

AN ABSTRACT OF THE DISSERTATION OF

Hyun Doug Yoon for the degree of Doctor of Philosophy in Civil Engineering
presented on August 11, 2011.

Title: Observations and Prediction of Intermittent Sediment Suspension in the Surf Zone

Abstract approved:

Daniel T. Cox

In this dissertation the interactions between hydrodynamics, sediment suspension and transport, and morphological evolution in the surf zone was investigated with a large-scale laboratory experiment data, CROss-Shore Sediment Transport Experiment (CROSSTEX). The data set included comprehensive measurements of water surface elevation, fluid velocity, sediment concentration, and morphology for irregular waves under erosive and accretive beach conditions.

First, hydrodynamics were examined in response to morphological evolution, focusing on turbulence due to wave breaking. For the erosive and accretive beach conditions, wave breaking characteristics, such as wave heights, average rate of energy dissipation by bores, and surf similarity parameter, were investigated in

response to morphodynamics of the bar. Time-averaged turbulent kinetic energy was closely related to wave energy dissipation, supporting that wave energy dissipation is the main source of turbulent kinetic energy production in the surf zone. From this, it was found that wave energy, turbulent estimates, and morphodynamics in the surf zone were closely related to each other and they were quantitatively examined.

Second, intermittent features of sediment suspension and turbulence, and their relationship were examined. Intermittent events of turbulence and sediment suspension occurred for a small portion of the time series but contained a significant amount of motions in these events. Comparison of intermittency statistics with previous studies conducted under different experimental conditions showed similar results, indicating that intermittency is a general aspect of turbulence and sediment suspension in the surf zone. Also the relationship between the turbulence and sediment suspension events were explored with conditional probabilities. Here, only 20~35% of the turbulent events were associated with sediment suspension events, implying that much of the intermittent turbulent motion may act to dissipate wave energy rather than suspend sediments. On the other hand, 50~65% of the sediment suspension events were associated with turbulent events, implying that intermittent turbulent motion is one of the fundamental mechanism for the initiation of sediment suspension in the surf

zone. It was also found that the intermittent sediment suspension events significantly contributed to onshore sediment transport.

Finally, the intermittent sediment suspension was predicted with an artificial neural network. Input hydrodynamics consisted of low-frequency motions, wave-induced motions, and turbulent kinetic energy near the bed and near water surface level. Artificial neural network provided a prominent prediction capability of sediment suspension, showing a correlation coefficient up to 0.79 at the bar crest in the accretive beach condition. From the investigation of various combinations of input data, it was found that turbulence is the most contributing factor for sediment suspension in the surf zone. The inclusion of the information from the upper sensor increases the prediction at the bar trough in the erosive case. The increased prediction at this location may possibly be attributed to the effect of vertical shear motion in the low-frequency range due to strong undertow from wave breaking.

© Copyright by Hyun Doug Yoon

August 11, 2011

All Rights Reserved

Observations and Prediction of Intermittent Sediment Suspension
in the Surf Zone

by
Hyun Doug Yoon

A DISSERTATION

submitted to

Oregon State University

in partial fulfillment of
the requirements for the
degree of

Doctor of Philosophy

Presented August 11, 2011
Commencement June 2012

Doctor of Philosophy dissertation of Hyun Doug Yoon presented on August 11, 2011.

APPROVED:

Major Professor, representing Civil Engineering

Head of the School of Civil and Construction Engineering

Dean of the Graduate School

I understand that my dissertation will become part of the permanent collection of Oregon State University libraries. My signature below authorizes release of my dissertation to any reader upon request.

Hyun Doug Yoon, Author

ACKNOWLEDGEMENTS

First of all, I would like to express my deepest appreciation to Dr. Daniel Cox for his guidance, support, patient and trust. I was so lucky to be his student and to work with him. Also I appreciate Dr. Kyung-Duck Suh at Seoul National University, who led me to coastal engineering. I thank Dr. Sungwon Shin for his brotherly support throughout the stay here in Corvallis.

I am thankful to Dr. Solomon Yim, Dr. Tuba Ozkan-Haller, Dr. Peter Ruggiero and Dr. Andrew Meigs (GCR) for serving as my committee. I would also like to thank Dr. Merrick Haller and Dr. Harry Yeh for their concern and advice during the PhD program. I thank to Dr. Dennis Albert for the knowledge about ‘bulrushes’. I also thank to Dr. Nobuhito Mori for the advice and discussion about the data analysis. I am grateful for the help, guidance, and encouragement given to me by the staff at O. H. Hinsdale Wave Research Laboratory: Tim Maddux, Jason Killian, Linda Fayler, Melora Park, Alicia Lyman-Holt, Alex Sinclair, and Dr. Bill MacDougal. I also thank to Dr. Tom Hsu, for hosting me during the short trip to University of Delaware and his guidance and comments on the numerical modeling. I must thank all of my friends, David Newborn, Kerri Bridges, Chris Bradner, Greg Guannel, Greg Wilson, Joe Long, Meg Palmsten and Justin Broderson, Kristen Splinter, and David Honegger for their friendship through the years. I will miss those basketball, softball, soccer and volleyball games.

Without unconditional support from my parents, parents-in-law and the family of my younger sister, I could not achieve this. My son, Hayden, always cheers me with his favorite song, 'Wheels on the bus'. Most of all, I deeply appreciate my wife, Jieun Shin, for her sacrifice and being with me as always.

This work was supported by the National Science Foundation (OCE-0351741).

CONTRIBUTION OF AUTHORS

Dr. Daniel T. Cox contributed to all chapters in this dissertation. In Chapters 2 and 3, Chris Scott, who was the former graduate student at Oregon State University, contributed to the experiment and preliminary analysis. In Chapter 3, Meghan Irving, who was a REU student from Smith College contributed to the experiment and preliminary analysis. In Chapter 4, Munki Kim, who was the exchange student from Seoul National University, contributed to the development of the neural network modeling.

TABLE OF CONTENTS

	<u>Page</u>
1 General Introduction	
References	4
2 Large-scale laboratory observations of wave breaking turbulence over an evolving beach	6
Abstract	7
2.1 Introduction	8
2.2 Experiment	12
2.3 Beach Morphodynamics	15
2.4 Wave Breaking Characteristics and Morphodynamics	16
2.5 Wave Breaking Turbulence	19
2.5.1 Despiking	19
2.5.2 Turbulence Estimate by the ST01 Method	19
2.5.3 Application of the ST01 method to Vertically Spaced ADVs	23
2.5.4 Time-Averaged Turbulence Intensities and TKE	25
2.5.5 Observation of Turbulence Over an Evolving Bottom	27
2.5.6 Observation of Turbulence Over a Quasi-Equilibrium Bottom	30
2.6 Discussion	31
2.6.1 Transition of Breaking Types	32
2.6.2 Increase of Horizontal Distance From the Bar Crest to the Bar Trough	33
2.6.3 Increase of Water Depth at the Bar Trough	34
2.7 Conclusions	34
Acknowledgements	37
References	37
3 Cross-shore variation of intermittent sediment suspension and turbulence induced by depth-limited wave breaking	67
Abstract	68
3.1 Introduction	69
3.2 Experiment	73
3.3 Data Reductions	77
3.3.1 Pre-process of Velocity and Sediment Concentration Data	77
3.3.2 Hydrodynamic Forcings and Sediment Response	78
3.3.3 Identifying Intermittent Events	82
3.4 Results	85

TABLE OF CONTENTS (Continued)

	<u>Page</u>
3.4.1 Cross-shore Variation of Intermittent Turbulence and Sediment Suspension near the Bed	85
3.4.2 Cross-shore and Vertical Distributions of Intermittent Turbulence and Sediment Concentration	95
3.4.3 Contribution of Intermittent Sediment Suspension on Cross-shore Transport	98
3.5 Discussion	101
3.5.1 Sediment Suspension Mechanism in addition to Turbulence	102
3.5.2 Intermittency on the Sediment Transport Modeling	103
3.6 Conclusions	104
Acknowledgements	107
References	107
4 Prediction of time-dependent Sediment Suspension in the Surf Zone using Artificial Neural Network.....	130
Abstract	131
4.1 Introduction	132
4.2 Data Set	137
4.3 Artificial Neural Network Model.....	142
4.3.1 General Configuration of ANN Structure	142
4.3.2 ANN Training	144
4.3.3 Procedures	145
4.4 Results and Discussion.....	146
4.5 Conclusions	150
Acknowledgements	151
References	152
5 General Conclusions	167
Bibliography.....	171

LIST OF FIGURES

<u>Figure</u>	<u>Page</u>
1.1 Sketch of nearshore process (courtesy of Dr. Daniel Cox).....	5
2.1 Sketch of experimental setup with initial bed profile before E1. Wavemaker is located at $x=0$ m	45
2.2 Photo of vertical stack of ADVs (modified from Scott et al., 2006).	46
2.3 Mesh plot of beach profile evolution: (a) erosive case and (b) accretive case.....	47
2.4 Time series of (a) bar shape parameter (H_{bar} / W_{bar}) and (b) bar cross-shore location (x_{bar}). Definition sketch of H_{bar} / W_{bar} is shown in upper right box in panel (a).....	48
2.5 Cross-shore distributions of (a) significant wave height (H_s), (b) average rate of energy dissipation by bores $\langle \varepsilon_b \rangle$, and (c) bottom profiles averaged across the wave flume for erosive case. Runs are selected when ADVs are located at bar trough ($x_{ADV}=63.70$ m). In panel (c), the initial bathymetry is indicated by dashed line and cross-shore location of ADVs is shown as a vertical line.....	49
2.6 Cross-shore distributions of (a) significant wave height (H_s), (b) average rate of energy dissipation by bores $\langle \varepsilon_b \rangle$, and (c) bottom profiles averaged across the wave flume for accretive case. Runs are selected when ADVs are located at the bar crest ($x_{ADV}=63.70$ m) or at bar trough ($x_{ADV}=65.54$ m). In panel (c), initial bathymetry is indicated by dashed line and cross-shore location of ADVs is shown as a vertical line.....	50

LIST OF FIGURES (Continued)

<u>Figure</u>	<u>Page</u>
<p>2.7 Time variation of the surf similarity parameter. Since bottom profiles for A8 and A9 were not measured, the bathymetry of A7 was used for the calculations of the surf similarity parameter for A8 ($t_{elapsed} = 255$ min) and A9 ($t_{elapsed} = 270$ min).....</p>	51
<p>2.8 Temporal variation of (a) u at $\zeta = 0.50$ m (black line), u at $\zeta = 0.31$ m (blue line), and coherent wave motion of u (red line); (b) u^{12} from ST01 (red line) and from T98 (blue line); (c) v at $\zeta = 0.50$ m (black line), v at $\zeta = 0.31$ m (blue line), and coherent wave motion of v (red line); (d) v^{12} from ST01 (red line) and from T98 (blue line); (e) w at $\zeta = 0.50$ m (black line), w at $\zeta = 0.31$ m (blue line), and coherent wave motion of w (red line); and (f) w^{12} from ST01 (red line) and from T98 (blue line), for E1.....</p>	52
<p>2.9 Squared coherence (γ^2) (in upper panels) and phase difference (ϕ) (in lower panels) of ADV6 and ADV5 for E1, smoothed using band averaging with 50 degrees of freedom: (a, d) cross-shore velocity; (b, e) alongshore velocity; and (c, f) vertical velocity. Dashed lines in upper panels are 95% confidence level. In lower panels, dots indicate the phase difference at frequencies where squared coherences are above 95% confidence level and vertical lines indicate 95% confidence intervals for these phase differences.</p>	53
<p>2.10 Power spectral densities (PSD) of instantaneous velocity (dotted lines) and turbulence velocity (solid lines) at ADV6 for E1: (a) cross-shore; (b) alongshore; and (c) vertical component. Turbulent velocity is estimated with ADV5 and ADV6. Despiked and interpolated velocities described in section 5.1 are used and high-pass-filtered with cut-off frequency of 0.0625 Hz. PSD is smoothed using band averaging with 50 degrees of freedom. The Kolmogorov's $-5/3$ slope is indicated as reference of turbulent inertial subrange. Vertical lines indicate 95% confidence intervals. The filter length is chosen as a half of significant wave period as suggested by Shaw and Trowbridge (2001).....</p>	54

LIST OF FIGURES (Continued)

<u>Figure</u>	<u>Page</u>
2.11 Temporal variation of (a) u at $\zeta = 0.50$ m (black line), u at $\zeta = 0.01$ m (blue line), and coherent wave motion of u (red line); (b) u'^2 from ST01 (red line) and from T98 (blue line); (c) v at $\zeta = 0.50$ m (black line), v at $\zeta = 0.01$ m (blue line), and coherent wave motion of v (red line); (d) v'^2 from ST01 (red line) and from T98 (blue line); (e) w at $\zeta = 0.50$ m (black line), w at $\zeta = 0.01$ m (blue line), and coherent wave motion of w (red line); and (f) w'^2 from ST01 (red line) and from T98 (blue line), for E1	55
2.12 Squared coherence (γ^2) (in upper panels) and phase difference (ϕ) (in lower panels) of ADV6 and ADV1 for E1, smoothed using band averaging with 50 degrees of freedom: (a, d) cross-shore velocity; (b, e) alongshore velocity; and (c, f) vertical velocity. Dashed lines in upper panels are 95% confidence level. In lower panels, dots indicate the phase difference at frequencies where squared coherences are above 95% confidence level and vertical lines indicate 95% confidence intervals for these phase differences.	56
2.13 Vertical distributions of Froude-scaled turbulence intensities for E1: (a) $(\overline{u'^2} / gh)^{1/2}$, (b) $(\overline{v'^2} / gh)^{1/2}$, (c) $(\overline{w'^2} / gh)^{1/2}$, and (d) $(\overline{k} / gh)^{1/2}$. Square, circle, and asterisk indicate high-pass filter (cut-off frequency: 1 Hz), ST01 method, and T98 method, respectively	57
2.14 Comparison of $(\overline{k} / gh)^{1/2}$ between Scott et al., (2005) and the present study (CROSSTEX). P4(Scott et al., (2005)) and E11(CROSSTEX) are measured at the bar crest and P5(Scott et al., (2005)) and E10(CROSSTEX) are measured at the bar trough.....	58
2.15 Vertical distributions of $(\overline{k} / gh)^{1/2}$ at bar trough for (a) erosive case ($x_{ADV} = 63.70$ m) and (b) accretive case ($x_{ADV} = 65.54$ m).....	59

LIST OF FIGURES (Continued)

<u>Figure</u>	<u>Page</u>
2.16 Relation between depth-averaged \bar{k} ($x_{ADV}=63.70$ m for erosive case; $x_{ADV}=65.54$ m for accretive case) and average rate of energy dissipation by bores $\langle \varepsilon_b \rangle$. $\langle \varepsilon_b \rangle$ for erosive case is measured at $x_{WG}=63.87$ m. $\langle \varepsilon_b \rangle$ for accretive case is averaged with the calculations at $x_{WG}=63.87$ m and 67.53 m.....	60
2.17 Vertical distribution of $(\bar{k} / gh)^{1/2}$ for accretive case at bar crest (A1, A3, A5; $x_{ADV}=63.70$ m; solid line) and at bar trough (A2, A4, A6; $x_{ADV}=65.54$ m; no line).....	61
2.18 Cross-shore and vertical distributions of $(\bar{k})^{1/2}$ during quasi-equilibrium state: (a) erosive case (E7-E11) and (b) accretive case (A5-A9). Bottom profiles are averaged during quasi-equilibrium state. Dashed line indicates wave trough level calculated as average of 1/3 lowest wave trough levels from zero-upcrossing.....	62
2.19 Cross-shore and vertical distributions of ε during quasi-equilibrium state: (a) erosive case (E7-E11) and (b) accretive case (A5-A9). Bottom profiles are averaged during quasi-equilibrium state. Dashed line indicates wave trough level calculated as average of 1/3 lowest wave trough levels from zero-upcrossing.....	63
2.20 Exponential curve fitting of $(\bar{k} / gh)^{1/2}$ for erosive case at bar trough. Fitting coefficients are given in the top left corner.....	64
3.1 Bathymetry and cross-shore locations of the instrument array: (a) erosive and unstable (EU), (b) erosive and quasi-equilibrium (EQ), (c) accretive and unstable (AU), and (d) accretive and quasi-equilibrium (AQ). The vertical dashed lines represent the locations of the instrument array.....	114

LIST OF FIGURES (Continued)

<u>Figure</u>	<u>Page</u>
<p>3.2 Instrument array on mobile cart: vertical stack of ADV (right) and FOBS (middle). Inset photo shows mobile cart in Large Wave Flume.....</p>	<p>115</p>
<p>3.3 Temporal variation of (a) low-frequency motion of u, (b) wave-induced motion of u, (c) k estimated at ADV1 ($\zeta = 1$ cm) with ADV3 ($\zeta = 9$ cm), and (d) suspended load (C) detected at lower panel ($1 < \zeta < 9$ cm), for E2. In (a), thick solid line represents ADV1 ($\zeta = 1$ cm) and thin dashed line represents ADV6 ($\zeta = 50$ cm), and horizontal dotted line represents where $u_{lf} = 0$. In (b), wave-induced motion of ADV1 ($\zeta = 1$ cm) is plotted. In (c) and (d), the dash-dot lines indicate the mean plus a standard deviation of the time series. In (c) and (d), the thick lines represent the moving-averaging with 2-second filter length. The peak of each event over the mean plus one standard deviation is indicated as a triangle in (c) or a circle in (d). The closed triangles and circles denote the correlated events between k and C with a window length of $\pm T_p / 2$, while the open triangles and circles denote the uncorrelated events.....</p>	<p>116</p>
<p>3.4 Temporal variation of (a) low-frequency motion of u, (b) incident waves motion of u, (c) k_u estimated at ADV6 ($\zeta = 50$ cm) with ADV5 ($\zeta = 31$ cm), (d) k_l estimated at ADV1 ($\zeta = 1$ cm) with ADV3 ($\zeta = 9$ cm), and (e) suspended load (C) detected at lower panel ($1 < \zeta < 9$ cm), for E2, in the range of $330s < t < 400s$. In (a) and (b), thick solid line represents ADV1 ($\zeta = 1$ cm) and thin dashed line represents ADV6 ($\zeta = 50$ cm). Dotted line represents where $u_{lf} = 0$ and $u_{wave} = 0$. In (c), k at ADV6 ($\zeta = 50$ cm) are denoted as k_u. In (d), k at ADV1 ($\zeta = 1$ cm) are denoted as k_l. In (c), (d), and (e), the dashed lines indicate the mean plus three standard deviations of the time series. The events over the mean plus three standard deviations are indicated as gray region.....</p>	<p>117</p>

LIST OF FIGURES (Continued)

<u>Figure</u>	<u>Page</u>
<p>3.5 Temporal variation of: (a) mean of time-averaged k, (b) mean of standard deviation of k, (c) mean of time-averaged C, (d) standard deviation of C, (e) percentage of coherent events, (f) percentage of the motion contained in coherent events, (g) percentage of intense events, and (h) percentage of the motion contained in intense events, at bar trough, for erosive case. Symbols indicate the average of the eight 100-second segment estimation (total 800 sec), excluding the first segment. Closed square, open square, and open circle represent k_u, k_l (ADV2 was used for E4 and E5), and C, respectively.....</p>	118
<p>3.6 Cross-shore distribution of: (a) mean of time-averaged k, (b) mean of time-averaged C, (c) ratio of mean to standard deviation of k and C, (d) percentage of coherent events, (e) percentage of the motion contained in coherent events, (f) percentage of intense events, and (g) percentage of the motion contained in intense events, and (h) bathymetry and locations of the instrumental array for EQ. Symbols indicate the average of the eight 100-second segment estimation, excluding the first segment. Open square and open circle represent k and C, respectively.....</p>	119
<p>3.7 Cross-shore distribution of: (a) mean of time-averaged k, (b) mean of time-averaged C, (c) ratio of mean to standard deviation of k and C, (d) percentage of coherent events, (e) percentage of the motion contained in coherent events, (f) percentage of intense events, and (g) percentage of the motion contained in intense events, and (h) bathymetry and locations of the instrumental array for AQ. Symbols indicate the average of the four 180-second segment estimation, excluding the first segment. Open square and open circle represent k and C, respectively.....</p>	120

LIST OF FIGURES (Continued)

<u>Figure</u>	<u>Page</u>
<p>3.8 Cross-correlation (γ_{kC}) between k and C. The solid line represents the average of all erosive cases and the dashed line represents the average of all accretive cases. The (-) sign means that k leads C. The lag (τ) is normalized by peak period (T_p). The horizontal gray line represents the length of $\pm T_p / 2$</p>	121
<p>3.9 Cross-shore and vertical distribution of: (a) m_k and $m_k + \sigma_k$, (b) m_c and $m_c + \sigma_c$, (c) $(n_3/n)_k$ and $(n_3/n)_c$, and (d) $(n_3m_3/nm)_k$ and $(n_3m_3/nm)_c$, for EQ state. The average of the eight 100-second segment estimation is plotted. Bottom profiles are averaged during EQ state. Dash-dot line indicates wave trough level calculated as average of 1/3 lowest wave trough levels from zero-upcrossing</p>	122
<p>3.10 Cross-shore and vertical distribution of: (a) m_k and $m_k + \sigma_k$, (b) m_c and $m_c + \sigma_c$, (c) $(n_3/n)_k$ and $(n_3/n)_c$, and (d) $(n_3m_3/nm)_k$ and $(n_3m_3/nm)_c$, for AQ state. The average of the four 180-second segment estimation is plotted. Bottom profiles are averaged during AQ state. Dash-dot line indicates wave trough level calculated as average of 1/3 lowest wave trough levels from zero-upcrossing.....</p>	123
<p>3.11 Cross-shore distribution of: (a) significant wave height, (b) \bar{u}_f at ADV1 ($\zeta = 1$ cm), (c) \bar{u}_{wave} at ADV1 ($\zeta = 1$ cm), (d) cross-shore sediment flux, and (e) bathymetry and locations of the instrumental array, for EQ. In (b), (c) and (d), closed circle and open triangle represent estimates during intense events and whole time series, respectively</p>	124

LIST OF FIGURES (Continued)

<u>Figure</u>	<u>Page</u>
<p>3.12 Cross-shore distribution of: (a) significant wave height, (b) \bar{u}_f at ADV1 ($\zeta = 1$ cm), (c) \bar{u}_{wave} at ADV1 ($\zeta = 1$ cm), (d) cross-shore sediment flux, and (e) bathymetry and locations of the instrumental array, for AQ. In (b), (c) and (d), closed circle and open triangle represent estimates during intense events and whole time series, respectively.....</p>	125
<p>3.13 (a) Comparison of $(n_3 m_3 / nm)$ of C with sediment concentration at $\zeta = 5$ cm of JS92. (b) Sediment transport by the intense events for EQ, AQ and JS92. Closed circle, closed square, and open triangle represent the intense events for EQ, AQ, and JS92, respectively. x^* denotes normalized cross-shore locations with $x^* = 0$ at bar crest and $x^* = 1$ at shoreline.....</p>	126
<p>4.1 Bathymetry and locations of measurements for: (a) erosive and quasi-equilibrium (EQ) and (b) accretive and quasi-equilibrium (AQ). Open circle and square represents lower ADV (ADV1, $\zeta = 0.01$ m), and upper ADV (ADV6, $\zeta = 0.50$ m), respectively. At A8, ADV5 ($\zeta = 0.31$ m) is replaced for upper ADV. Vertical lines near bed indicates the range of FOBS from $\zeta = 0.01$ to 0.09 m. Horizontal dash-dot lines represent wave crest and trough level calculated as average of 1/3 highest and lowest water surface levels from zero-upcrossing.....</p>	156
<p>4.2 Example of inputs (a-d) and output (e) for E10: (a) cross-shore velocity of low-frequency motion at lower ADV (ADV1, $\zeta = 0.01$ m, solid line) and upper ADV (ADV6, $\zeta = 0.50$ m, dashed line), (b) cross-shore velocity of low-frequency motion at lower ADV, (c) turbulent kinetic energy per unit mass (k) at upper ADV (gray and thin: raw, black and solid: smoothed), (d) turbulent kinetic energy per unit mass (k) at lower ADV (gray and thin: raw, black and solid: smoothed), and (e) suspended load (C).....</p>	157

LIST OF FIGURES (Continued)

<u>Figure</u>	<u>Page</u>
4.3 Sketch of ANN structure	158
4.4 Standard deviation of correlation coefficient with number of iteration. Input case 8 and Subset 5 is used for the training, validation, and prediction. Closed symbols represent EQ: circle (E7), square (E8), diamond (E9), upward triangle (E10), and downward triangle (E11). Open symbols represent AQ: circle (A5), square (A6), diamond (A7), upward triangle (A8), and downward triangle (A9).....	159
4.5 Example of inputs (a-d) and output (e) for E10 for input case 11 and subset 5: (a) cross-shore velocity of low-frequency motion at lower ADV (ADV1, $\zeta = 0.01$ m, solid line) and upper ADV (ADV6, $\zeta = 0.50$ m, dashed line), (b) cross-shore velocity of low-frequency motion at lower ADV, (c) turbulent kinetic energy per unit mass (k) at upper ADV, (d) turbulent kinetic energy per unit mass (k) at lower ADV, and (e) measured (gray) and predicted (solid) suspended load. In (c), (d), and (e), the smoothed lines (moving averaged with 2 s filter) are shown.....	160
4.6 Time series of observed suspended load (gray line) and predicted suspended load (solid line) for E10, in the range of $300 \text{ s} < t < 500 \text{ s}$. Input case 11 and Subset 5 is used for the training, validation, and prediction. Correlation coefficient between the observed and predicted suspended load is provided in upper left.....	161
4.7 Cross-shore variation of the average of correlation coefficients over all subsets, for EQ: (a) Group 1 (Case 1), (b) Group 2 (Case 2-4), (c) Group 3 (Case 5-8), (d) Group 4 (Case 9-11), and (e) averaged bathymetry over EQ. Legends indicate input case number.....	162

LIST OF FIGURES (Continued)

<u>Figure</u>		<u>Page</u>
4.8	Cross-shore variation of the average of correlation coefficients over all subsets, for AQ: (a) Group 1 (Case 1), (b) Group 2 (Case 2-4), (c) Group 3 (Case 5-8), (d) Group 4 (Case 9-11), and (e) averaged bathymetry over AQ. Legends indicate input case....	163

LIST OF TABLES

<u>Table</u>	<u>Page</u>
2.1 Summary of experimental conditions and observations during CROSSTEX.	65
2.2 Anisotropy characteristics inside surf zone.	66
3.1 Summary of experimental observations.....	127
3.2 Comparison of intermittency statistics for k and C	128
3.3 Coherent event analysis of k and C	129
4.1 Summary of literatures using artificial neural network in coastal and nearshore research.....	164
4.2 Case of input data.....	165
4.3 Subset for training, validation and prediction.....	166

Observations and Prediction of Intermittent Sediment Suspension in the Surf Zone

Chapter 1

General Introduction

Wave breaking turbulence and sediment suspension is an important factor for understanding hydrodynamics and sediment transport in the surf zone. Figure 1.1 illustrates the qualitative mechanism of sediment suspension in the surf zone. Wave energy loss caused by breaking is converted to turbulent kinetic energy (TKE) in the vicinity of wave trough level, and this TKE is infused into the water column. The TKE in the water column links hydrodynamics and sediment transport by enhancing vertical mixing and sediment suspension, and modifying forcing patterns for mean flows and consequently influences on a beach evolution mechanism in the surf zone. Despite the importance of wave breaking turbulence and sediment suspension to the beach evolution mechanisms in the surf zone, however, understanding of sediment suspension mechanism in response to hydrodynamics (including turbulence) is still unclear.

For the study of turbulence and associated sediment transport, near-prototype scale laboratory experiments were strongly recommended. Recently, Scott et al. (2005)

observed wave breaking turbulence on a fixed barred beach (i.e., without sediments) in a large-scale laboratory flume. They showed that wave breaking turbulence was the greatest at the bar crest and that TKE was transported to the bed. These results supported the hypothesis that wave breaking turbulence is an important factor for near-bed processes in nearshore environments. However, in the study of Scott et al. (2005), the response of the beach (e.g., sediment suspension) to hydrodynamic forcing (e.g., turbulence) could not be observed due to the fixed bed. To address this limitation, the study of Scott et al. (2005) was extended by replacing the fixed barred beach with a natural sand beach, as part of CROss-Shore Sediment Transport Experiment (CROSSTEX). Among the multi-investigated goals of CROSSTEX, this dissertation will investigate the interaction between hydrodynamics (focusing on turbulence) and sediment suspension. The data set included comprehensive measurements of water surface elevation, fluid velocity, sediment concentration, and morphology for irregular waves under erosive and accretive beach conditions. In addition to observations of turbulence and sediment suspension, the prediction model of time-dependent sediment suspension is developed. This dissertation is organized as follows.

In Chapter 2, hydrodynamics were examined in response to morphological evolution, focusing on turbulence due to wave breaking. Time-averaged turbulent kinetic energy and turbulence dissipation rate are estimated and their relationship with wave energy dissipation, which is dependent on morphological changes, will

be investigated. By doing so, the relationships between hydrodynamics, such as wave energy dissipation, turbulent kinetic energy and turbulence dissipation rates, and morphodynamics in the surf zone will be quantitatively explored. It is noted that this manuscript was published in *Journal of Geophysical Research – Oceans* in 2010 (Yoon and Cox, 2010).

In Chapter 3, intermittent features of sediment suspension and turbulence, and their relationship are examined. Intermittent events of turbulence and sediment suspension will be compared each other, and also be compared with previous studies conducted under different experimental conditions in the surf zone. Also the relationship between the turbulence and sediment suspension events are examined with conditional probability. For example, suspension events on the condition of turbulence events, or vice versa, will be computed across the surf zone. Also, the contribution of these intermittent suspension events to cross-shore sediment transport will be examined. This chapter was submitted to *Continental Shelf Research* in June, 2011.

In Chapter 4, time-dependent sediment suspension is predicted with an artificial neural network. Suspended load near bed will be predicted with the optimized artificial neural network, using various input combinations including low-frequency motion, wave-induced motion, and turbulent kinetic energy near the bed

and from upper sensor. This chapter was submitted to Coastal Engineering in August, 2011.

References

Scott, C. P., D. T. Cox, T. B. Maddux, and J. W. Long. 2005. Large-scale laboratory observations of turbulence on a fixed barred beach, *Meas. Sci. Technol.* 16, 1903-1912.

Yoon, H.-D, and D. T. Cox, 2010, Large-scale laboratory observations of wave breaking turbulence over an evolving beach, *J. Geophys. Res.*, 115 ,C10007, Doi:10.1029/2009JC005748.

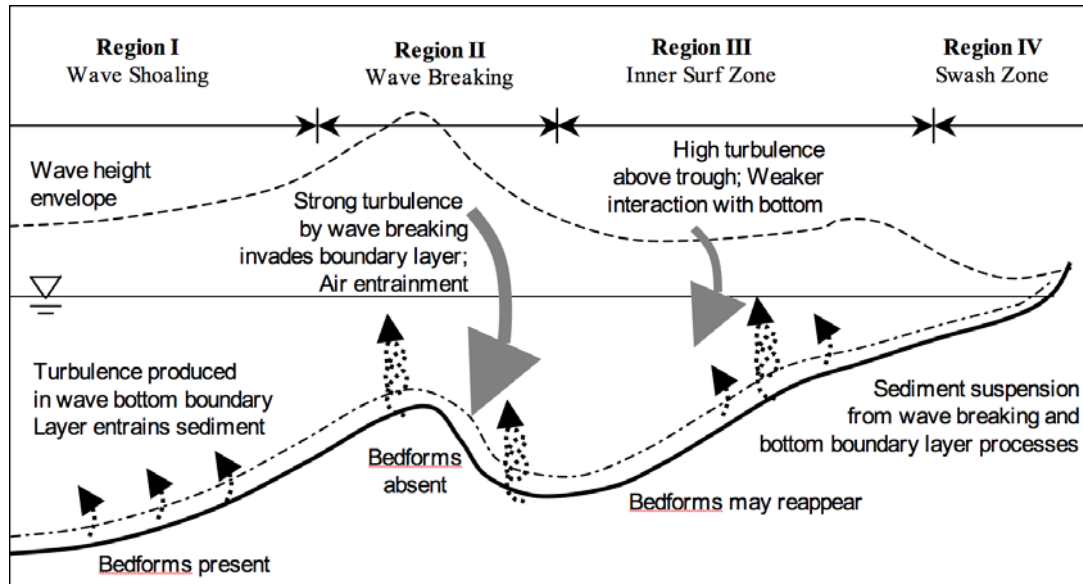


Figure 1.1: Sketch of nearshore process (courtesy of Dr. Daniel Cox)

Chapter 2

**Large-scale laboratory observations of wave breaking
turbulence over an evolving beach**

Hyun-Doug Yoon

School of Civil and Construction Engineering

Oregon State University, Corvallis, OR 97331-2302, USA

Tel: 541-737-6967 Fax: 541-737-6974 Email: yoonyh@onid.orst.edu

Daniel T. Cox

School of Civil and Construction Engineering

Oregon State University, Corvallis, OR 97331-2302, USA

Journal of Geophysical Research – Oceans

Vol. 115, C10007, doi:10.1029/2009JC005748, 2010

Abstract

Wave breaking turbulence over an evolving beach was observed in a large-scale laboratory flume, as part of the CROss-Shore Sediment Transport EXperiment (CROSSTEX). The data set included comprehensive measurements of water surface elevation, fluid velocity, and morphology for irregular waves under erosive and accretive wave conditions. For the both conditions, the beach reached a quasi-equilibrium state, defined as when the bar shape was stable. Wave breaking characteristics, such as wave heights, average rate of energy dissipation by bores, and surf similarity parameter, were investigated in response to morphodynamics of the bar. Turbulent kinetic energy (TKE) was estimated using the method by Shaw and Trowbridge (2001). As the beach evolved, a less amount of TKE was observed at the trough for the erosive case, while more TKE was observed at the trough for the accretive case. It was also found that the temporal variation of the time-averaged TKE were closely associated with the average rate of energy dissipation by bores. Comparing with the bar trough, the vertical distribution of nondimensionalized time-averaged TKE and turbulence dissipation rate at the bar crest showed a large increase near the bottom, probably due to a strong cross-shore RMS velocity. Finally, in the quasi-equilibrium state, time-averaged TKE and turbulence dissipation rate at the bar trough were smaller than those inside the surf zone. Inside the surf zone, significant turbulence intensities were observed due to a second breaking on a shallow water depth.

Keywords: wave breaking turbulence, large-scale laboratory experiment, evolving beach, quasi-equilibrium state, average rate of energy dissipation by bores, turbulent kinetic energy, turbulence dissipation rate

2. 1 Introduction

Wave breaking turbulence is an important factor for understanding hydrodynamics and sediment transport in the surf zone. Wave energy loss caused by breaking is converted to turbulent kinetic energy (TKE) in the vicinity of wave trough level, and this TKE is infused into the water column. The TKE in the water column links hydrodynamics and sediment transport by enhancing vertical mixing and sediment suspension, and modifying forcing patterns for mean flows (Holman, 1995) and consequently influences on a beach evolution mechanism in the surf zone. For example, the beach profile evolution model of Dally and Dean (1984) introduced the effect of wave breaking turbulence on bottom shear stress which triggered an increase in the suspended load. Roelvink and Stive (1989) also considered the stirring effect of sediment by turbulence for their energetic-based Bowen/Bailard model (1981), and they showed improved beach profile prediction by comparing with laboratory data. Despite the importance of wave breaking turbulence on the beach evolution mechanisms in the surf zone, however, few observations of turbulence in response to an evolving beach have been made under controlled conditions.

The studies of wave breaking turbulence have mostly been conducted in small-scale laboratory flumes (e.g., Stive, 1980; Nadaoka and Kondoh, 1982; Ting and Kirby, 1994, 1995, 1996; Cox et al., 1995; Chang and Liu, 1999; Govender et al., 2002; Melville et al., 2002; Kimmoun and Branger, 2007; Huang et al., 2009), because researchers can utilize well-controlled experimental conditions (e.g., regular waves, a solitary wave, and a planar beach) and state-of-the-art measuring techniques. These studies have helped us understand wave breaking turbulence and turbulent kinetic energy equation (e.g., Tennekes and Lumley, 1972), applied to the nearshore. Alternatively, field observations of turbulence in the surf zone have also been carried out (e.g., George et al., 1994; Trowbridge and Elgar, 2001; Rodriguez et al., 1999). However, the difficulties in the operation of instruments and the control of environmental conditions have hindered adequate quantification of wave breaking turbulence. Moreover, these turbulence observations in the field assumed the seabed was stable and did not account for changes in the bottom profile.

On the other hand, observations of waves and hydrodynamics on barred beached also have been collected over the years on the small-scale laboratory experiments (e.g., Smith and Kraus, 1991; Cox and Kobayashi, 1998; Haller et al., 2002; Blenkinsopp and Chaplin, 2008; Govender et al., 2009) or in the field (e.g., Roelvink and Stive, 1989; Haines and Sallenger, 1994; Thornton et al., 1996; Elgar et al. 1997; Gallagher et al., 1998; Aargaard et al, 1998; Garcez Faria et al.,

2000; Kuriyama, 2002; Marino-Tapia, 2007a; Marino-Tapia, 2007b). Despite a number of research of hydrodynamics over a barred beach, turbulence observation is still rare due to the complex flow field caused by a barred beach, along with the difficulties mentioned previously.

To fill the gap between the small-scale laboratory experiments and field observations in the study of turbulence and associated sediment transport, near-prototype scale laboratory experiments were strongly recommended by Thornton et al. (2000). Recently, Scott et al. (2005) observed wave breaking turbulence on a fixed barred beach (i.e., without sediments) in a large-scale laboratory flume. They showed that wave breaking turbulence was the greatest at the bar crest and that TKE was transported to the bed. These results supported the hypothesis that wave breaking turbulence is an important factor for near-bed processes in nearshore environments. However, in the study of Scott et al. (2005), the response of the beach (e.g., sediment suspension) to hydrodynamic forcing (e.g., turbulence) could not be observed due to the fixed bed. To address this limitation, the study of Scott et al. (2005) was extended by replacing the fixed barred beach with a natural sand beach, as part of CROSS-Shore Sediment Transport Experiment (CROSSTEX). Among the multi-investigated goals of CROSSTEX, this paper will focus on the observations of wave breaking turbulence over an evolving beach in a prototype-scale laboratory experiment.

Another aspect of the difficulty in turbulence observation in the surf zone is how to estimate turbulence intensities from instantaneous velocity data. Separating the wave and turbulent component is challenging because the wave component is unsteady. Traditionally, ensemble averaging has been used in small-scale experimental turbulence studies by using regular waves or repeating the experiment under the same condition. High-pass filtering (e.g., Nadaoka et al., 1989) is another conventional technique, which is based on the assumption that turbulence is confined to high frequency motions. In the field, turbulence intensities have been estimated from the dissipation rates in the turbulent inertial subrange (George et al., 1994). Trowbridge (1998), hereinafter referred to as T98, developed a novel but simple technique to separate wave and turbulence motions. The basic assumption is that the length scale of turbulence is smaller than the distance between two measurement points, and that the length scale of the wave is larger. Under this assumption, the differencing of two velocity data results in turbulence. The wave components of two measuring points are removed by differencing since wave components are assumed identical. Shaw and Trowbridge (2001), hereinafter referred to as ST01, improved the T98 method by applying a least square filter to reduce possible differences in velocity magnitude and phase in the wave motion. Recently, Feddersen and Williams (2007) modified T98 and ST01 and provided the vertical structure of Reynolds stress in a wave-dominant environment seaward of the surf zone.

The objective of this paper is to provide a large-scale, synoptic, and process-based data of hydrodynamics and morphology over an evolving beach during relatively short time steps in the surf zone. To estimate the vertical distribution of wave breaking turbulence in response to morphodynamics, the ST01 method is used. Section 2.2 describes the experimental setup and procedures and Section 2.3 shows the results of beach morphodynamics. Then Section 2.4 presents the interactions between wave breaking characteristics and morphodynamics. Section 2.5 explains the methodology of the ST01 method and shows the vertical distribution of wave breaking turbulence over an evolving and a quasi-equilibrium beach. Section 2.6 discusses the contributing factors on wave breaking turbulence on an evolving beach. Finally, the main conclusions are summarized in Section 2.7.

2. 2 Experiment

CROSSTEX was conducted in the large wave flume at Oregon State University's O H Hinsdale Wave Research Laboratory during the summer of 2005. The flume was 104 m long, 3.7 m wide, and 4.6 m deep with a programmable flap-type wavemaker. A natural beach was installed using approximately 800 m³ of Oregon beach sand, with a median grain diameter of $d_{50}=0.22$ mm. Observations were made during two types of irregular waves which caused two morphological cases: the formation of a sand bar (an erosive case) and restoration of the planar beach (an accretive case). Table 2.1 summarized the experimental conditions and observations. The irregular waves were simulated with a TMA spectrum (Bouws

et al., 1985), with target significant wave height ($(H_s)_t$), target peak wave period ($(T_p)_t$), and peak enhancement factor (γ_{peak}) of 0.6 m, 4.0 s, 3.3 for the erosive case and of 0.4 m, 7.0 s, 10.0 for the accretive case. For this paper, 11 erosive runs (E1~E11) and 9 accretive runs (A1~A9) were investigated. Although there was a range of breaker types (spilling and plunging) for both cases, spilling breakers were observed predominant for the erosive case and plunging breakers were observed predominant for the accretive case. The duration of each run (t_{dur}) was mostly 15 minutes, but some runs in the accretive case (A3, A5, A6, and A7) lasted 45 minutes. The total elapsed times ($t_{elapsed}$) were 180 minutes for the erosive and 300 minutes for the accretive case. Note that there were regular wave runs between the erosive and accretive cases to develop the bar features but they were not included in this study. The significant wave height (H_b) and peak period (T_p) at the bar crest where wave breaking predominantly occurred ($x=60.21$ m) are also included in Table 2.1. The significant wave height (H_s) was calculated with $H_s = 4.004\sqrt{m_0}$, where m_0 is the zeroth moment of a wave spectrum. In addition, the cross-shore location (x_{ADV}), significant wave height (H_s), water depth (h), and the number of wave breaking (N_b) at the vertical array are also listed in Table 2.1. The number of wave breaking (N_b) were visually observed during each run. More of experiment procedure will be given later in this section.

Free surface elevations were measured using 10 wire resistance-type wave gauges mounted along the walls of the large wave flume, with 50 Hz sampling rate (Figure 2.1). The coordinate system was x positive onshore and z positive up, with $x=0$ m at the wavemaker and $z=0$ m at the still water level (SWL). In the region where there were sharp gradients in the wave height due to shoaling and breaking, 5 wave gauges were placed at approximately 3.65 m intervals from $x_{WG}=56.56$ m to $x_{WG}=71.18$ m, where x_{WG} is denoted as the cross-shore location of wave gauge.

The cross-shore velocity (u), alongshore velocity (v), and vertical velocity (w) were measured at six elevations at each cross-shore location using an acoustic Doppler velocimeter (ADV), with a sampling rate of 50 Hz. ADVs were installed on a vertical array in the mobile instrument cart (Figure 2.2). The vertical array was lowered such that the sampling volume of the bottom most ADV was 1.0 cm above the bed. The distances from the bed of the ADVs (ζ) were 1.0 cm (ADV1), 5.0 cm (ADV2), 9.0 cm (ADV3), 20.0 cm (ADV4), 31.0 cm (ADV5), and 50.0 cm (ADV6).

The cross-shore bathymetry was surveyed using a multiple transducer array (MTA) mounted on the mobile instrument cart after each run. The beach was unstable in the early runs (E1~E6 for the erosive case, A1~A6 for the accretive case). During these runs, the vertical array of ADVs was located at the bar trough

region (the erosive case) or both the bar crest and trough regions (the accretive case). After E6 and A6, the beach was observed to be stable. The ADV array was moved to new cross-shore locations and the same wave forcing repeated for E7~E11 and A7~A9. The cross-shore locations of the vertical array (x_{ADV}) are listed in Table 2.1. Detailed observation of the beach profile evolution are provided in Section 2.3.

2.3 Beach morphodynamics

Figure 2.3 shows the temporal evolution of the cross-shore bottom profile. The initial planar beach evolved to a bar-shaped geometry in the erosive case, while a preexisting bar recovered to a planar beach in the accretive case. Although there are small bars inside the surf zone, we will concentrate on the outer bar of which the crest is located around $x=61$ m, because it predominantly affected the wave breaking process. To monitor the characteristics of the bar, the bar shape is parameterized with H_{bar} / W_{bar} , where H_{bar} and W_{bar} are the vertical and horizontal distance from the bar crest and trough, respectively, as shown in Figure 2.4a. For the both cases, H_{bar} / W_{bar} reaches a constant value (~ 0.07 for the erosive case, ~ 0.06 for the accretive case) in approximately 100 minutes ($1500T_p$ for the erosive case, $857T_p$ for the accretive case). This tendency is also found in Figure 2.3 in which morphological changes predominantly occur in the initial stage. The beach morphology interacts with hydrodynamic forcing (e.g., wave height), and

evolves until a quasi-equilibrium state is reached (Hughes, 1998). In the present study, we define the “quasi-equilibrium” state when H_{bar} / W_{bar} is constant. In addition to H_{bar} / W_{bar} , the cross-shore location of the bar crest, x_{bar} , is also shown in Figure 2.4b. Even in the quasi-equilibrium state, it is found that the bar migrates slowly offshore (decreasing x_{bar}) in the erosive case, and onshore (increasing x_{bar}) in the accretive case (Figure 2.4b). Although there is a bar migration, the concept of the quasi-equilibrium state is consistent with the definition of an equilibrium profile in Roelvink and Broker (1993) in which a cross-shore profile translates seawards or shorewards without changing form. Similarly, Wang et al. (2002) defined the quasi-equilibrium as the state when the beach profile is stable.

2. 4 Wave breaking characteristics and morphodynamics

Figure 2.5 shows the relation between the wave breaking characteristics and morphodynamics for the erosive case. Wave breaking predominantly occurs near the bar crest, and wave heights at this point ($x_{WG}=60.21$ m) increase with elapsed runs (Figure 2.5a). This is because the bottom slope prior to the bar crest becomes steeper (Figure 2.5c).

The energy dissipation by breaking waves was used to calculate the wave height decay and as a measure of the production of turbulence in the surf zone (Fredsoe and Deigaard, 1998; Thornton and Guza, 1983). For Rayleigh-distributed irregular

waves, Thornton and Guza (1983) proposed the average rate of energy dissipation by bores ($\langle \varepsilon_b \rangle$) as

$$\langle \varepsilon_b \rangle = \frac{3\sqrt{\pi}}{16} \rho g B^3 \bar{f} \frac{H_{rms}^5}{\gamma^2 h^3} \left[1 - \frac{1}{\left(1 + (H_{rms} / \gamma h)^2\right)^{5/2}} \right] \quad (2.1)$$

where, ρ is the water density (1030 kg/m³), g is the gravity acceleration (9.81 m/s²), B is the breaker coefficient (~ 1), \bar{f} is the average frequency of waves, H_{rms} is the root-mean-square wave height, γ is the depth-limited breaking coefficient, h is the water depth. In this paper, we used f_p (0.25 Hz for the erosive case and 0.14 Hz for the accretive case) for \bar{f} . The wave energy dissipation model by Thornton and Guza (1983) was originally derived from a gentle slope and plane beach. However, this model also provided good agreement with data on a barred beach (e.g., Haines and Sallenger, 1994; Aagaard et al., 1998), even with a constant B in Equation (2.1). Figure 2.5b indicates that most of the wave energy is dissipated at the bar crest. Similar to Figure 2.5a, the temporal variation of $\langle \varepsilon_b \rangle$ shows that wave energy dissipation increases until E6. After that, $\langle \varepsilon_b \rangle$ shows a slight decrease in E10. The offshore bar migration without changing the bar shape (Figure 2.4) causes earlier breaking of larger waves, resulting in a decrease of $\langle \varepsilon_b \rangle$ in E10.

Figure 2.6 is similar to Figure 2.5 but for the accretive case where the bar is restored to a relatively planar beach. Waves break mostly at the bar crest, however, more waves pass the bar crest and break inside the surf zone as the bar decays with times. Consequently, the cross-shore location of maximum $\langle \varepsilon_b \rangle$ moves onshore from $x_{wG}=60.21$ m (A2) to $x_{wG}=63.87$ m (A6) as shown in Figure 2.6b.

The breaker types are typically classified by surf similarity parameter as follows (Battjes, 1974):

$$\xi_b = \frac{\tan \alpha_b}{\sqrt{H_b / L_0}} \quad (2.2)$$

where $\tan \alpha_b$ is the bottom slope in front of the breaking point, H_b is the significant wave height at the breaking point ($x_{wG}=60.21$ m), and L_0 is the deepwater wavelength. In Figure 2.7, ξ_b ranges 0.75~0.98 for the erosive case and 1.16~1.46 for the accretive case. In the erosive case, the increase of $\tan \alpha_b$ due to the bar development causes a gradual transition from spilling-type to plunging-type breakers, as shown by the increase of ξ_b . On the contrary, ξ_b decreases from 1.46 to 1.16 for the accretive case, implying that waves break in a more spilling manner as the beach evolves. As mentioned earlier, both types of breaking behavior (spilling and plunging) were observed for both cases. As runs elapsed, more spilling-type wave breakers were observed for the erosive case and more plunging-type wave breakers were observed for the accretive case.

2. 5 Wave breaking turbulence

2. 5. 1 Despiking

When wave breaking occurs, air bubbles penetrate into the water column and generate spike noises which cause unreliable estimates of the ADV data. Spike noises and turbulence in the velocity data look similar each other, therefore it is important to identify noise before estimating turbulence components from the velocity data. To detect spike noises, a signal-to-ratio (SNR) threshold and the 3D phase-space threshold method by Mori et al. (2007) were used for the velocity data. A SNR threshold of 10 dB was used first to identify spike noise, and then the 3D phase-space threshold method was used for the data which were not identified by the SNR threshold. If any component of u , v , or w was identified as a spike noise, all 3 components of velocity were identified as a spike noise. The percent of removed data is typically less than 10% out of the whole data, except near the wave trough level, i.e., ADV6, because of aeration by the bores. After spiked noises were identified, an interpolation between valid data was used to replace them. If the duration of the spike was less than 0.26 s, then the spike was replaced using linear interpolation. If the duration of the spike was greater than 0.26 s then the spike was replaced with a running mean of 0.26 s.

2. 5. 2 Turbulence estimate by the ST01 method

The measured instantaneous velocity u can be considered to consist of a mean component (\bar{u}), an organized wave component (\tilde{u}), and a turbulent component (u') as

$$u = \bar{u} + \tilde{u} + u' . \quad (2.3)$$

By simply taking average over the entire instantaneous velocity u , \bar{u} can be obtained. To separate the wave motion \tilde{u} and the turbulent motion u' , the ST01 method is used here. The basic assumption of the ST01 method is that incoherent signals between two ADVs are turbulence, while coherent signals are wave motion. Following is the brief description of the ST01 method.

The filtering operation can be expressed as a convolution

$$\hat{U}_1(t) = \int_{-T/2}^{T/2} h_f(t-\tau)U_2(t)d\tau \quad (2.4)$$

where, \hat{U}_1 is a filtered velocity at position (1), U_2 is a velocity at position (2), T is a filter length, and h_f is a filter weight. To predict the wave motion (\hat{U}_1), a least square filter is used for h_f . A vector of least square filter weights ($\hat{\mathbf{h}}$) is provided in a matrix form as introduced in ST01

$$\hat{\mathbf{h}} = (\mathbf{A}^T \mathbf{A})^{-1} \mathbf{A}^T \mathbf{U}_1 \quad (2.5)$$

where, \mathbf{A} is an M (the number of data points)-by- N (the number of filter weights) data matrix at position (2) and \mathbf{U}_1 is the instantaneous velocity vector at position

(1). The coherent wave velocity vector at position (1), $\hat{\mathbf{U}}_1$, is predicted by convolving the matrix \mathbf{A} with the least square filter weights ($\hat{\mathbf{h}}$)

$$\hat{\mathbf{U}}_1 = \mathbf{A}\hat{\mathbf{h}} \quad (2.6)$$

Then, the vector of turbulence component, $\Delta\hat{\mathbf{U}}$, can be computed by

$$\Delta\hat{\mathbf{U}} = \mathbf{U}_1 - \hat{\mathbf{U}}_1 \quad (2.7)$$

With the least square filter, the coherent wave motion is predicted more appropriately by reducing the difference in velocity magnitude and phase between the two vertically located ADVs.

Figure 2.8 shows the temporal variation of instantaneous u , v , w and squared turbulent component u'^2 , v'^2 , w'^2 at $\zeta = 0.50$ m, where u' , v' , w' are the turbulent velocity components in the cross-shore, alongshore, and vertical direction. In Figures 2.8a, 2.8c, and 2.8e, the coherent wave motion is predicted with the velocity data at ADV5. Note that since there is no input of wave motion in the alongshore direction, the coherent wave motion is almost zero throughout the time series in Figure 2.8c. By the definition, the difference between the instantaneous velocity and the coherent wave motion velocity results in turbulence. Figures 2.8b, 2.8d, and 2.8f show examples of the temporal variation of squared turbulence estimates. For a comparison, the results from the T98 method are also provided. Note that turbulence estimates by the T98 method is calculated by the direct differencing of velocity data at ADV6 and ADV5, while the least square

filter is applied in the ST01 method. The ST01 method shows smaller turbulence estimates than the T98 method, as expected. The time-averaged turbulence intensities from the ST01 method are: $\overline{u'^2} = 247.77 \text{ cm}^2/\text{s}^2$ ($272.14 \text{ cm}^2/\text{s}^2$), $\overline{v'^2} = 61.57 \text{ cm}^2/\text{s}^2$ ($97.60 \text{ cm}^2/\text{s}^2$), and $\overline{w'^2} = 172.73 \text{ cm}^2/\text{s}^2$ ($195.24 \text{ cm}^2/\text{s}^2$), where the results from the T98 method are provided in parentheses. The ST01 method reduces the time-averaged turbulence intensities of the T98 method by 9.0% for $\overline{u'^2}$, 36.92% for $\overline{v'^2}$, and 11.53% for $\overline{w'^2}$. The filter length (T) is chosen as a half of peak period (T_p) and time-averaged turbulence intensities show little sensitivity on the filter length of the ST01 method.

Figure 2.9 shows the squared coherence and the phase difference of the velocity data measured at ADV6 and ADV5 for E1. The figure can be used to investigate the distribution of estimated turbulence over frequencies, based on the assumption that incoherent signals between two ADVs are turbulence, while coherent signals are wave motion when using the ST01 method. Large values of the squared coherence of u near the peak frequency (0.25 Hz for the erosive case) in Figure 2.9a indicate that most of the coherent cross-shore motions are induced by the waves. The squared coherence decreases significantly in the high frequency range ($f > 1$ Hz), implying that most of high frequency fluctuation is estimated as turbulence. Corresponding to the squared coherence, the phase difference of u (Figure 2.9d) is nearly zero in the wave frequency range ($0.0625 \text{ Hz} < f < 1 \text{ Hz}$),

and deviates from zero in the high frequency range. In Figures 2.9b and 2.9e, the squared coherence of v is considerably reduced and the phase difference deviates from zero in all frequency range, as inferred from Figure 2.8c. In Figures 2.9c and 2.9f, the squared coherence and the phase difference of w show a similar tendency with u but the squared coherence in the wave frequency range shows lower value than u .

Figure 2.10 shows the power spectral densities (PSD) of high-passed (cut-off frequency: 0.0625 Hz) instantaneous velocity and turbulence velocity at ADV6 for E1. The coherent cross-shore and vertical wave components are removed effectively by the ST01 method as shown in the PSD of turbulent component (Figures 2.10a and 2.10c). In Figure 2.10b, the PSDs of the instantaneous and turbulent components of v are almost identical because most of alongshore motion is turbulence. It is noted that low frequency components ($f < 0.0625$ Hz) were removed before applying the ST01 method. The slope of the turbulence PSD is closely parallel with the Kolmogorov's slope of $-5/3$.

2. 5. 3 The application of the ST01 method to vertically spaced ADVs

As remarked earlier, the ST01 method is based on the assumption that the distance of two measuring points is larger than the length scale of turbulence but smaller than the length scale of waves. To satisfy this assumption, ST01 suggested that the distance between measuring points should be at least five times larger than the

elevation of the lower measuring point for turbulence to be uncorrelated. However, this suggestion is based on the data in the vicinity of the bottom (7 m above the bed at a water depth of 70 m) under non-wave-dominant conditions. On the other hand, Osler et al. (2004) applied the ST01 method in the laboratory experiment with horizontally spaced ADVs (20 cm, 50 cm, and 100 cm) and found that 100 cm separation was most appropriate for their study. These examples imply that ADV distances should be chosen carefully. In this section, we will investigate the appropriate pairs of ADVs at each elevation, among various combinations of ADVs to apply the ST01 method.

Figures 2.11 and 2.12 are similar to Figures 2.8 and 2.9, respectively, but ADV6 and ADV1 are used to show the effect of largely spaced ADVs. The distance between ADV6 and ADV1 is 49 cm, and the distance between ADV6 and ADV5 is 19 cm. Two significant tendencies are found with largely spaced ADVs. First, the vertical wave motion is unsuccessfully predicted with ADV1 (Figure 2.11e). This is because vertical wave motion decreases linearly toward bottom in shallow water and thus there is little vertical wave motion near the bottom. This is also supported by low squared coherence of w in the frequency range in Figure 2.12. Secondly, there exists ‘pseudo-turbulence’ in u as shown in the range of $337 \text{ s} < t < 345 \text{ s}$ in Figure 2.11a. Pseudo-turbulence is a low frequency fluctuation which is not a physical process but a result of the turbulence estimate method. Taking into account the fact that the low frequency components were removed before applying

the ST01 method, pseudo-turbulence should be minimized in the turbulence estimates. Pseudo-turbulence in the present study mainly arises from the large phase lag between the free stream (e.g., ADV6) and inside the wave bottom boundary layer (e.g., ADV1) in the cross-shore direction. The cross-shore velocity in the proximity of the bed (within an order of 10 cm) leads the phase of free stream velocity (Foster et al., 2000). Overall, if the ADV spacing is too large, then turbulence estimates can be overestimated. Hence, we use the adjacent ADVs to predict the vertical wave motion more closely and to minimize the pseudo-turbulence in the cross-shore velocity.

2. 5. 4 Time-averaged turbulence intensities and TKE

Figure 2.13 shows the vertical distributions of the Froude-scaled time-averaged turbulence intensities and TKE for E1. The time-averaged TKE per unit mass is defined as

$$\bar{k} = \frac{1}{2}(\overline{u'^2} + \overline{v'^2} + \overline{w'^2}) \quad (2.8)$$

where the overbar refers to the turbulent intensity averaged over the entire time series of the run. At each elevation except at ADV1 and ADV6, two estimates are obtained from the adjacent ADVs and then averaged. For a quantitative comparison, the results of the high-pass filtering (cut-off frequency: 1 Hz) and the T98 method are provided. The cut-off frequency for the high-pass filtering is selected based on the spectrum where the slope follows the Kolmogorov's $-5/3$

slope (see Figure 2.10) and is consistent with Scott et al., (2005). As pointed out by Svendsen (1987), the high-pass filtering provides a low estimate of the time-averaged TKE because this technique excludes large eddies which have lower frequencies than the cut-off frequency. The results of the ST01 method are larger than those of high-pass filtering approximately by a factor of 2. On the other hand, the ST01 method provides lower turbulent intensities than the T98 method because the least square filter reduces the wave bias in turbulence estimates. The reduced amount from the ST01 method is relatively constant (e.g., ~ 0.005 for $(\bar{k} / gh)^{1/2}$) over the water depth. For all three methods, the vertical distributions show that $(\overline{u'^2} / gh)^{1/2}$ and $(\overline{w'^2} / gh)^{1/2}$ decrease toward the bottom, while $(\overline{v'^2} / gh)^{1/2}$ is relatively constant over water depth. Consequently, the magnitudes of $(\bar{k} / gh)^{1/2}$ are the largest near the free surface level and diminish toward the bottom.

Figure 2.14 shows a comparison of the vertical structure of $(\bar{k} / gh)^{1/2}$ between Scott et al. (2005) and the present study (CROSSTEX) under similar wave conditions. The target wave height and wave period are 0.6 m and 4 s, respectively. The only difference in the wave condition is the peak enhancement factor: $\gamma = 20$ for Scott et al. (2005) and $\gamma = 3.3$ for the present study. P4 in Scott et al. (2005) and E11 in the present study are compared, which were measured at the bar crest. Similarly, P5 in Scott et al. (2005) and E10 in the present study are compared to represent $(\bar{k} / gh)^{1/2}$ at the bar trough. Note that water depths are 0.69 m at the bar

crest (P4) and 0.99 m at the bar trough (P5) in Scott et al. (2005). At the bar crest, the depth-averaged values of $(\bar{k} / gh)^{1/2}$ are of a similar magnitude (~ 0.04), although there is more vertical variation in the CROSSTEX data. This is because of similar intensities of wave breaking at the bar crest. At the bar trough, however, $(\bar{k} / gh)^{1/2}$ in the present study is larger approximately by a factor of 1.5 because of the shorter distance from the bar crest to trough in the present study (less than 3 m) than Scott et al. (2005) (~ 6 m).

2. 5. 5 Observation of turbulence over an evolving bottom

Figures 2.15a and 2.15c show the vertical distribution of $(\bar{k} / gh)^{1/2}$ at the bar trough region for the erosive and accretive cases, respectively. As the beach evolves, it is observed that $(\bar{k} / gh)^{1/2}$ decreases for the erosive case, while it is generally increasing for the accretive case. These temporal variations of $(\bar{k} / gh)^{1/2}$ in the water column can be associated with the energy dissipation of waves and will be shown in Figure 2.16. Additionally, Figures 2.15b and 2.15d show the vertical distribution of nondimensionalized turbulence dissipation rate $(\varepsilon h / (gh)^{3/2})$. The turbulence dissipation rate (ε) is estimated using the method by Trowbridge and Elgar (2001) as follows.

$$\varepsilon = \left[\frac{55}{21} (P_{uu}(f) + P_{vv}(f) - noise) \cdot (2\pi f)^{5/3} V^{-2/3} \alpha^{-1} I\left(\frac{\sigma}{V}, \theta\right)^{-1} \right]^{3/2} \quad (2.9)$$

$$\varepsilon = \left[\frac{55}{12} (P_{ww}(f) - noise) \cdot (2\pi f)^{5/3} V^{-2/3} \alpha^{-1} I\left(\frac{\sigma}{V}, \theta\right)^{-1} \right]^{3/2} \quad (2.10)$$

where, P_{uu} , P_{vv} , and P_{ww} are power spectral densities, f is frequency, α is the empirical Kolmogorov constant (~ 1.5), V is the magnitude of the current, σ^2 is the variance of the wave-induced horizontal velocity, θ is the angle between waves and current and $I(\frac{\sigma}{V}, \theta)$ is the function defined as following

$$I\left(\frac{\sigma}{V}, \theta\right) = \frac{1}{\sqrt{2\pi}} \left(\frac{\sigma}{V}\right)^{2/3} \int_{-\infty}^{+\infty} \left[x^2 - 2\frac{V}{\sigma} \cos(\theta)x + \frac{V^2}{\sigma^2} \right]^{1/3} \exp\left(-\frac{1}{2}x^2\right) dx. \quad (2.11)$$

The equations (9) and (10) are estimated in the range of $3 \text{ Hz} < f < 10 \text{ Hz}$ with noise level of $1.0 \times 10^{-5} \text{ m}^2/\text{s}^2$, and then averaged. As opposed to $(\bar{k} / gh)^{1/2}$, $\varepsilon h / (gh)^{3/2}$ increases for the erosive case as the beach evolves. However, for the accretive case, $\varepsilon h / (gh)^{3/2}$ increases near the water surface, whereas it decreases near the bottom.

Figure 2.16 shows the relation between $\bar{K}^{1/2}$ and $(\langle \varepsilon_b \rangle / \rho)^{1/3}$ at the bar trough region, where \bar{K} is the depth-averaged \bar{k} . The observations of $(\bar{k} / gh)^{1/2}$ are fitted to an exponential curve (e.g., Svendsen, 1987; Roelvink and Stive, 1989; Kobayashi et al., 2005)

$$\sqrt{\frac{\bar{k}}{gh}} = a \exp\left(b \frac{\zeta}{h}\right) \quad (2.12)$$

where, a and b are fitting coefficients. From this, \bar{K} is calculated as

$$\bar{K} = \frac{1}{h} \int_0^h \bar{k} d\zeta . \quad (2.13)$$

This figure shows a similar order-of-magnitude between $\bar{K}^{1/2}$ and $(\langle \varepsilon_b \rangle / \rho)^{1/3}$, as proposed by Battjes (1975), under the assumption that production and dissipation of turbulence are locally in equilibrium. Quantitatively, $\bar{K}^{1/2}$ is approximately one half of $(\langle \varepsilon_b \rangle / \rho)^{1/3}$. This supports the hypothesis that wave energy dissipation is the main source of TKE production in the surf zone (e.g., Thornton and Guza, 1983; Govender et al., 2004). In this sense, the decreasing $(\bar{k} / gh)^{1/2}$ for the erosive case can be associated with the decreasing wave energy dissipation at the bar trough (Figure 2.5b). As the bar develops, more wave energy is dissipated at the bar crest and less wave energy is transported to the bar trough. Consequently, smaller values of $(\bar{k} / gh)^{1/2}$ are observed at the bar trough.

Figure 2.17 shows the vertical structures of $(\bar{k} / gh)^{1/2}$ and $\varepsilon h / (gh)^{3/2}$ at the bar crest (Figures 2.17a and 2.17b) and at the bar trough (Figures 2.17c and 2.17d) for the accretive case. The magnitudes of $(\bar{k} / gh)^{1/2}$ near the water surface at the bar crest are larger than at the bar trough approximately by a factor of 2, as a result of intense wave breaking at this location. One thing to notice is that the vertical distribution of $(\bar{k} / gh)^{1/2}$ at the bar crest (A5) shows a large increase near the bottom, whereas $(\bar{k} / gh)^{1/2}$ near the bottom at the bar trough (A2) decreases. This can be attributed to a strong cross-shore root-mean-square (RMS) velocity at the

bar crest. The average and standard deviation of cross-shore RMS velocities near the bed (ADV1, 2, and 3) in the wave frequency range ($0.0625 \text{ Hz} < f < 1 \text{ Hz}$) are $0.4227 \pm 0.0139 \text{ m/s}$ at the bar crest and $0.2935 \pm 0.0280 \text{ m/s}$ at the bar trough.

Similar to $(\bar{k} / gh)^{1/2}$, the magnitudes of $\varepsilon h / (gh)^{3/2}$ near the water surface at the bar crest are larger than at the bar trough (Figures 2.17b and 2.17d). A large increase of $\varepsilon h / (gh)^{3/2}$ is also observed near the bed at the bar crest. Especially, in A5 in Figure 2.17b, $\varepsilon h / (gh)^{3/2}$ near the bed are observed to be larger than at the water surface level, approximately by a factor of 4.

2. 5. 6 Observation of turbulence over a quasi-equilibrium bottom

Figure 2.18 and Figure 2.19 show the cross-shore and vertical distribution of $(\bar{k})^{1/2}$ and ε inside the surf zone. In these figures, the beach profiles for E7~E11 and A5~A9 are averaged for the erosive and accretive cases, respectively. Both figures represent a similar tendency inside the surf zone. The magnitudes of $(\bar{k})^{1/2}$ and ε at the bar trough ($x_{ADV} = 63.70 \text{ m}$ for the erosive case; $x_{ADV} = 65.64 \text{ m}$ for the accretive case) are smaller than those at other locations in the surf zone. The rapid increase of water depth (or water mass) enhances TKE to spread with more water mass. For E7 and A7, $(\bar{k})^{1/2}$ and ε near the water surface increase again, owing to a second wave breaking on a shallow water depth. The significant intensities of $(\bar{k})^{1/2}$ and ε are observed inside the surf zone.

The anisotropic characteristics of wave breaking turbulence over water depth are also examined for all cross-shore locations. Table 2.2 shows the ratio of $\overline{u'^2} : \overline{v'^2} : \overline{w'^2}$ normalized by $2\overline{k}$. Inside the surf zone (e.g., E7, E8, E9, A7, and A8), the anisotropic characteristics are similar with a plane wake ($\overline{u'^2} : \overline{v'^2} : \overline{w'^2} = 0.42:0.26:0.32$) near the water surface, consistent with Svendsen (1987). Toward the bottom, the anisotropic features become close to inner boundary layer flow ($\overline{u'^2} : \overline{v'^2} : \overline{w'^2} = 0.62:0.28:0.10$), due to the influence of the bed, as also noted by Scott et al. (2005). Near the water surface at the bar crest ($\zeta = 0.50$ and 0.31 m for E11, A9, and A5), $\overline{u'^2}$ is approximately 30% larger and $\overline{v'^2}$ is approximately 50% smaller than other locations. From this, it can be conjecture that the anisotropic (especially two-dimensional) turbulence at breaking point is transformed into more isotropic turbulence toward inner surf zone.

2.6 Discussion

As previously noted, turbulence intensities are strongly associated with wave energy dissipation. In this section, we will discuss more possible factors which affect the reduced turbulence intensities for the erosive case. These can be: 1) the transition of breaking types from spilling to plunging; 2) the increase of horizontal distance from the bar crest to the bar trough, and 3) the increase of water depth at the bar trough.

2. 6. 1 The transition of breaking types

A more comprehensive investigation of the vertical distribution of wave breaking turbulence can be accomplished by using Equation (12). The coefficients a and b represent $(\bar{k} / gh)^{1/2}$ at the bottom and the curvature of the fitting curve, respectively. Figure 2.20 shows an example of the curve fitting with Equation (12). Runs are selected when ADVs are located at bar trough ($x_{ADV} = 63.70$ m), but E4 and E5 are excluded due to lack of ADV1 data. All turbulence estimates are fitted closely to the exponential curve with $R^2 = 0.99$. It is found that lesser amount of TKE is transported to the bottom, as shown with the decreasing a by 15.4% from E1 to E10. Relating to the surf similarity parameter in Figure 2.7, it can be hypothesized that the gradual transition of breaker type from spilling to plunging lessen the amount of transported TKE near the bottom. The evolution of vertical distribution of $(\bar{k} / gh)^{1/2}$ can be associated with turbulence transport mechanism of each breaker type.

Ting and Kirby (1995, 1996) suggested that the mechanism of energy transfer from organized wave motion to turbulence is primarily different between spilling and plunging breakers. In a spilling breaker, wave breaking turbulence is generated almost throughout the whole wave cycle and is transported toward the bottom slowly by large strain rates (Ting and Kirby, 1996). Because of the long time scale of turbulence and slow mixing in the water column, turbulence intensities at any

given time is relatively constant due to the advected turbulence of the preceding breakers (Svendsen, 1987). On the contrary, in a plunging breaker, wave breaking turbulence is generated immediately after the wave has broken and is transported by large vortex-like eddies (Ting and Kirby, 1995). The large vortex-like eddies transport turbulence to the bottom instantaneously, with much smaller time scale than that of spilling breakers. Hence, in time-averaged point of view, turbulence intensity in the water column in spilling breaker is relatively uniform over depth than that of plunging breakers. This is supported by the curve fitting coefficients in Figure 2.20. As more waves break by plunging-type with elapsed runs, b increases by 10.9 % from E1 to E10, which means a larger vertical variation of $(\bar{k} / gh)^{1/2}$, indicating that smaller portion of wave breaking turbulence near the water surface level is transported to the bottom.

In addition to the inherent difference of turbulence transport mechanism, more TKE is confined in upper region of water column in plunging breakers. For example, Ting and Kirby (1995) observed strong upward flow underneath the wave front in plunging breakers. Mori et al. (2007), from their experimental study of air bubbles, pointed out that the strong wave breaking which is the case of plunging breakers in their experiment, entrap a larger volume of air and this large-size bulk of air can rise faster.

2. 6. 2 The increase of horizontal distance from the bar crest to the bar trough

The offshore migration of the bar crest also may affect the reduced magnitudes of $(\bar{k} / gh)^{1/2}$ at the bar trough. Although the offshore migration of breaking point was not detected due to the sparse cross-shore distribution of wave gauges, it is expected that wave breaking occur offshore corresponding to the offshore bar migration. This is found in Figure 2.6a and 2.6b, in which the reduction of wave breaking height in E11 is believed as a result of offshore movement of the bar without changing of the bar shape. Because of offshore wave breaking of large waves and resulting longer distance of dissipation and spread of TKE, smaller $(\bar{k} / gh)^{1/2}$ would be observed at the bar trough as the beach evolves.

2. 6. 3 The increase of water depth at the bar trough

As runs elapsed, the bar trough deepened. The water depths at the bar trough are decreasing from E1 to E10 (Table 2.1) and the change of wave trough level (less than 1 cm) is negligibly small. This indicates that the increased vertical distance between the wave trough level, where TKE is mainly produced by wave breaking, and the measuring point is partially attributed to smaller TKE.

2. 7 Conclusions

This paper presents the experimental observations of wave breaking turbulence in response to an evolving beach during the CROSSTEX. The observations include synoptic measurements of wave height, fluid velocity, and morphology for 11 erosive and 9 accretive runs in the surf zone. It was found that the temporal

evolution of morphology, wave breaking, and turbulence are closely related to each other. The main conclusions drawn from this study are stated below.

- (1) The beach evolves to the quasi-equilibrium state in approximately 100 minutes (1500 T_p for the erosive case, 857 T_p for the accretive case) for both cases. The quasi-equilibrium state is defined when H_{bar} / W_{bar} is stable. The bar crest migrates slowly offshore for the erosive case and onshore for the accretive case even in the quasi-equilibrium state.
- (2) Wave breaking characteristics, such as wave breaking height, the average rate of energy dissipation by bores ($\langle \varepsilon_b \rangle$), and the surf similarity parameter, are observed in response to morphodynamics. As the beach evolves for the erosive case, wave breaking heights and $\langle \varepsilon_b \rangle$ increase at the bar crest during the bar development. At the bar trough, wave heights and $\langle \varepsilon_b \rangle$ decrease due to the increase of wave energy dissipation at the bar crest. On the contrary, wave heights and $\langle \varepsilon_b \rangle$ decrease at the bar crest and increase at the bar trough for the accretive case, implying more waves pass the bar crest and break inside the surf zone as the beach becoming a planar beach. The surf similarity parameter increases for the erosive case and decreases for the accretive case. This indicates that the waves break in a more plunging manner for the erosive case and in a spilling manner for the accretive case as the beach evolves, and was generally consistent with observations.

- (3) For E1, the vertical distribution of $(\bar{k} / gh)^{1/2}$ from the ST01 method is larger than the high-pass filtering method (cut-off frequency: 0.0625 Hz) by a factor of 2 but smaller than those of the T98 method by approximately 10~15% over water depth. Also, $(\bar{k} / gh)^{1/2}$ at the bar crest and trough are compared with Scott et al., (2005), in which the experiment was conducted under similar wave condition on a fixed bed. Depth-averaged $(\bar{k} / gh)^{1/2}$ at the bar crest are of similar magnitude, while the present study shows larger $(\bar{k} / gh)^{1/2}$ than Scott et al., (2005) by a factor of 1.5, at the bar trough. This is because of a smaller distance from the bar crest to trough in the present study.
- (4) The vertical distribution of $(\bar{k} / gh)^{1/2}$ and $\varepsilon h / (gh)^{3/2}$ are observed at the bar trough over an evolving beach. For the erosive case, $(\bar{k} / gh)^{1/2}$ decreases whereas $\varepsilon h / (gh)^{3/2}$ increases as the bar develops. From the relation between $(\bar{K})^{1/2}$ and $(\langle \varepsilon_b \rangle / \rho)^{1/3}$, the turbulence intensity is closely related to the wave energy loss by wave breaking. Besides the changes in $\langle \varepsilon_b \rangle$ at the bar trough, the transition of wave breaking types, the increase of horizontal distance from the bar crest to trough, and the increased water depth at the bar trough are discussed as contributing factors for decreasing turbulence intensity near the bed in the erosive case.

- (5) Comparing to the bar trough, the vertical distribution of $(\bar{k} / gh)^{1/2}$ at the bar crest shows a large increase near the bottom, resulting from a strong cross-shore RMS velocity.
- (6) In the quasi-equilibrium state, $(\bar{k})^{1/2}$ and ε at the bar trough are smaller than those inside the surf zone. This is due to the rapid increase of water depth at the bar trough, where the spread of TKE are enhanced by the increased water mass. Inside the surf zone, strong intensities of $(\bar{k})^{1/2}$ and ε are observed due to a second breaking on a shallow water depth.

Acknowledgements

This work was supported by the National Science Foundation (OCE-0351741).

The authors are grateful to all participants during the CROSSTEX project and the staff at the O. H. Hinsdale Wave Research Laboratory.

References

- Aagaard, T., J. Nielsen, and B. Greenwood, 1998, Suspended sediment transport and nearshore bar formation on a shallow intermediate-state beach, *Marine Geology*, 148, 203–225.
- Bailard, J. A., 1981, An energetics total load sediment transport model for a plane sloping beach, *J. Geophys. Res.*, 86, 10938-10964.

- Battjes, J. A. 1974. Surf similarity, *Proceedings of the 14th International Conference on Coastal Engineering*. ASCE, New York, 466-480.
- Battjes, J. A., 1975. Modeling of turbulence in the surf zone, paper presented at *Symposium on Modeling Techniques* Am. Soc. Of Civ. Eng., San Francisco, California.
- Blenkinsopp, C. E, and J. R. Chaplin. 2008. The effect of relative crest submergence on wave breaking over submerged slopes, *Coastal Eng.*, 55, 967-974.
- Bowen, A. 1981. Simple models of nearshore sedimentation: Beach profiles and longshore bars, *Coastline Can.*, 80-10, 1-11.
- Bouws, E., H. Gunther, W. Rosenthal, and C. L. Vincent. 1985. Similarity of the wind wave spectrum in finite depth water, Part I- Spectral form, *J. Geophys. Res.*, 90 (C1), 975-986.
- Chang, K, -A., and P. L. -F. Liu. 1999. Experimental investigation of turbulence generated by breaking waves in water of intermediate depth, *Physics of fluids*, 11, 3390-3400.
- Cox, D. T., N. Kobayashi, and A. Okayasu. 1995. *Experimental and numerical modeling of surf zone hydrodynamics*, Res. Report CACR-95-07, Center for Applied Coastal Research, University of Delaware, 293 pp.
- Cox, D.T. and Kobayashi, N., 1998, Application of an Undertow Model to Irregular

- Waves over Plane and Barred Beach, *Journal of Coastal Research*, 14 (4), 1314-1324.
- Dally, W. R., and R. G. Dean, 1984, Suspended sediment transport and beach profile evolution, *J. waterway, Port, Coastal and Ocean Engineering.*, 110, 15-33.
- Elgar, S., R.T. Guza, B. Raubenheimer, T.H.C. Herbers, and E. L. Gallagher, 1997, Spectral evolution of shoaling and breaking waves on a barred beach, *J. Geophys. Res.*, 102 (C7), 15797-15805.
- Feddersen, F., and A. J. Williams III, 2007, Direct estimation of the Reynolds stress vertical structure in the nearshore, *J. Atmos. Oceanic Technol.*, 24, 102-116.
- Foster, D. L., R. A. Beach, and R. A. Holman, 2000, Field observations of the wave bottom boundary layer, *J. Geophys. Res.*, 105(C8), 19,631-19,647.
- Fredsøe, J., and R. Deigaard. 1998. *Mechanics of Coastal Sediment Transport*, World Scientific Publishing, Singapore, 369 pp.
- Gallagher, E.L., S. Elgar and R.T. Guza, 1998, Observations of sand bar evolution on a natural beach, *J. Geophys. Res.*, 103 (C2), 3203–3215.
- Garcez Faria, A.F., E.B.Thornton, T.C.Lippmann, and T.P.Stanton, 2000, Undertow over a barred beach, *J. Geophys. Res.*, 105 (C7), 16,999–17,010.
- George, R., R. E. Flick, and R. T. Guza. 1994. Observations of turbulence in the surf zone, *J. Geophys. Res.*, 99 (C1), 801-810.

- Goring, D. G., and V. I. Nikora. 2002. Despiking acoustic Doppler velocimeter data, *J. Hydraul. Eng.*, 128 (1), 117-126.
- Govender, K., G. P. Mocke, and M. J. Alport, 2002, Video-imaged surf zone wave and roller structures and flow fields, *J. Geophys. Res.*, 107(C7), 3072.
- Govender, K., H. Michallet, M.J. Alport, U. Pillay, G.P. Mocke, and M. Mory, 2009. Video DCIV measurements of mass and momentum fluxes and kinetic energies in laboratory waves breaking over a bar, *Coastal Eng.*, 56, 876-885.
- Haines, J.W. and A. H. Sallenger Jr., 1994, Vertical structure of mean cross-shore currents across a barred surf zone, *J. Geophys. Res.*, 99 (C7), 14,223–14,242.
- Haller, M. C., R. A. Dalrymple, and I. A. Svendsen, 2002, Experimental study of nearshore dynamics on a barred beach with rip channels, *J. Geophys. Res.*, 107 (C6), 3061, doi:10.1029/2001JC000955
- Holman, R. A., 1995. *Nearshore processes*, Review of geophysics, Supplement, July 1995, 1237-1247.
- Huang, Z.-C., S.-C. Hsiao, H.-H. Hwung, and K.-A. Chang, 2009. Turbulence and energy dissipations of surf-zone spilling breakers, *Coastal Eng.*, 56, 733-746.
- Hughes, S. A., 1998, *Physical models and laboratory techniques in coastal engineering*, World Scientific, 568 pp.
- Kimmoun, O., and H. Branger. 2007. A particle image velocimetry investigation on laboratory surf-zone breaking waves over a sloping beach, *J. Fluid Mech.*, 588, 353-397.

- Kobayshi, N., H. Zhao, and Y. Tega, 2005, Suspended sand transport in surf zone, *J. Geophys. Res.*, *110*, C12009
- Kuriyama, Y., 2002, Medium-term bar behavior and associated sediment transport at Hasaki, Japan, *J. Geophys. Res.*, *107* (C9), 3132, doi:10.1029/2001JC000899.
- Marino-Tapia, I.J., P.E.Russell, T.J.O'Hare, M.A. Davidson, and D.A.Huntley, 2007a, Cross-shore sediment transport on natural beaches and its relation to sandbar migration patterns: 1. Field observations and derivation of a transport parameterization, *J. Geophys. Res.*, *112*, C03001, doi:10.1029/2005JC002893.
- Marino-Tapia, I.J., P.E.Russell, T.J.O'Hare, M.A. Davidson, and D.A.Huntley, 2007b, Cross-shore sediment transport on natural beaches and its relation to sandbar migration patterns: 2. Application of the field transport parameterization, *J. Geophys. Res.*, *112*, C03002, doi:10.1029/2005JC002894.
- Melville, W. K., F. Veron, and C. J. White. 2002. The velocity field under breaking waves: coherent structures and turbulence, *J. Fluid Mech.*, *454*, 203-233.
- Mocke, G. P., 2001, Structure and modeling of surf zone turbulence due to wave breaking., *J. Geophys. Res.*, *106*(C8), 17,039-17,057.
- Mori, N., T. Suzuki, and S. Kakuno. 2007. Noise of acoustic Doppler velocimeter data in bubbly flows, *J. of Engrg Mech.*, *133*, 122-125
- Mori, N., T. Suzuki, and S. Kakuno. 2007. Experimental study of air bubbles and turbulence characteristics in the surf zone, *J. Geophys. Res.*, *112*, C05014.

- Nadaoka, K., M. Hino, and Y. Koyano. 1989. Structure of the turbulent flow field under breaking waves in the surf zone, *J. Fluid Mech.*, 204, 359-387.
- Nadaoka, K., and T. Kondoh. 1982. Laboratory measurements of velocity field structure in the surf zone by LDV, *Coastal Eng. in Japan*, 25, 125-146.
- Osler, M. S., I. A. Svendsen, and J.T. Kirby. 2004. A Laboratory Investigation of Nearshore Turbulence. *Proceedings of the 29th International Conference on Coastal Engineering*, ASCE, 2,1393-1403.
- Rodriguez, A, A. Sánchez-Arcilla, J. M. Redondo, and C. Mösso. 1999. Macroturbulence measurements with electromagnetic and ultrasonic sensors: a comparison under high-turbulent flows, *Experiments in fluids*, 27, 31-42.
- Roelvink, J.A, and I. Broker, 1993, Cross-shore profile models, *Coastal Engineering*, 21, 163–191.
- Roelvink, J. A. and M. J. F. Stive. 1989, Bar-generating cross-shore flow mechanism on a beach, *J. Geophys. Res.*, 94 (C4), 4785-4800.
- Scott, C. P., D. T. Cox, T. B. Maddux, and J. W. Long. 2005. Large-scale laboratory observations of turbulence on a fixed barred beach, *Meas. Sci. Technol.* 16, 1903-1912.
- Scott, C. P., D. T. Cox, S. Shin, and T. B. Maddux. 2006. The role of wave breaking turbulence in sediment suspension observed during CROSSTEX, *Proceedings of the 30th International Conference on Coastal Engineering*. ASCE, 3, 2537-2546.

- Shaw, W. J., and J. Trowbridge. 2001. The direct estimation of near-bottom turbulent fluxes in the presence of energetic wave motions, *J. Atmos. Oceanic Technol.*, 18, 1540-1557.
- Smith, E. R., and N. C. Kraus, 1991, Laboratory study of wave-breaking over bars and artificial reefs, , *J. waterway, Port, Coastal and Ocean Engineering.*, 117, 307-325.
- Stive M. J. F., 1980. Velocity and pressure field in spilling breakers, *Proceedings of the 17th International Conference on Coastal Engineering*. ASCE, 1, 547-566
- Svendsen, I. A. 1987. Analysis of surf zone turbulence, *J. Geophys. Res.*, 92 (C5), 5115-5124.
- Tennekes, H., and J. L. Lumley, 1972, *A First Course in Turbulence*, MIT Press, 300pp
- Thornton, E.B. and R.T. Guza, 1983, Transformation of wave height distribution, *J. Geophys. Res.*, 88 (C10), 5925–5938.
- Thornton, E.B., R.T. Humiston, and W. Birkemeier, 1996, Bar/trough generation on a natural beach, *J. Geophys. Res.*, 101 (C5), 12,097-12,110.
- Thornton, E.B., R.A. Dalrymple, T. Drake, E. Gallagher, R.T. Guza, A. Hay, R.A. Holman, J. Kaihatu, T.C. Lippmann, and T. Özkan-Haller. 2000. State of nearshore processes research: II, *Technical Report NPS-OC-00-001*, Naval Postgraduate School, Monterey, CA, 37 pp.

- Ting, F. C. K., and J. T. Kirby. 1994. Observation of undertow and turbulence in a laboratory surf zone, *Coastal Eng.*, 24, 51-80.
- Ting, F. C. K., and J. T. Kirby. 1995. Dynamics of surf-zone turbulence in a strong plunging breaker, *Coastal Eng.*, 24, 177-204.
- Ting, F. C. K., and J. T. Kirby. 1996. Dynamics of surf-zone turbulence in a spilling breaker, *Coastal Eng.*, 27, 131-160.
- Trowbridge, J., 1998. On a technique for measurement of turbulent shear stress in the presence of surface waves, *J. Atmos. Oceanic Technol.*, 15, 290-298.
- Trowbridge, J., and S. Elgar. 2001. Turbulence measurements in the surf zone, *J. Phys. Oceanogr.*, 31, 2403-2417.
- Wang, P., B. A. Ebersole, E. R. Smith, and B. D. Johnson. 2002. Temporal and spatial variations of surf-zone currents and suspended sediment concentration, *Coastal Eng.*, 46, 175-211.

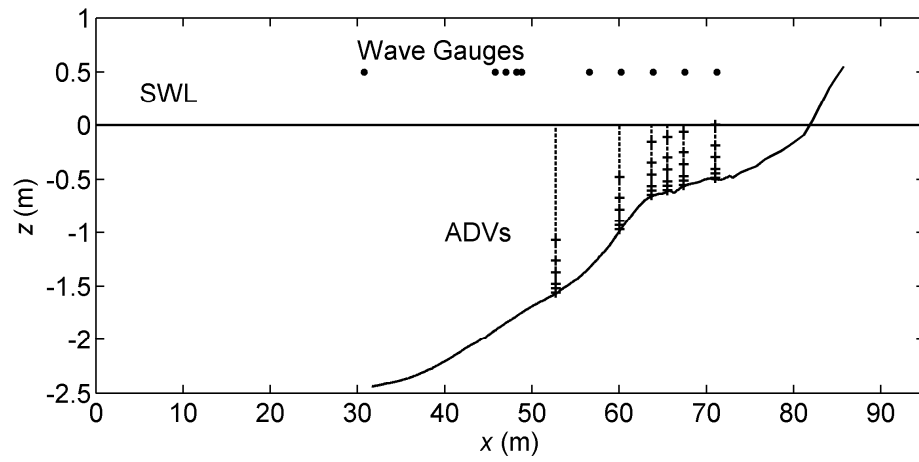


Figure 2.1: Sketch of experimental setup with initial bed profile before E1. Wavemaker is located at $x=0$ m.

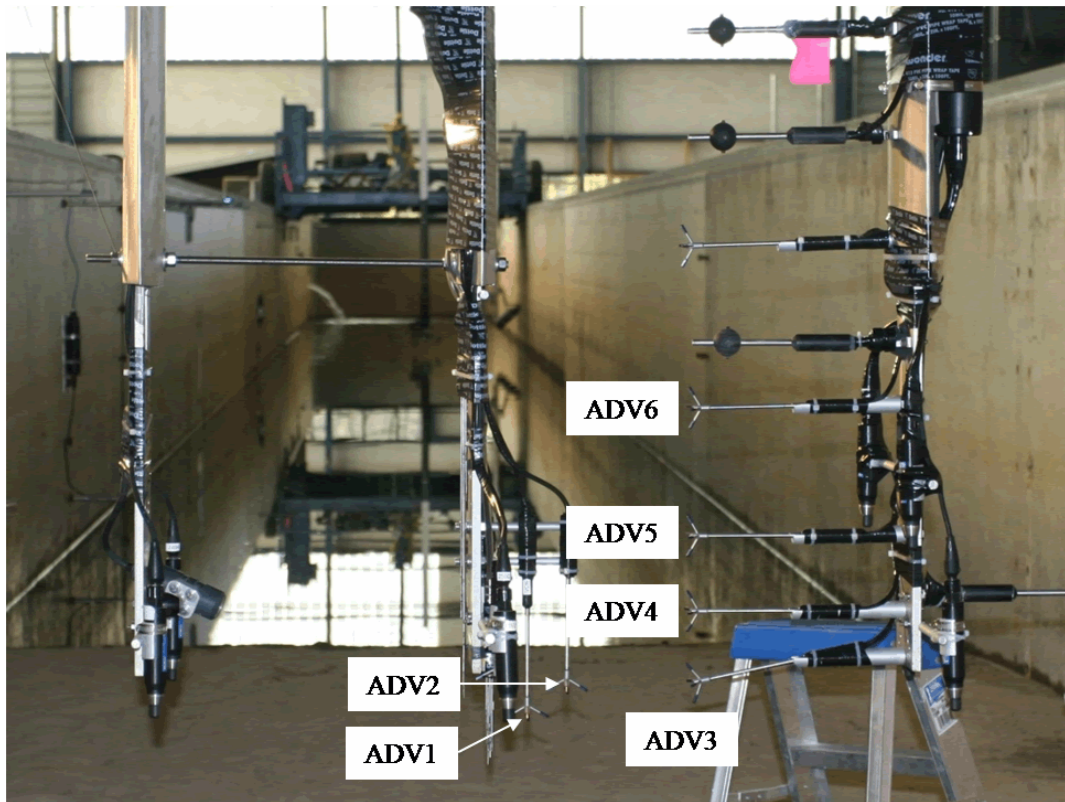


Figure 2.2: Photo of vertical stack of ADVs (modified from Scott et al., 2006).

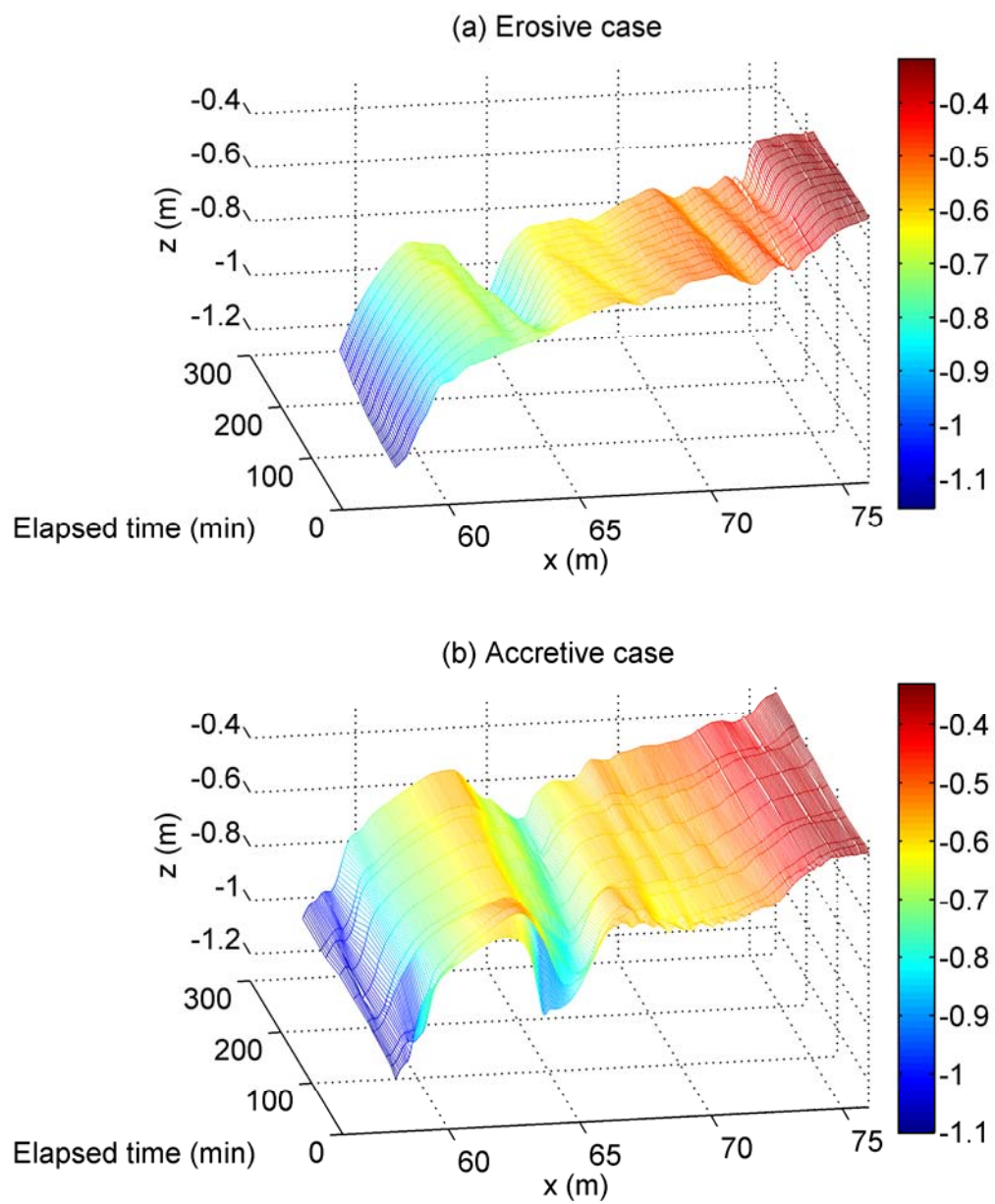


Figure 2.3: Mesh plot of beach profile evolution: (a) erosive case and (b) accretive case.

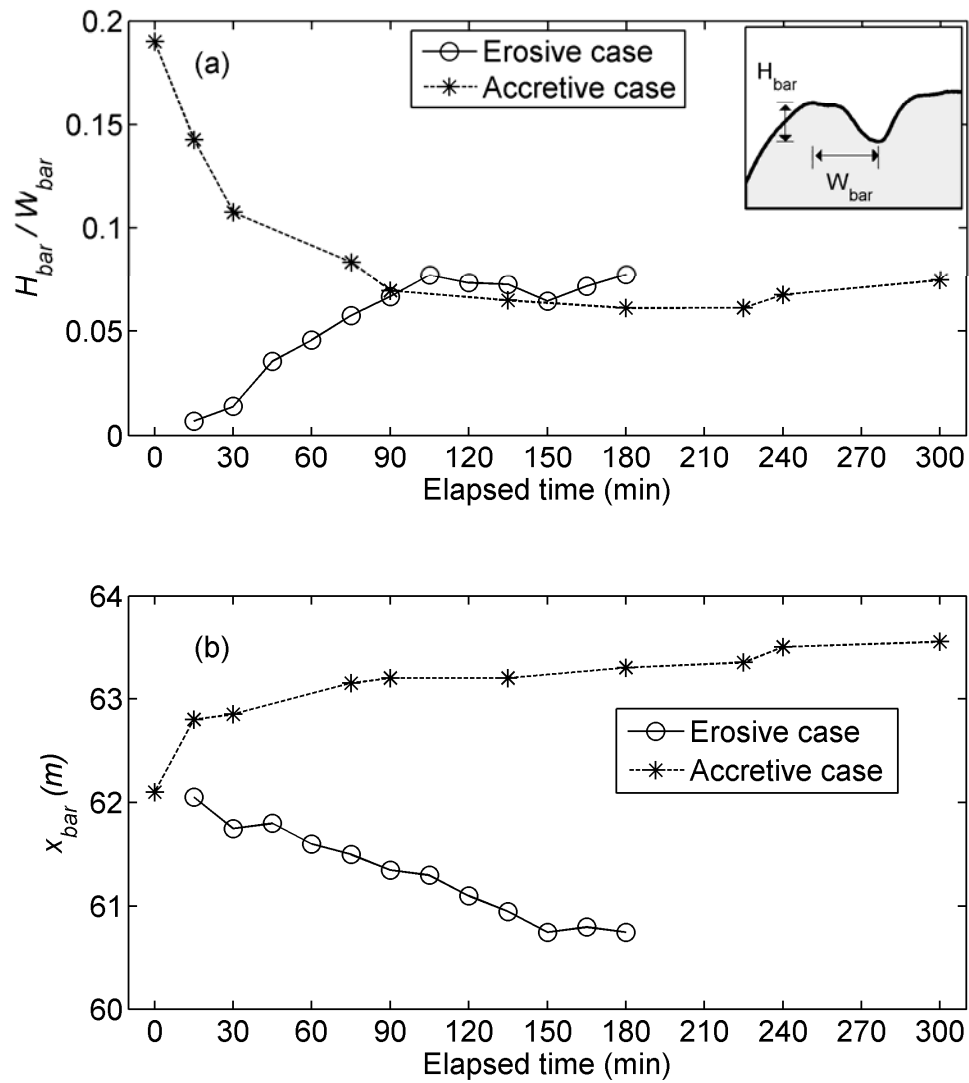


Figure 2.4: Time series of (a) bar shape parameter (H_{bar}/W_{bar}) and (b) bar cross-shore location (x_{bar}). Definition sketch of H_{bar}/W_{bar} is shown in upper right box in panel (a).

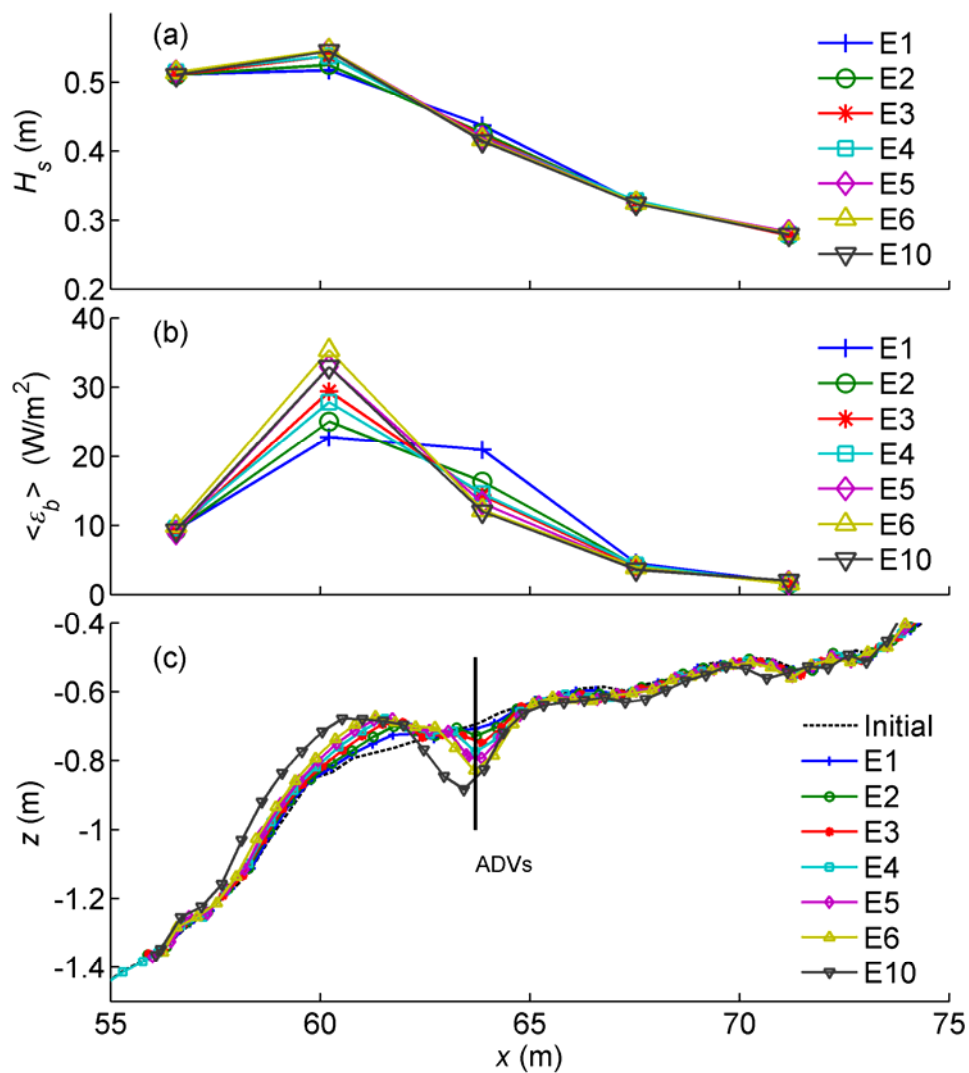


Figure 2.5: Cross-shore distributions of (a) significant wave height (H_s), (b) average rate of energy dissipation by bores $\langle \varepsilon_b \rangle$, and (c) bottom profiles averaged across the wave flume for erosive case. Runs are selected when ADVs are located at bar trough ($x_{ADV} = 63.70$ m). In panel (c), the initial bathymetry is indicated by dashed line and cross-shore location of ADVs is shown as a vertical line.

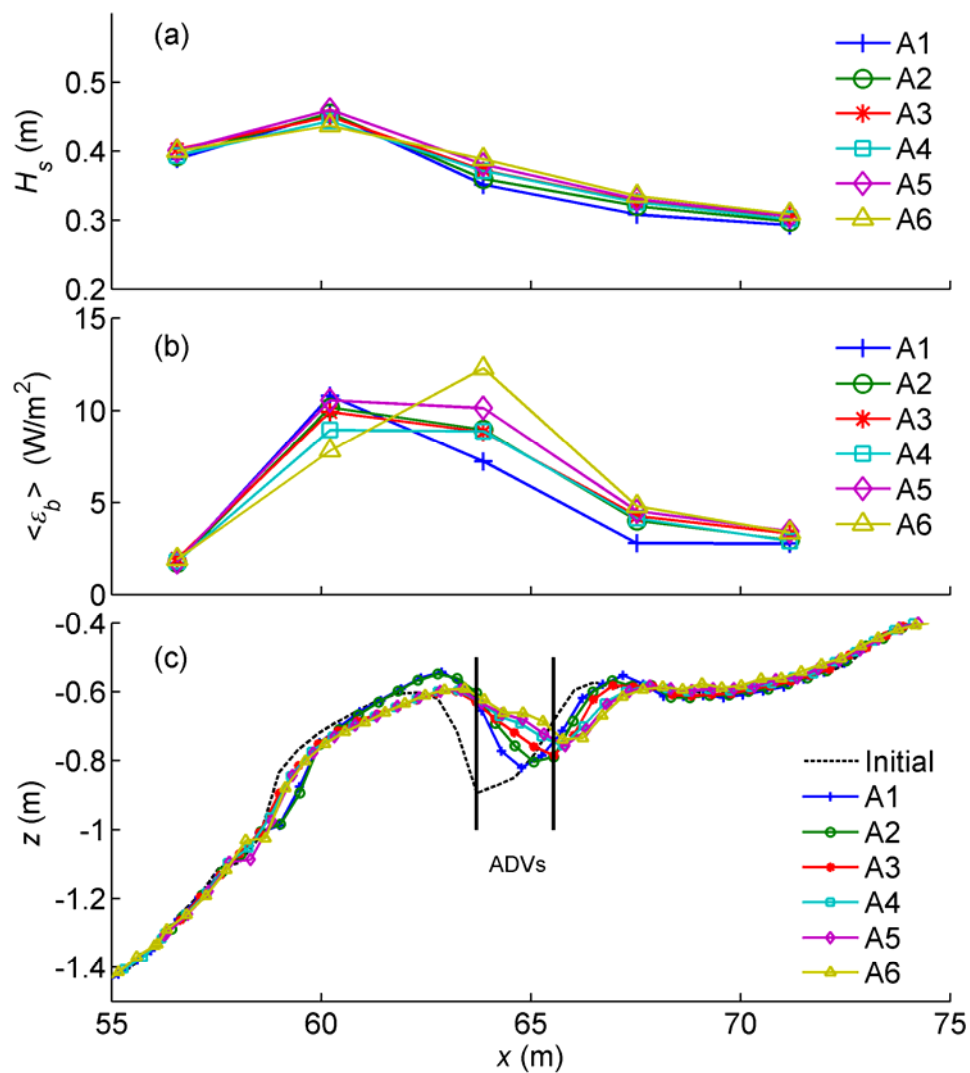


Figure 2.6: Cross-shore distributions of (a) significant wave height (H_s), (b) average rate of energy dissipation by bores $\langle \varepsilon_b \rangle$, and (c) bottom profiles averaged across the wave flume for accretive case. Runs are selected when ADVs are located at the bar crest ($x_{ADV} = 63.70$ m) or at bar trough ($x_{ADV} = 65.54$ m). In panel (c), initial bathymetry is indicated by dashed line and cross-shore location of ADVs is shown as a vertical line.

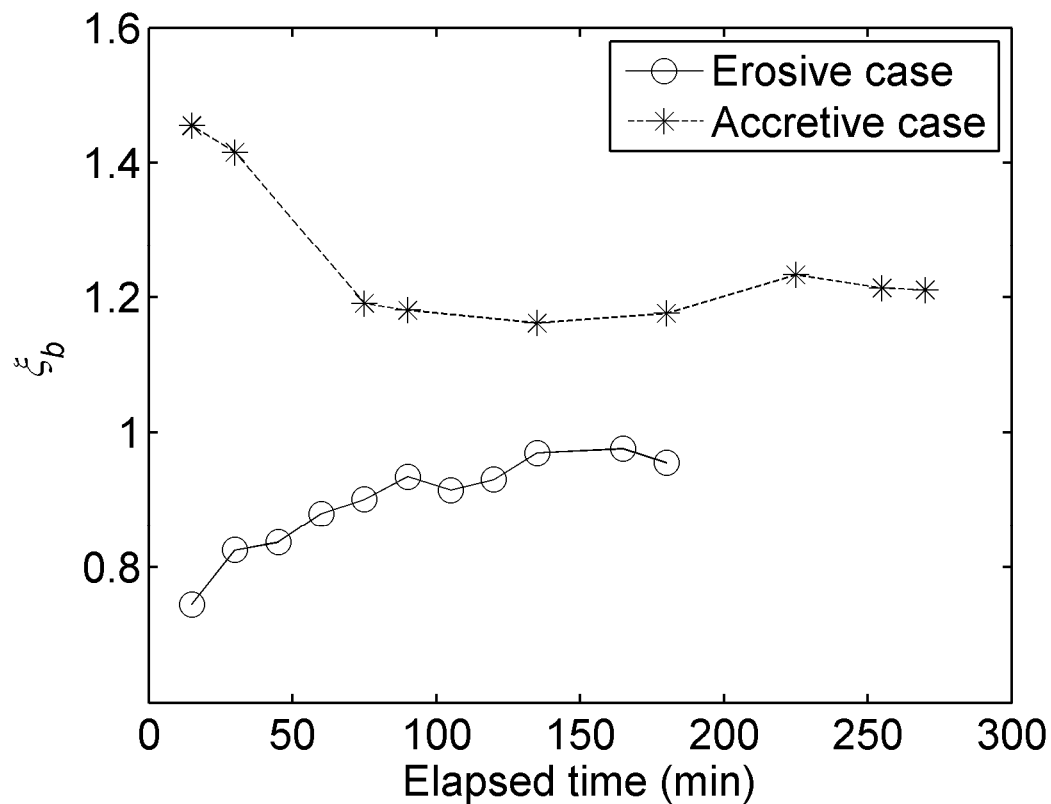


Figure 2.7: Time variation of the surf similarity parameter. Since bottom profiles for A8 and A9 were not measured, the bathymetry of A7 was used for the calculations of the surf similarity parameter for A8 ($t_{elapsed}=255$ min) and A9 ($t_{elapsed}=270$ min).

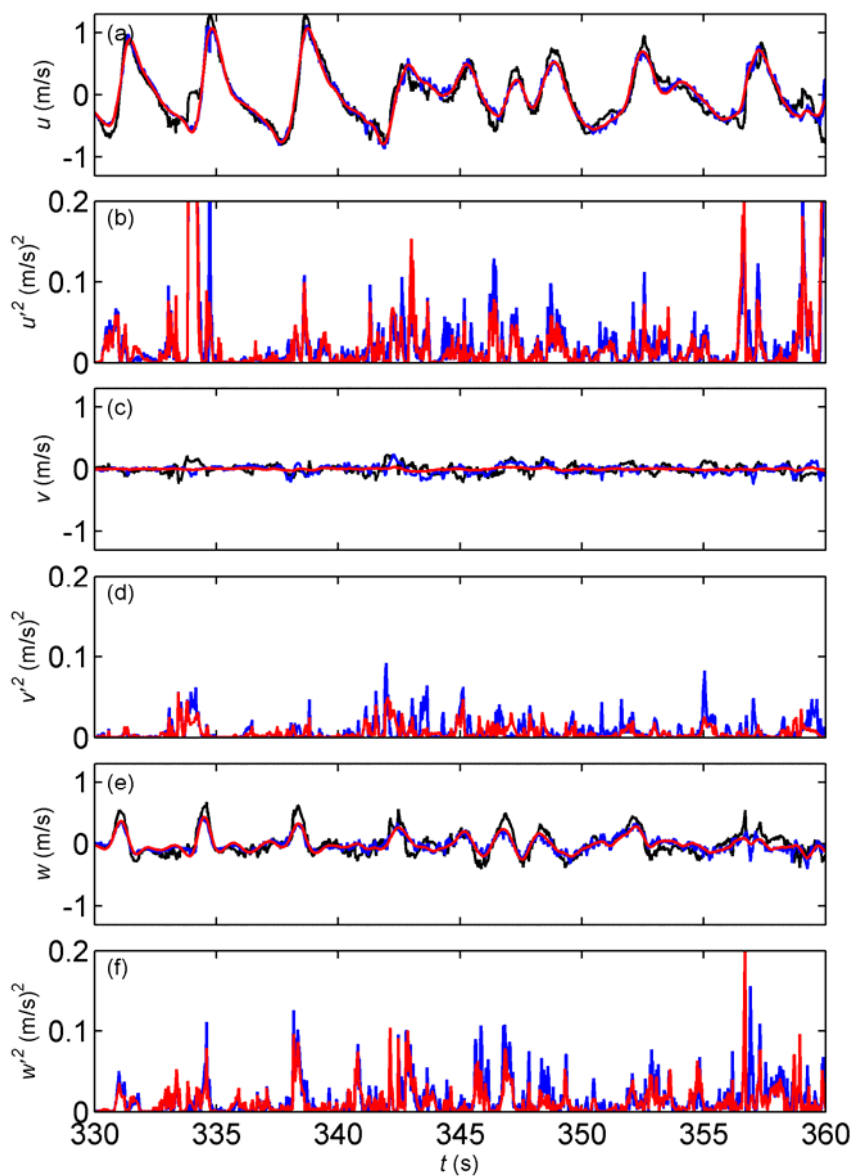


Figure 2.8: Temporal variation of (a) u at $\zeta = 0.50$ m (black line), u at $\zeta = 0.31$ m (blue line), and coherent wave motion of u (red line); (b) u^2 from ST01 (red line) and from T98 (blue line); (c) v at $\zeta = 0.50$ m (black line), v at $\zeta = 0.31$ m (blue line), and coherent wave motion of v (red line); (d) v^2 from ST01 (red line) and from T98 (blue line); (e) w at $\zeta = 0.50$ m (black line), w at $\zeta = 0.31$ m (blue line), and coherent wave motion of w (red line); and (f) w^2 from ST01 (red line) and from T98 (blue line), for E1.

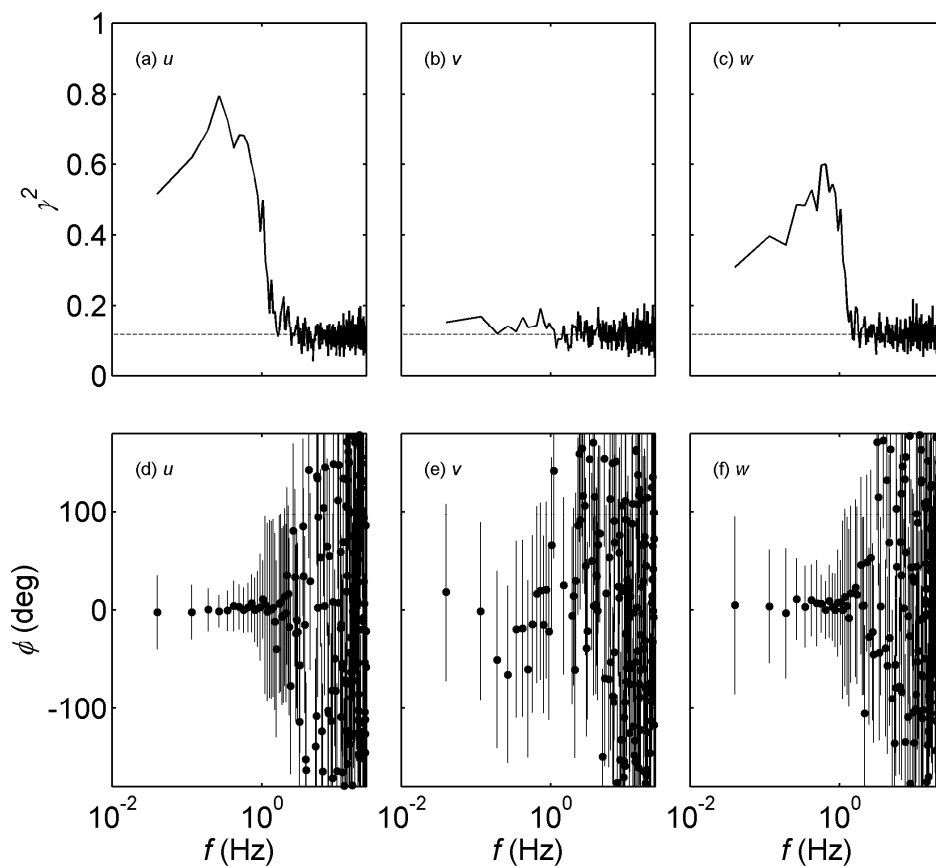


Figure 2.9: Squared coherence (γ^2) (in upper panels) and phase difference (ϕ) (in lower panels) of ADV6 and ADV5 for E1, smoothed using band averaging with 50 degrees of freedom: (a, d) cross-shore velocity; (b, e) alongshore velocity; and (c, f) vertical velocity. Dashed lines in upper panels are 95% confidence level. In lower panels, dots indicate the phase difference at frequencies where squared coherences are above 95% confidence level and vertical lines indicate 95% confidence intervals for these phase differences.

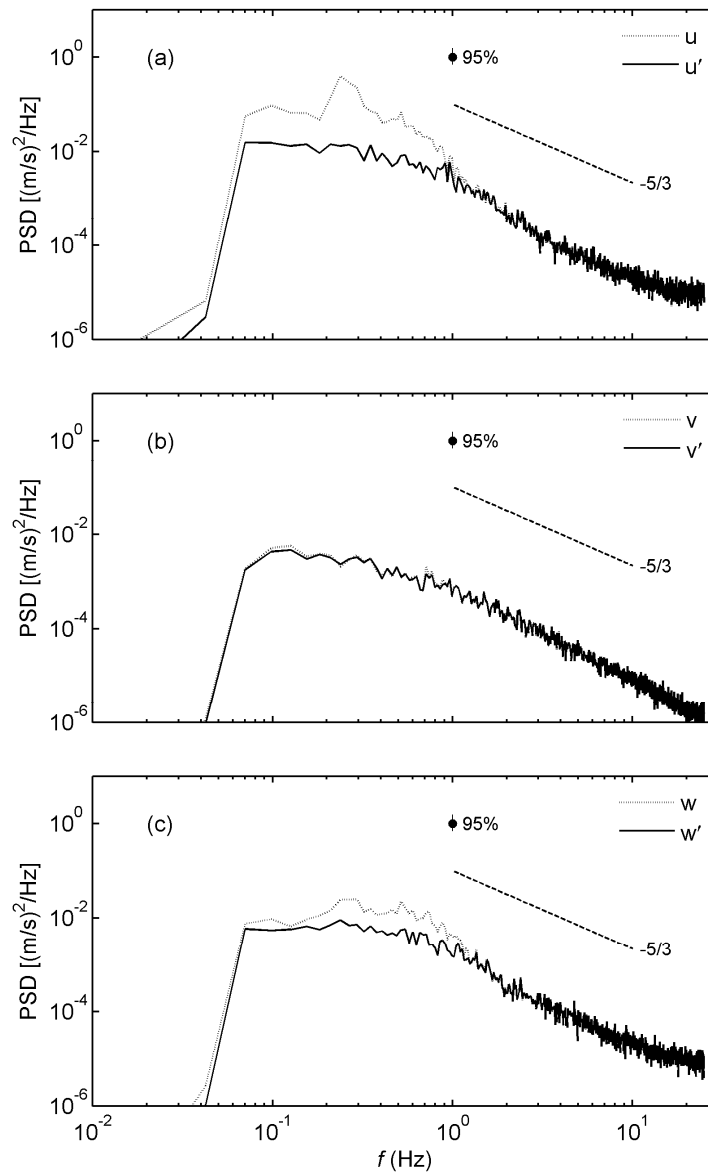


Figure 2.10: Power spectral densities (PSD) of instantaneous velocity (dotted lines) and turbulence velocity (solid lines) at ADV6 for E1: (a) cross-shore; (b) alongshore; and (c) vertical component. Turbulent velocity is estimated with ADV5 and ADV6. Despiked and interpolated velocities described in section 5.1 are used and high-pass-filtered with cut-off frequency of 0.0625 Hz. PSD is smoothed using band averaging with 50 degrees of freedom. The Kolmogorov's $-5/3$ slope is indicated as reference of turbulent inertial subrange. Vertical lines indicate 95% confidence intervals. The filter length is chosen as a half of significant wave period as suggested by Shaw and Trowbridge (2001).

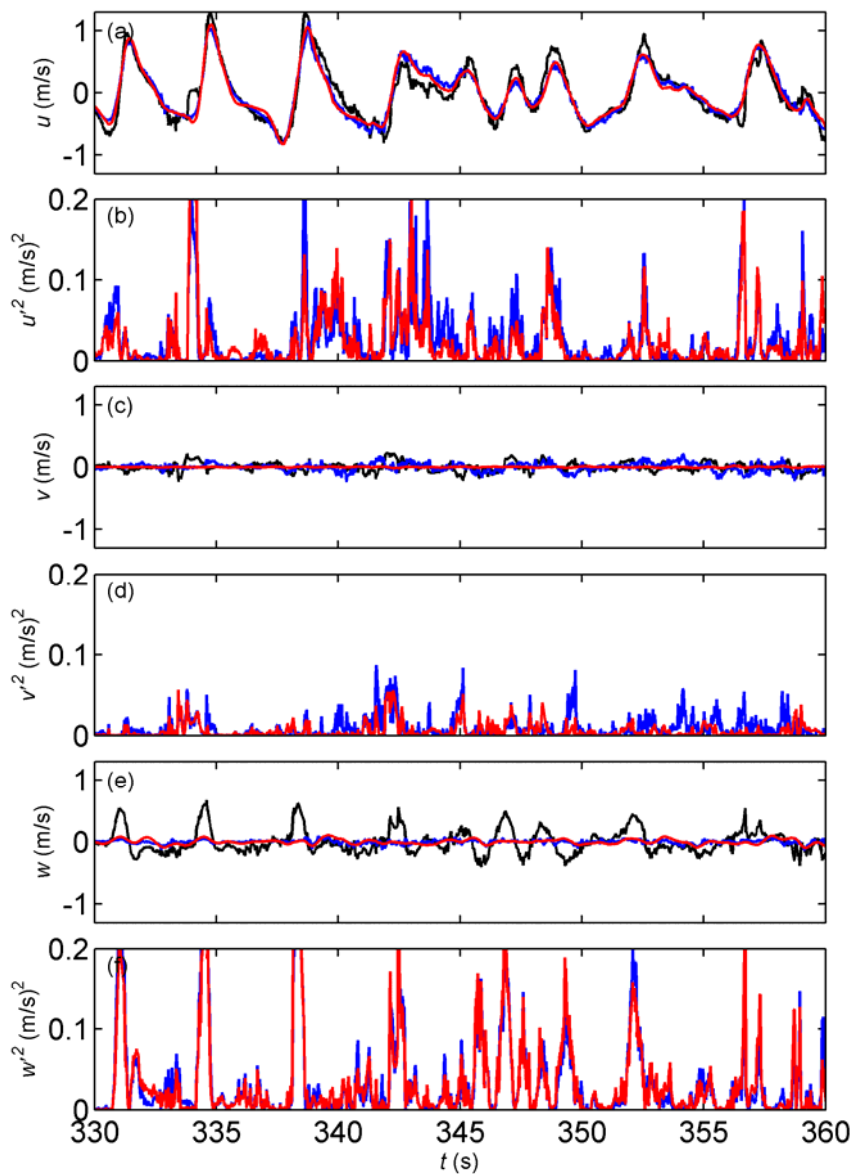


Figure 2.11: Temporal variation of (a) u at $\zeta = 0.50$ m (black line), u at $\zeta = 0.01$ m (blue line), and coherent wave motion of u (red line); (b) u^2 from ST01 (red line) and from T98 (blue line); (c) v at $\zeta = 0.50$ m (black line), v at $\zeta = 0.01$ m (blue line), and coherent wave motion of v (red line); (d) v^2 from ST01 (red line) and from T98 (blue line); (e) w at $\zeta = 0.50$ m (black line), w at $\zeta = 0.01$ m (blue line), and coherent wave motion of w (red line); and (f) w^2 from ST01 (red line) and from T98 (blue line), for E1.

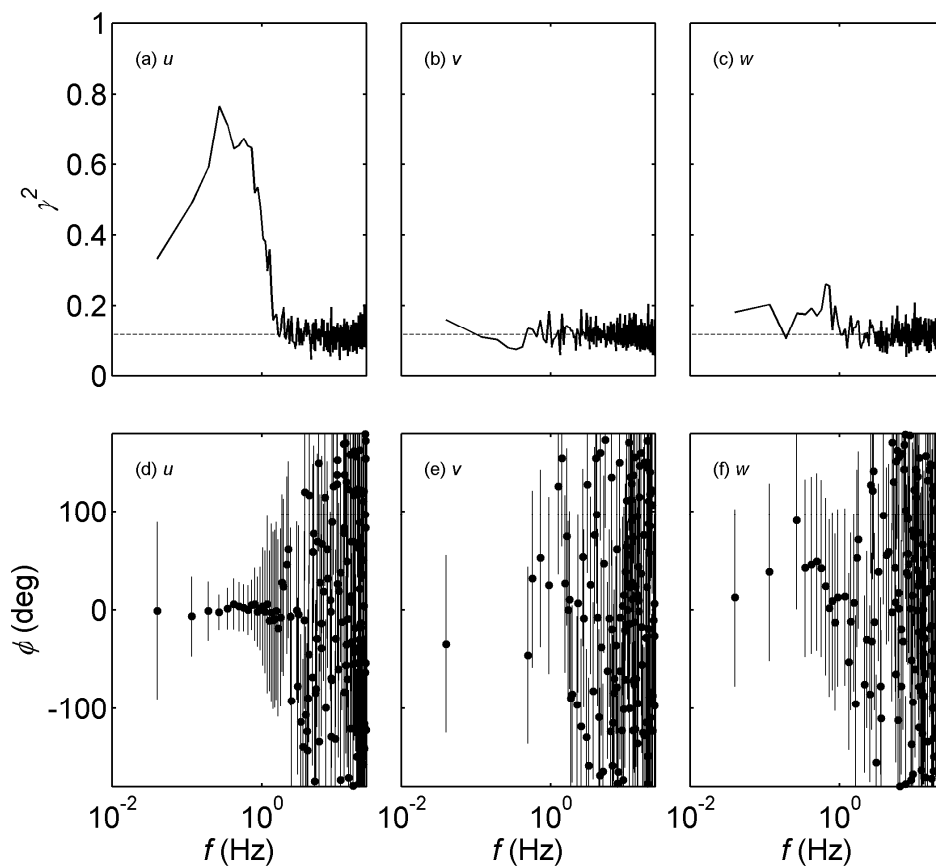


Figure 2.12: Squared coherence (γ^2) (in upper panels) and phase difference (ϕ) (in lower panels) of ADV6 and ADV1 for E1, smoothed using band averaging with 50 degrees of freedom: (a, d) cross-shore velocity; (b, e) alongshore velocity; and (c, f) vertical velocity. Dashed lines in upper panels are 95% confidence level. In lower panels, dots indicate the phase difference at frequencies where squared coherences are above 95% confidence level and vertical lines indicate 95% confidence intervals for these phase differences.

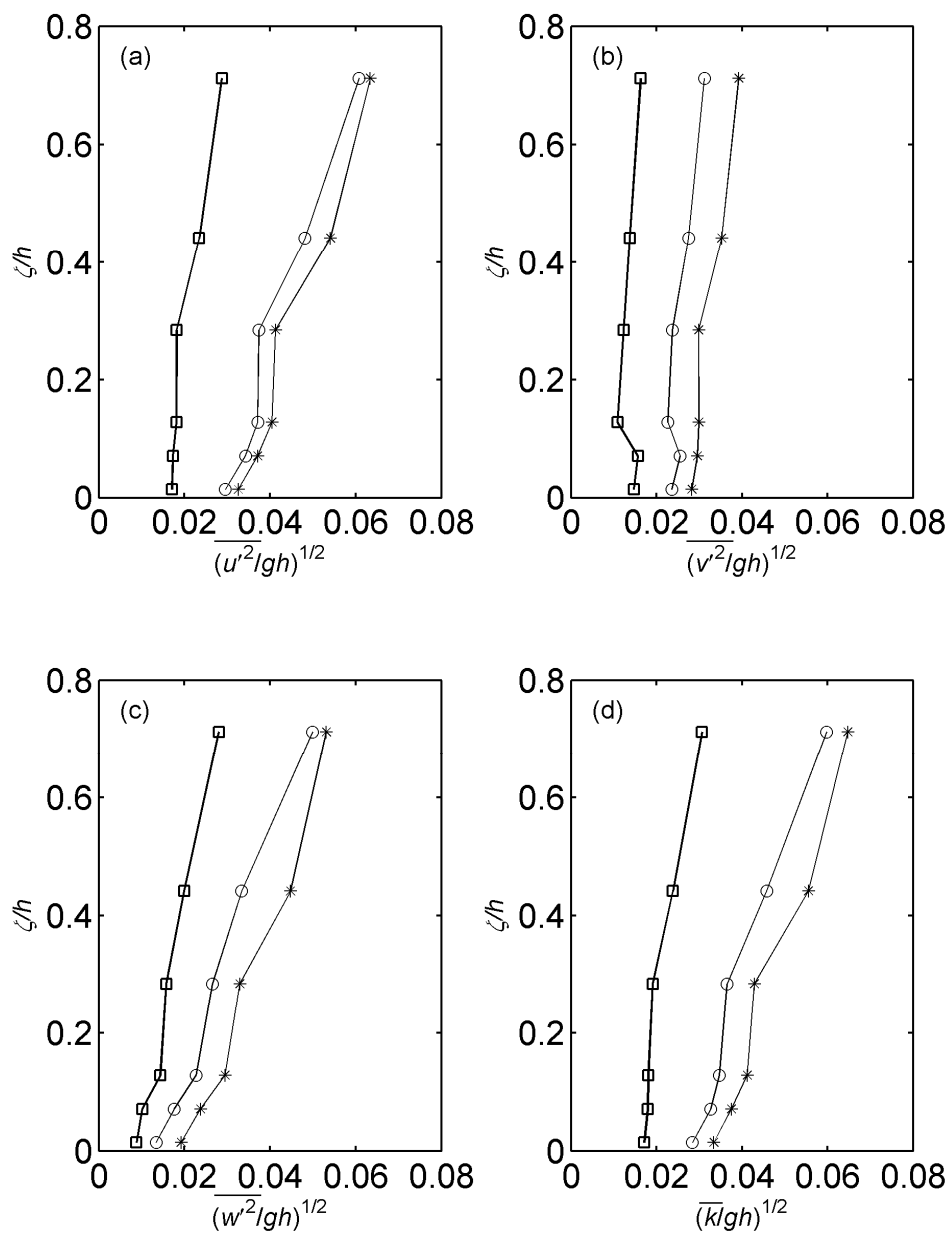


Figure 2.13: Vertical distributions of Froude-scaled turbulence intensities for E1: (a) $\overline{u'^2 / gh}^{1/2}$, (b) $\overline{v'^2 / gh}^{1/2}$, (c) $\overline{w'^2 / gh}^{1/2}$, and (d) $\overline{k / gh}^{1/2}$. Square, circle, and asterisk indicate high-pass filter (cut-off frequency: 1 Hz), ST01 method, and T98 method, respectively.

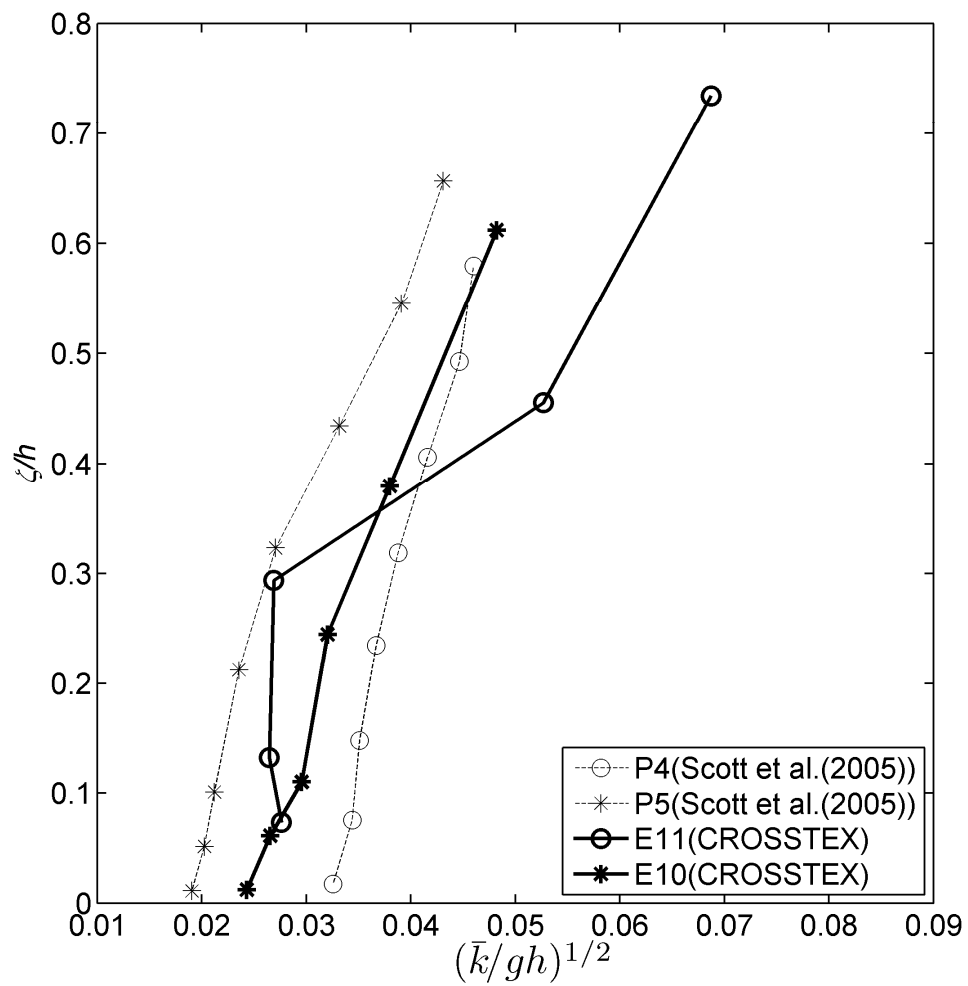


Figure 2.14: Comparison of $(\bar{k} / gh)^{1/2}$ between Scott et al., (2005) and the present study (CROSSTEX). P4(Scott et al., (2005)) and E11(CROSSTEX) are measured at the bar crest and P5(Scott et al., (2005)) and E10(CROSSTEX) are measured at the bar trough.

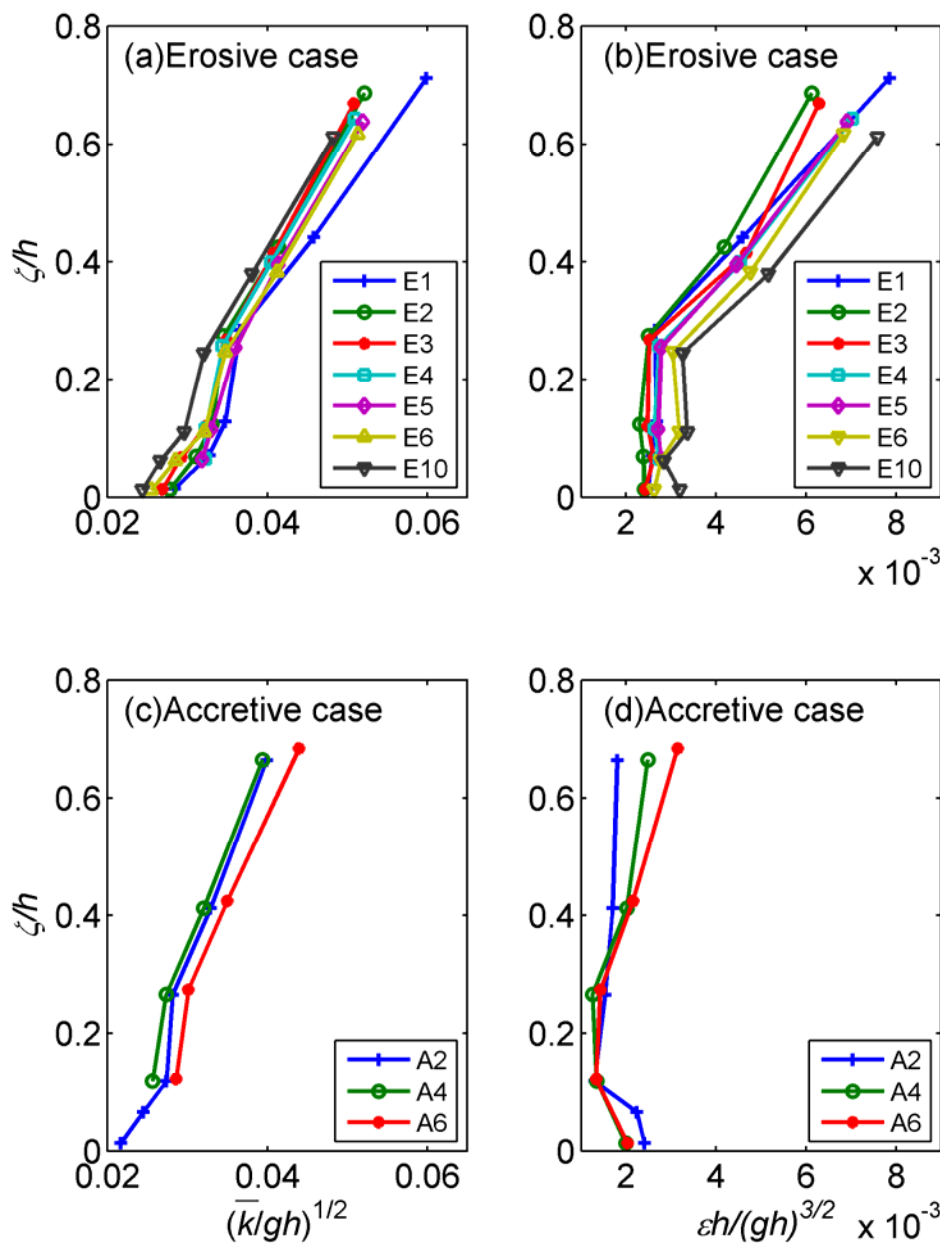


Figure 2.15: Vertical distributions of $(\bar{k} / gh)^{1/2}$ at bar trough for (a) erosive case ($x_{ADV} = 63.70$ m) and (b) accretive case ($x_{ADV} = 65.54$ m).

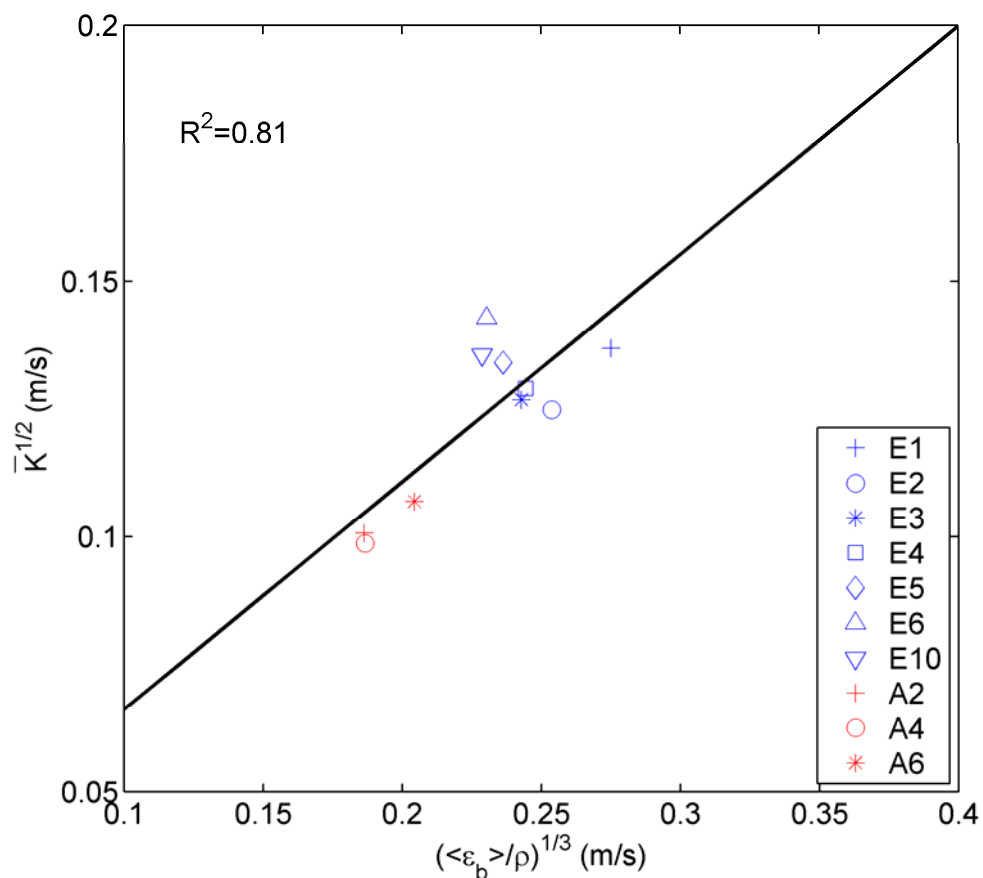


Figure 2.16: Relation between depth-averaged \bar{k} ($x_{ADV}=63.70$ m for erosive case; $x_{ADV}=65.54$ m for accretive case) and average rate of energy dissipation by bores $\langle \varepsilon_b \rangle$. $\langle \varepsilon_b \rangle$ for erosive case is measured at $x_{WG}=63.87$ m. $\langle \varepsilon_b \rangle$ for accretive case is averaged with the calculations at $x_{WG}=63.87$ m and 67.53 m.

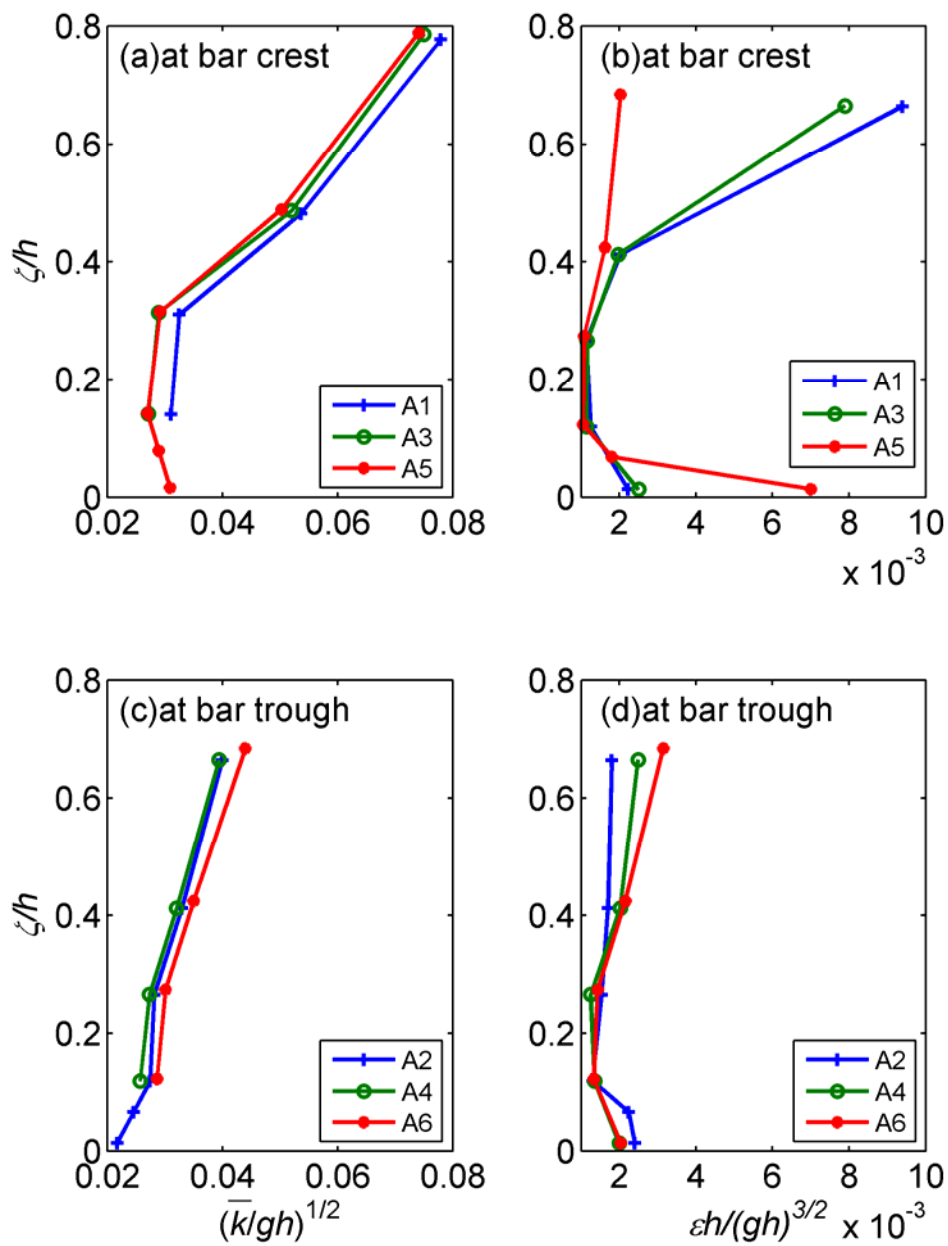


Figure 2.17: Vertical distribution of $(\bar{k}/gh)^{1/2}$ for accretive case at bar crest (A1, A3, A5; $x_{ADV}=63.70$ m; solid line) and at bar trough (A2, A4, A6; $x_{ADV}=65.54$ m; no line).

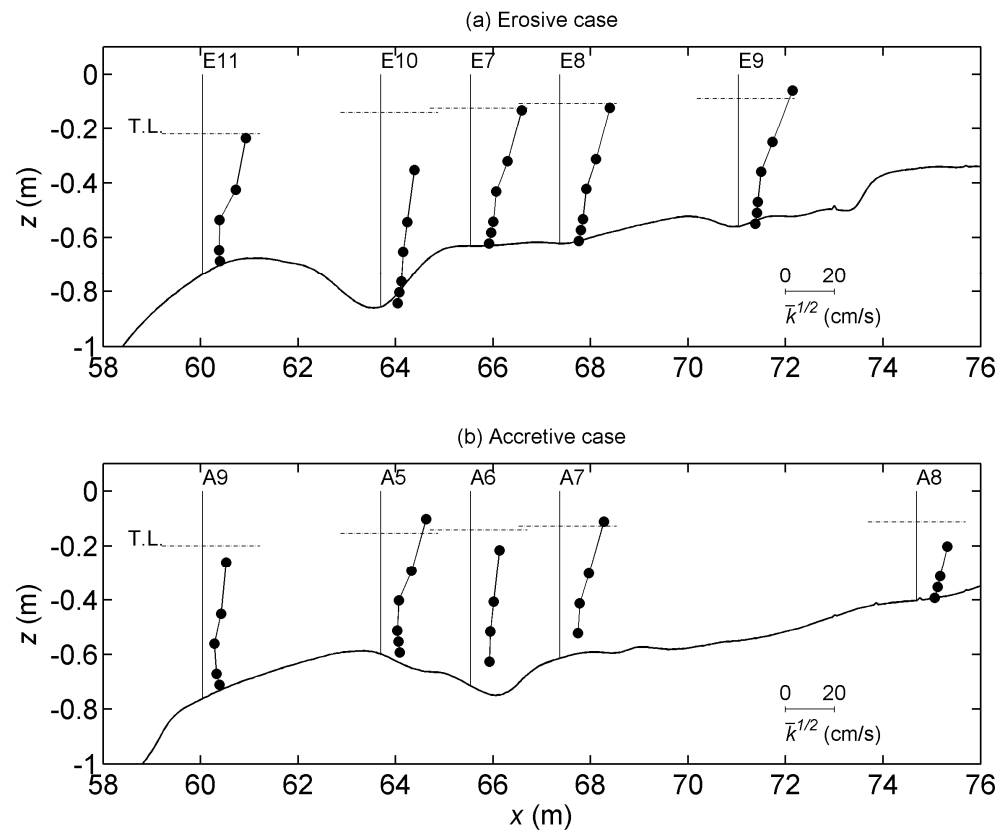


Figure 2.18: Cross-shore and vertical distributions of $\overline{k}^{1/2}$ during quasi-equilibrium state: (a) erosive case (E7-E11) and (b) accretive case (A5-A9). Bottom profiles are averaged during quasi-equilibrium state. Dashed line indicates wave trough level calculated as average of 1/3 lowest wave trough levels from zero-upcrossing.

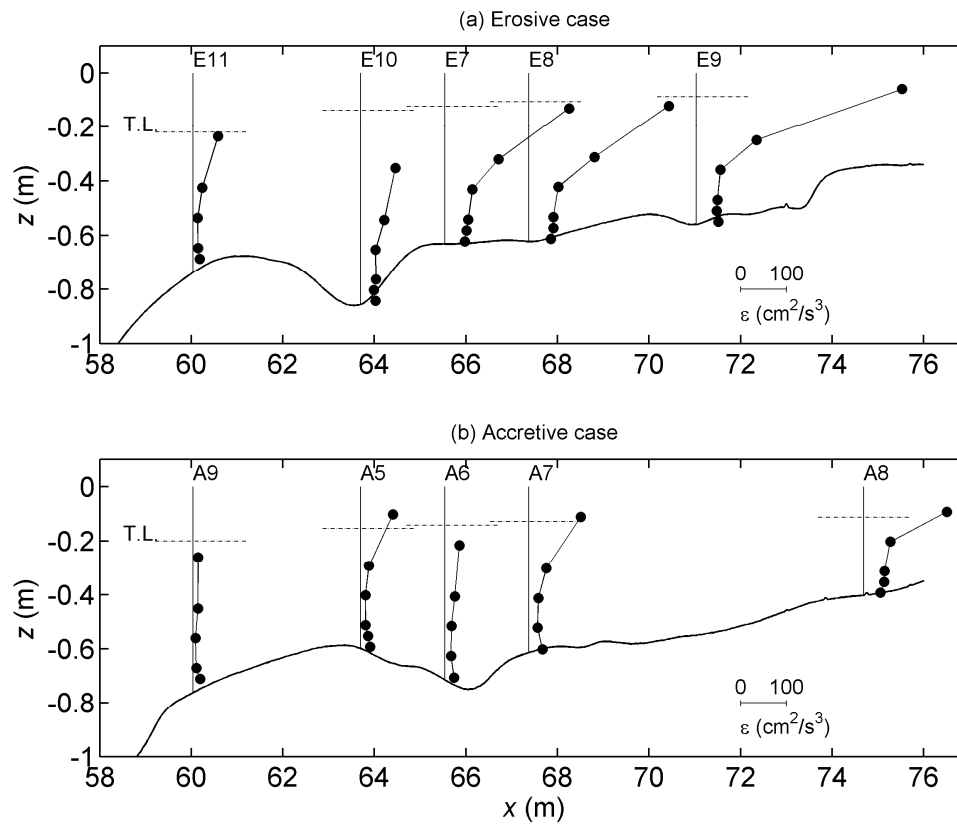


Figure 2.19: Cross-shore and vertical distributions of ε during quasi-equilibrium state: (a) erosive case (E7-E11) and (b) accretive case (A5-A9). Bottom profiles are averaged during quasi-equilibrium state. Dashed line indicates wave trough level calculated as average of 1/3 lowest wave trough levels from zero-upcrossing.

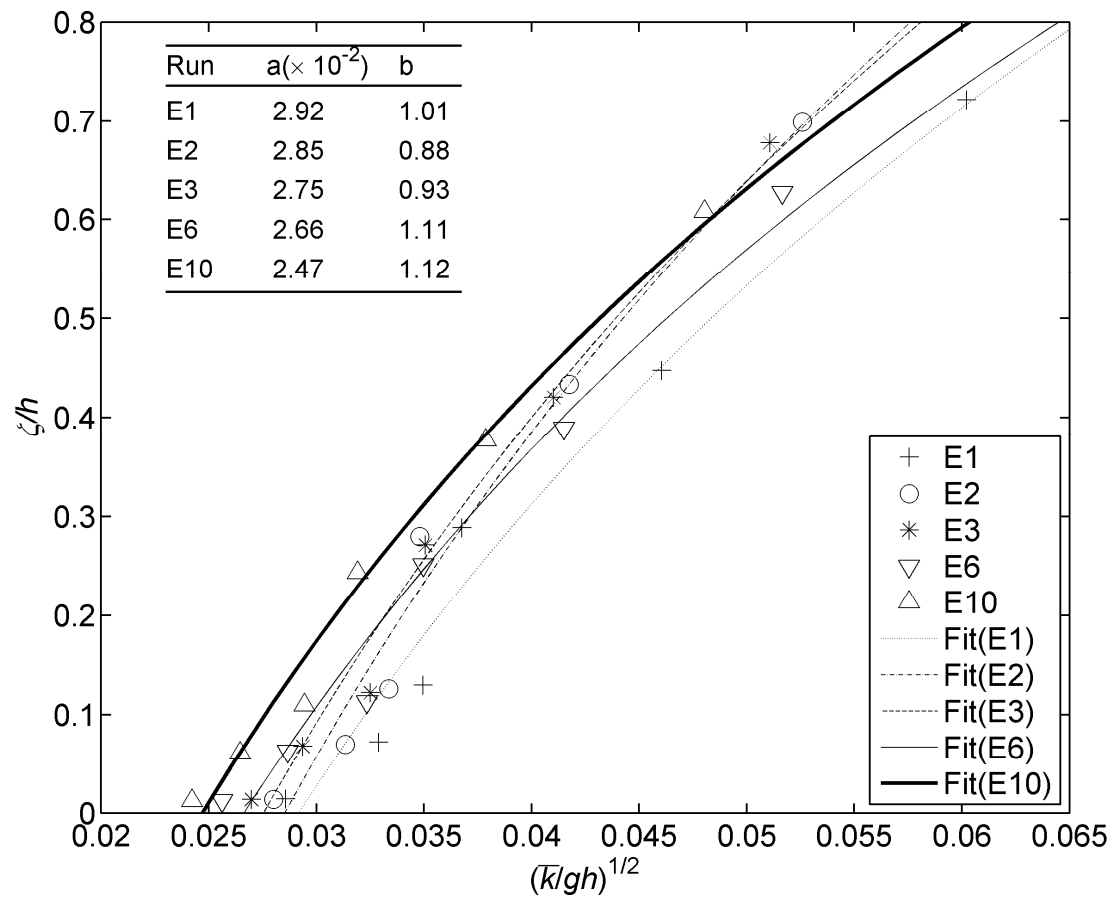


Figure 2.20. Exponential curve fitting of $(\bar{k} / gh)^{1/2}$ for erosive case at bar trough. Fitting coefficients are given in the top left corner.

Table 2.1: Summary of experimental conditions and observations during CROSSTEX

Run	Target					Observed at breaking		Observed at ADV array			
	$(H_s)_t$ (m)	$(T_p)_t$ (s)	γ_{peak} (-)	t_{dur} (min)	$t_{elapsed}$ (min)	H_b (cm)	T_p (s)	x_{ADV} (m)	H_s (cm)	h (cm)	N_b (-)
E1	0.6	4.0	3.3	15	15	51.77	4.01	63.70	43.72	70.20	102
E2	0.6	4.0	3.3	15	30	52.52	4.02	63.70	42.64	72.86	101
E3	0.6	4.0	3.3	15	45	53.80	4.01	63.70	42.21	74.72	100
E4	0.6	4.0	3.3	15	60	53.80	3.99	63.70	41.94	77.71	103
E5	0.6	4.0	3.3	15	75	54.64	3.97	63.70	41.92	78.39	118
E6	0.6	4.0	3.3	15	90	54.66	3.97	63.70	41.66	80.99	109
E7	0.6	4.0	3.3	15	105	57.75	4.00	65.54	36.72	62.38	131
E8	0.6	4.0	3.3	15	120	59.06	4.00	67.37	32.16	61.19	121
E9	0.6	4.0	3.3	15	135	58.43	4.00	71.03	27.65	55.64	160
N/A	0.6	4.0	3.3	15	150	N/A	N/A	N/A	N/A	N/A	N/A
E10	0.6	4.0	3.3	15	165	53.75	4.00	63.70	41.65	81.68	116
E11	0.6	4.0	3.3	15	180	54.50	3.99	60.04	54.50	68.07	12
A1	0.4	7.0	10.0	15	15	45.45	7.28	63.70	35.15	64.35	40
A2	0.4	7.0	10.0	15	30	45.49	7.24	65.54	34.02	75.27	55
A3	0.4	7.0	10.0	45	75	45.03	7.27	63.70	37.23	63.63	27
A4	0.4	7.0	10.0	15	90	44.35	7.23	65.54	34.86	75.15	55
A5	0.4	7.0	10.0	45	135	46.02	7.25	63.70	38.08	63.40	30
A6	0.4	7.0	10.0	45	180	43.68	7.24	65.54	36.17	73.08	61
A7	0.4	7.0	10.0	45	225	43.58	7.23	67.37	33.62	60.74	73
N/A	0.4	7.0	10.0	15	240	N/A	N/A	N/A	N/A	N/A	N/A
A8	0.4	7.0	10.0	15	255	44.99	7.23	74.69	30.20	53.63	101
A9	0.4	7.0	10.0	15	270	45.18	7.27	60.04	45.18	73.79	0
N/A	0.4	7.0	10.0	30	300	N/A	N/A	N/A	N/A	N/A	N/A

Note: N/A denotes that data were not acquired in this run. Duration is included because it contributed to total elapsed time and corresponding beach profile change.

Table 2.2: Anisotropy characteristics inside surf zone

ζ (m)	Erosive case														
	E11			E10			E7			E8			E9		
	$\overline{u'^2}$	$\overline{v'^2}$	$\overline{w'^2}$												
0.50	0.64	0.05	0.31	0.47	0.22	0.31	0.50	0.12	0.38	0.52	0.13	0.35	0.50	0.12	0.37
0.31	0.75	0.07	0.18	0.50	0.23	0.27	0.59	0.17	0.25	0.53	0.20	0.27	0.56	0.18	0.26
0.20	0.50	0.20	0.30	0.50	0.25	0.25	0.45	0.25	0.30	0.44	0.27	0.29	0.46	0.26	0.28
0.09	0.50	0.23	0.27	0.51	0.24	0.26	0.49	0.25	0.26	0.48	0.25	0.27	0.48	0.25	0.27
0.05	0.60	0.24	0.16	0.53	0.32	0.15	0.48	0.34	0.17	0.49	0.34	0.17	0.51	0.33	0.16
0.01	NaN	NaN	NaN	0.50	0.40	0.10	0.49	0.41	0.10	0.47	0.41	0.11	0.55	0.35	0.11
ζ (m)	Accretive case														
	A9			A5			A6			A7			A8		
	$\overline{u'^2}$	$\overline{v'^2}$	$\overline{w'^2}$												
0.50	0.71	0.07	0.22	0.59	0.05	0.36	0.48	0.18	0.34	0.52	0.10	0.38	NaN	NaN	NaN
0.31	0.77	0.07	0.16	0.73	0.07	0.20	0.50	0.20	0.30	0.61	0.16	0.23	0.53	0.15	0.32
0.20	0.62	0.14	0.24	0.51	0.19	0.30	0.50	0.21	0.29	0.47	0.27	0.27	0.58	0.19	0.23
0.09	0.67	0.12	0.22	0.56	0.20	0.24	0.56	0.25	0.19	0.48	0.28	0.24	0.49	0.25	0.26
0.05	0.73	0.20	0.06	0.61	0.26	0.13	NaN	NaN	NaN	NaN	NaN	NaN	0.52	0.32	0.16
0.01	NaN	NaN	NaN	0.65	0.27	0.08	NaN	NaN	NaN	NaN	NaN	NaN	0.52	0.37	0.11

Chapter 3

Cross-shore variation of intermittent sediment suspension and turbulence induced by depth-limited wave breaking

Hyun-Doug Yoon

School of Civil and Construction Engineering

Oregon State University, Corvallis, OR 97331-2302, USA

Tel: 541-737-6967 Fax: 541-737-6974 Email: yoonyh@onid.orst.edu

Daniel T. Cox

School of Civil and Construction Engineering

Oregon State University, Corvallis, OR 97331-2302, USA

Submitted to

Continental Shelf Research

Abstract

Intermittent features of turbulence and sediment suspension were investigated in a large-scale laboratory flume, under erosive and accretive conditions with measured free surface elevation, fluid velocity, and sediment concentration across the surf zone. Intermittent events of turbulence and sediment suspension occurred for a small portion of the time series but contained a significant amount of motions in these events. Comparison of intermittency statistics with previous studies conducted under different experimental conditions showed similar results, indicating that intermittency is a general aspect of turbulence and sediment suspension in the surf zone, including the bar crest, the bar trough, and the inner surf zone. The relationship of these intermittent turbulence and suspension events were examined with conditional probabilities. Here, it was found that only 20~35% of the turbulent events were associated with sediment suspension events, implying that much of the intermittent turbulent motion may act to dissipate wave energy rather than suspend sediments. On the other hand, 50~65% of the sediment suspension events were associated with turbulent events, implying that intermittent turbulent motion is one of the fundamental mechanism for the initiation of sediment suspension in the surf zone. The sediment suspension events that were uncorrelated with turbulent events were mostly induced by strong offshore low-frequency motion, suggesting that advection plays a key role. One notable exception was at the bar trough in the accretive case. Here, additional mechanisms for the initiation of sediment suspension such as strong pressure gradients are

particularly important for this case. The vertical structures of intermittency showed that the duration of intermittent events for both turbulence and sediment concentration were vertically uniform and quantitatively similar each other, although their thresholds varied vertically. The motion contained in the intermittent suspension events increased toward the bed, while it was vertically uniform in the intermittent turbulent events. Finally, it was found that the intermittent sediment suspension events contributed to onshore sediment transport, consistent with previous field observations.

Keywords: sediment transport, intermittency, turbulence, sediment suspension, wave breaking, large-scale experiment, nearshore processes

3. 1 Introduction

Field studies have shown that the sediment suspension in the surf zone is characterized by intense, intermittent events (Hanes and Huntley, 1986; Beach and Sternberg, 1988; Jaffe and Sallenger, 1992, hereinafter JS92; Yu et al., 1993; Foster et al., 1994; Aagaard and Hughes. 2010). However, the intermittent feature of sediment suspension and transport can be lost by traditional statistical processes, such as time-averaging, even though the intermittency may be critical to understanding cross-shore sediment transport. For instance, the importance of the intermittent suspension to sediment transport was pointed out by showing the significance of the coupled fluctuations of velocity and sediment concentration in

the calculation of sediment flux (Jaffe et al., 1984; Ogston and Sternberg, 1995). JS92 quantified the contribution of intermittent suspension events on the cross-shore sediment transport using the field data at Duck, North Carolina. They showed that the ‘large’ suspension events, which exceed the mean plus three standard deviations of the time series, accounted for only 10% of the total record duration, but these events contains approximately 15~35% of the sediment concentration and drove the onshore sediment transport.

Independent of sediment suspension, the instantaneous velocity signal due to wave breaking is also intermittent, and contains large and coherent motions that are several orders of magnitude larger than the average turbulence levels. Cox and Kobayashi (2000), hereinafter CK00, identified intermittent coherent events (which exceed the mean plus one standard deviation) in the surf zone and these events occurred for only 10% of the record yet they contained approximately 50% of turbulent kinetic energy in spilling breakers. Cox and Anderson (2001) confirmed the existence of intermittency in plunging breakers, showing similar statistics of 7% of the record and 40% of turbulent kinetic energy for the coherent event. Furthermore, in a natural surf zone, Ruessink (2010) applied kurtosis for estimating the intermittent events of Reynolds stress, and showed that only 3~15% of the duration contributed to the net stress. These studies highlighted the importance of the intense, intermittent turbulence to describe the turbulent flow field in the surf zone.

Although research on the intermittency of sediment suspension and turbulence has been conducted independently, the relationship between these first-order surf zone processes is still unclear. Based on small-scale laboratory investigations, it was visually demonstrated that sediment suspension in the surf zone is governed by large-scale obliquely descending eddies (Nadaoka et al., 1989) or downbursts (Kubo and Sunamura, 2001) which hit the bottom and lift the sediment into suspension. However, the inherent limitation of small-scale laboratory flume prohibits the quantification of the contribution of turbulence in the sediment suspension and transport. Scott et al. (2009) examined the relation between steep wave, turbulence, and sediment concentration, applying wavelet analysis to some part of the data in the present paper. However, since their statistical results were limited to only one cross-shore location and two elevations (1 and 9 cm above the bed), more data at other cross-shore locations and elevations are needed to understand the intermittent features of turbulence and sediment concentration. Aagaard and Hughes (2010) examined the role of coherent vortices (related to wave breaking) in suspension sediment dynamics from the field measurements, and they showed that plunging breakers induced larger sediment suspension than surf bores and shoaling waves. In their estimation of Reynolds stress near the bed, they used the vertical velocity component as proxy for the turbulence. However, this may be insufficient to describe the intense, intermittent turbulent flow field near the bed because the vertical component will be influenced by the bottom.

On the other hand, there have been efforts to incorporate the influence of turbulence on the cross-shore sediment transport. Roelvink and Stive (1989) examined the contributions of breaking-induced turbulence, low-frequency motions (i.e., undertow, long-waves), and incident waves asymmetry to bar-generating cross-shore flow mechanisms on a beach. They found that all contributing factors were the same order of magnitude. Butt et al. (2004) investigated the role of turbulence for sediment transport in the swash and inner surf zone, and they improved the predictive capability of Bagnold-type sediment transport model, replacing the bed shear stress term with turbulent kinetic energy. However, these models are based on the time-averaged turbulent kinetic energy, without considering the intermittency of turbulence which could be important for sediment transport modeling.

In this paper, we use observations from a large-scale laboratory flume to investigate the relationship between intermittent turbulence by wave breaking and intermittent sediment suspension. We conducted the study using both erosive and accretive conditions, and our observations were made at several cross-shore locations, including the bar crest, bar trough, and inner surf zone. We examine the relationship between the intermittent turbulence and sediment suspension events using conditional probability, that is, the probability that turbulence-induced sediment suspension event will be observed on the condition of each sediment

suspension or turbulence event. By doing so, we explore the contribution of wave breaking turbulence on sediment suspension and subsequent transport process for the erosive and accretive beach cases.

This paper is organized as follows. In Section 2, we describe the experiment and the data used for the analysis. In Section 3, we briefly explain the data reduction, including methodology for identifying intermittent events. In Section 4, we provide the results of the intermittent events. In Subsection 4.1, we investigate the intermittent features of turbulence and sediment suspension near the bed. In addition, the relationship between them is examined with a probabilistic approach. In Subsection 4.2, we extend the intermittency analysis through the water column. The cross-shore and vertical distribution of the intermittent turbulence and sediment concentration will be shown. In Subsection 4.3, we estimate the contribution of the intermittency to the cross-shore sediment flux. In Section 5, we discuss possible mechanisms of the sediment suspension in addition to turbulence. Also we discuss the importance of intermittency in future modeling of nearshore processes. Finally, in Section 6 we summarize the findings and present our conclusions.

3. 2 Experiment

The experiment was conducted in the large wave flume (104 m long, 3.7 m wide, and 4.6 m deep) at Oregon State University's O H Hinsdale Wave Research

Laboratory during the summer of 2005, as a part of CROSSTEX (CROSS-Shore Sediment Transport EXperiment). Approximately 800 m³ of Oregon beach sand ($d_{50}=0.22$ mm) were placed for a natural beach. For the experiment presented here, two wave conditions were synthesized to produce erosive and accretive conditions. For the erosive conditions, the vertical instrument array was held fixed while the bathymetry transformed from essentially a planar beach to a barred beach (Fig 1a). For each run (E1 to E6), the same irregular wave time series was used as the command signal for the wavemaker with a 15 minute duration. Then, with the forcing conditions essentially held constant, the beach was in quasi-equilibrium, and the instrument array was moved to five cross-shore locations (Fig 1b) for runs E7 to E11. For the accretive conditions, a new irregular wave time series was used, and the vertical instrument array was alternately stationed at two locations at the start of the surf zone as the bar migrated onshore for runs A1 to A4 (Fig 1c). Keeping the same accretive forcing, the beach reach a quasi-equilibrium condition, and the array was moved to five cross-shore locations for runs A5 to A9 (Fig 1d). Following Yoon and Cox (2010), we use the notation erosive and unstable (EU), erosive and quasi-equilibrium (EQ), accretive and unstable (AU), and accretive and quasi-equilibrium (AQ), respectively, as shown in Figure 3.1.

Table 3.1 summarizes the wave conditions observed during the experiment. The irregular waves were generated with a TMA spectrum (Bouws et al., 1985). The

observed significant wave heights at the seaward side of the bar crest (H_b) ranged from 51.8 cm to 59.1 cm for the erosive case and from 43.7 cm to 46.0 cm for the accretive case. The cross-shore location of H_b was measured at $x=60.21$ m, where x is positive onshore with $x=0$ m at the wavemaker. The significant wave height was calculated using the zeroth moment of a wave spectrum. The observed peak periods (T_p) at $x=60.21$ m ranged from 3.97 s to 4.02 s for the erosive case and from 7.23 s to 7.28 s for the accretive case.

The wave breaker types were classified with the surf similarity parameter defined as (Battjes, 1974):

$$\xi_b = \frac{\tan \alpha_b}{\sqrt{H_b / L_0}} \quad (3.1)$$

where $\tan \alpha_b$ is the bottom slope in front of the breaking point, and L_0 is the deepwater wavelength. In general, spilling breakers were observed predominant for the erosive case and plunging breakers were observed predominant for the accretive case (Yoon and Cox, 2010). However, the bar development caused a gradual transition from spilling-type to plunging type breakers as ξ_b ranged from 0.74 to 0.98 during the erosive case. On the contrary, in the accretive case, waves broke in a more spilling manner as the beach evolves, with ξ_b decreasing from 1.46 to 1.16. In addition to the observation at the seaward side of the bar crest, the observation at the instrument array are also listed in Table 3.1. The cross-shore

locations of the instrumental array (x), significant wave height (H_s), water depth (h), and the number of wave breaking (N_b) which was visually observed at the instrument array are also listed. The total elapsed times from the start are also listed in the last column. Most runs lasted 15 minutes, but some runs in the accretive case lasted 45 minutes by repeating the wavemaker command signal 3 times. The total elapsed time is 180 minutes for the erosive case and 300 minutes for the accretive case.

Figure 3.2 shows the instruments installed on a vertical array in the mobile cart. Simultaneous, high resolution measurements of velocity and sediment concentration were obtained from acoustic Doppler velocimeters (ADV) and fiber-optic backscatter sensors (FOBS). The ADV stack measured the cross-shore velocity (u), alongshore velocity (v), and vertical velocity (w) at six elevations with a sampling rate of 50 Hz. The instrument array was lowered such that the sampling volume of the bottommost ADV was 1.0 cm above the bed at the start of each run. The distances from the bed (ζ) of the ADVs were 1.0 cm (ADV1), 5.0 cm (ADV2), 9.0 cm (ADV3), 20.0 cm (ADV4), 31.0 cm (ADV5), and 50.0 cm (ADV6). FOBS were equipped in two probes which were identified as the lower and upper probe. The lower and upper probes consist of 8 and 6 FOBS, respectively. Similar to the ADV, the lowest FOBS was located 1.0 cm above the bottom at the start of each run. The distances from the bed were 1.0, 2.0, 3.0, 4.0,

5.0, 6.0, 7.0, and 9.0 cm for the lower probe and 9.0, 11.0, 14.0, 17.0, 21.0, and 32.0 cm for the upper probe. The sampling rate of FOBS was 10 Hz. Details about the experiment procedure can also be found in Yoon and Cox (2010).

3.3 Data reduction

3.3.1 Pre-process of velocity and sediment concentration data

For ADV data, a signal-to-noise ratio (SNR) threshold and the 3-d phase-space threshold method by Mori et al. (2007) were used to identify spikes. A SNR threshold of 10 dB was used first to identify spike noise, and then the 3D phase-space threshold method was used for the data which were not identified by the SNR threshold. For the identified spikes, the linear interpolation (for the spikes less than 0.26 s) or a running mean (for the spikes longer than 0.26 s) were used to replace those spikes, following Yoon and Cox (2010). For the all runs in the study, the despiked signals took 12.8% of the total record, showing decreased percentage toward the bottom where the void fraction induced by wave breaking turbulence was significantly lower.

For FOBS data, the calibration was performed using a racetrack flume. This flume was equipped with a propeller to circulate sediment and water through a cylinder along the flume centerline. The amount of 99 liters of tap water was added to the racetrack flume and known weights of sand were added to the flume. A second-

order polynomial was fit to the calibration data using the average voltage recorded for 3 minutes. Then, because FOBS signals have their own sensor specific offset voltage even at zero concentration (Fugate and Friedrichs, 2002), the output of the FOBS was adjusted by subtracting the average of the first 10 s in the time series, although the averages of the sediment concentration for the first 10 s were less than 10% of the average of the whole time series. Note that the FOBS at $x=63.7$ m detected the first considerable sediment suspension around $t=26$ s. Furthermore, the FOBS data were filtered with a median filter as recommended by Downing (2006), using a 3-point filter length.

3.3.2 Hydrodynamic forcing and sediment response

Figure 3.3 shows an example of the data for E2 which is an example from the EU case measured at bar trough. The measured instantaneous velocity (u) can be separated into

$$u = u_{lf} + u_{wave} + u' \quad (3.2)$$

where u_{lf} is the low-frequency motion including the mean component, u_{wave} is the wave-induced motion, and u' is the turbulent fluctuation. The top three panels show the low-frequency motion (u_{lf}) in Figure 3.3a, the wave-induced motion (u_{wave}) in Figure 3.3b, and turbulent fluid motion characterized by the turbulent kinetic energy (k) in Figure 3.3c. The sediment response is shown in Figure 3.3d. The following paragraphs describe each panel in detail.

Figure 3.3a shows the low-frequency motions for two ADVs, located at near bottom (ADV1, $\zeta = 0.01$ m) and at mid water column (ADV6, $\zeta = 0.50$ m). The low-frequency motion was low-pass filtered with $f / f_p < 0.25$, where f is the frequency and f_p is the peak frequency. Figure 3.3a shows that low-frequency motion is predominantly offshore and the variability of this flow is on the order of several wave periods. This seaward flow can, in some sense, be seen as a ‘slowly varying undertow’ – that is, the offshore flow increases in response to increased wave breaking, as was noted by Scott et al. (2004). In general, the near bottom and mid-depth low frequency motion is in-phase and approximately the same magnitude (e.g., $600 < t < 700$ s) although it is noted that occasionally a strong shear would develop and persist for several wave periods (e.g., $t \sim 290$ s, $t \sim 570$ s). Such ‘shear motion’ in the low frequency motion, which was observed occasionally in most of the records, cannot be explained from long wave theory (e.g., long waves forced by wave groups), and we speculate that this is a transient effect due to the return currents induced by wave breaking. The open circles are associated with the intermittent sediment suspension events as explained in Subsection 3.3.

Figure 3.3b shows an example of the wave-induced motion for ADV1 ($\zeta = 0.01$ m). ADV6 ($\zeta = 0.50$ m) is not shown for clarity and will be shown in Figure 3.4. The

wave-induced motion is estimated by applying Shaw and Trowbridge (2001) method, hereinafter ST01, on the high-pass filtered ($f / f_p > 0.25$) velocity. The basic assumption of the ST01 method is that coherent signals from a pair of ADVs are regarded as wave-induced motions but incoherent signals are turbulence. The wave-induced motion is calculated as follows.

$$u_{wave}(t)_{(1)} = \int_{-T/2}^{T/2} h_f(t-\tau) [u(t) - u_{lf}(t)]_{(2)} d\tau \quad (3.3)$$

where, $u_{wave}(t)_{(1)}$ is the time series of wave-induced motion at position (1), $[u(t) - u_{lf}(t)]_{(2)}$ is the high-pass filtered ($f / f_p > 0.25$) velocity at position (2), T is a filter length ($T_p / 2$ are used in this study), and h_f is a least square filter. Further details of a matrix form for calculation are provided in Yoon and Cox (2010). The wave-induced motion near the bed (ADV1, $\zeta = 0.01$ m) is estimated with ADV3 ($\zeta = 0.09$ m) except for some runs (E4, E5, E11, and A9) where an error in data acquisition at ADV1 occurred. In these cases, ADV1 data were replaced with ADV2. This replacement has little effect on the result of intermittency statistics as will be shown in Figure 3.5. For E2, the mean of u_{wave} is zero and the root-mean-square value is 0.32 m/s, while the mean of u_{lf} is -0.12 m/s (negative means offshore) and the root-mean-square value is 0.22 m/s, at ADV1 ($\zeta = 0.01$ m). Therefore, we note that the low frequency motion cannot be considered ‘weak’ compared to the wave-induced motions.

Figure 3.3c shows the turbulent kinetic energy per unit mass (k) which is calculated as follows:

$$k = \frac{1}{2}(u'^2 + v'^2 + w'^2) \quad (3.4)$$

where, u' , v' , and w' are turbulent components of cross-shore, alongshore, and vertical fluid velocities, respectively. Each turbulent component was estimated using the method of ST01. The solid thick line in Figure 3.3c shows a moving average using a 2 s filter length with the first 100 s of data truncated to eliminate transitional effects associated with the start of each run. The 2 s filter was used to further smooth the data to provide more robust statistics while at the same time retaining the characteristic intermittent signal.

Figure 3.3d shows the temporal variation of the suspended load (C) which is defined as follows (e.g., Butt et al., 2005; Aagaard and Hughes, 2006; Puleo, 2009):

$$C = \sum_0^{h_s} c(\zeta)\Delta\zeta \quad (3.5)$$

where, $c(\zeta)$ is the suspended sediment concentration at the elevation of ζ , $\Delta\zeta$ is the distance between measurement elevations, h_s is the elevation of top sensor, and C is the suspended load. The suspended load, C , is integrated from the bed to the height of the highest FOBS in the lower probe ($\zeta=0.09$ m), focusing on the sediment suspension near the bed and providing a less noisy signal than the

sediment concentration at a specific elevation. Similar to Figure 3.3c, the solid thick line shows the data filtered with a 2 s moving average.

3.3.3 Identifying intermittent events

In this subsection, we use a thresholding technique to identify the intermittent events following the works of JS92 for suspended sediments and CK00 for wave breaking turbulence. To summarize, an intermittent event is defined where the value of k or C exceeds a certain threshold. A ‘Coherent Event’ termed by CK00 is defined when the signal exceeds the mean plus one standard deviation. The horizontal dash lines in Figures 3.3c and 3d show an example of the threshold value of the coherent event. An ‘Intense Event’ is defined when the signal exceeds the mean plus three standard deviations. The horizontal dash lines in Figures 3.4c-3.4e show an example of the threshold value of the intense event. Consistent with CK00, the durations of the coherent and intense events are defined as n_1 / n and n_3 / n , respectively, where n_1 and n_3 are the number of data points exceeding the threshold, and n is the total number of data points. Also, the percent of the motion contained in the coherent and intense events are defined as $n_1 m_1 / nm$ and $n_3 m_3 / nm$, where m_1 and m_3 are the average values of the data points exceeding the threshold.

In Figure 3.3, the peak of each coherent event is denoted as a triangle (Figure 3.3c) or a circle (Figure 3.3d). The closed triangles and circles denote the events in which k and C are correlated within a window length of $\pm T_p / 2$ centered on the peak of the k event. The open triangles and circles denote the uncorrelated events between k and C . The open circles are re-plotted in Figure 3.3a to show the direction of the low frequency motion (offshore or onshore) during these uncorrelated sediment suspension events.

Before presenting a quantitative analysis on the intermittency of k and C for the different surf zone locations and the erosive vs. accretive case, we show a detail of the fluid motion and suspended sediment concentration to highlight the complexity of the turbulence and sediment suspension under fairly well-controlled laboratory conditions. Figure 3.4 shows a detail modified from Figure 3.3 in the range 330 s to 400 s, dropping the smoothed curves (thick lines) and adding another velocity sensor from mid-depth in Figure 3.4b. Figures 3.4a and 3.4b show the low-frequency motion and wave-induced motions, respectively, at mid-depth (ADV6, $\zeta = 0.50$ m) and near bottom (ADV1, $\zeta = 0.01$ m). Figures 3.4c and 3.4d show the turbulence at mid-depth k_u and near bottom k_l , respectively, and Figure 3.4e shows the suspended sediment concentration, C . In this figure, the most striking feature occurs $357 \text{ s} < t < 367 \text{ s}$. Figure 3.4e shows a large sediment suspension event starting at $t = 361 \text{ s}$ which corresponds to an intense turbulence event near

the bottom shown in Figure 3.4d. This intense turbulence event is preceded in time $t = 360$ s in the upper water column shown in Figure 3.4c, indicating that the suspension event is caused by a local influx of turbulence from trough level due to wave breaking. The mechanism that triggers this turbulent event is unclear.

Looking at the u_{wave} signal in Figure 3.4b, we note that the u_{wave} signals are mismatched between ADV1 ($\zeta = 0.01$ m) and ADV6 ($\zeta = 0.50$ m) compared to elsewhere in the record. Furthermore, the u_{vf} record has a change in sign of the vertical gradient around $t = 355$ s. Whether this phenomenon contributes to the initiation of oblique descending eddies (Nadaoka et al., 1989) or downbursts (Kubo and Sunamura, 2001) is uncertain, and is the subject of further investigation beyond the scope of this paper.

Further inspection of events in Figure 3.4 highlights the complex nature of the intermittent turbulence and sediment suspension. For instance, in the range of 390 s $< t < 395$ s, one can see a large turbulent event due to wave breaking in Figures 3.4c and 3.4d; however, there is no corresponding suspension event in Figure 3.4e. Furthermore, the mismatch seen earlier in u_{wave} and the sharp change in the vertical gradient of u_{vf} are also absent. Therefore, it is difficult to predict suspension events only with turbulence. For 341 s $< t < 345$ s, one can also see a large suspension event in Figure 3.4e, but the corresponding k records in Figures 3.4c and 3.4d show only a moderate level of k prior to the event. Again, this

shows the difficulty in predicting suspension events. Nevertheless, we continue to examine the k and C statistics for intermittent events independently because these are prominent features throughout the surf zone. Then, we look at their conditional probabilities, noting under what wave conditions and cross-shore locations are these events closely coupled.

3. 4 Results

3. 4. 1 Cross-shore variation of intermittent turbulence and sediment suspension near the bed

To assess the temporal variation of the intermittent events, we start by analyzing the EU record for runs E1-E6 for which the instrumentation array was held at a fixed cross-shore location at the outer surf zone where the bar was forming. We include E10 in this analysis where the instrument array was returned to its original cross-shore location in the final stages of EQ testing. Figure 3.5 shows the temporal variation of the statistics of k and C for E1-E6, and E10. The total duration of each run (900 s) were divided into nine 100 s segments for the erosive case and five 180 s segments for the accretive case, corresponding to approximately 25 waves for each segment. The first segment was eliminated due to possible transient effects associated with the start of the wavemaker, and the analysis is performed on the remaining segments. The mean of the segments is plotted as a symbol, and the standard deviation is plotted as vertical lines from the

symbol. Figures 3.5a and 5b show the mean (m_k) and standard deviation (σ_k) of k . Turbulence intensity in ADV6 ($\zeta=0.50$ m) is higher than ADV1 ($\zeta=0.01$ m) by a factor of 2-3, because turbulence is generated near the water surface due to breaking. m_k and σ_k at ADV6 also decrease slightly from E1 to E3 by approximately 30% and then remains constant for E4-E10 although the bed continues to erode. On the other hand, m_k and σ_k at ADV1 at the lower sensor are relatively constant, even during the initial evolution of the bed. Figures 3.5c and 3.5d show that mean (m_C) and the standard deviation (σ_C) of C range from 180 to 300 g/m² for m_C and from 300 to 500 g/m² for σ_C , and can be considered constant over time considering the fairly wide standard deviations.

Figures 3.5e-3.5h show the mean and standard distribution of the intermittency statistics of k for the mid-depth and near-bottom ADV and C integrated over the bottom FOBS. The statistics are plotted for each 15 minute run with slight offsets for clarity. In Figures 3.5e and 3.5f, the intermittency statistics for the coherent events are very similar between k and C , ranging around 5 to 10% for n_1/n and 45 to 50% for n_1m_1/nm . Figures 3.5g and 3.5h show the intense events. The statistics are stable for E1-E6, E10 and very similar between k and C , ranging around 2% for n_3/n and 15 to 25% for n_3m_3/nm . The general feature of the intermittency statistics is similar regardless of the threshold of the coherent ($m + \sigma$)

or intense ($m + 3\sigma$) event. Although m_k and m_c change for E1-E4, for example, the intermittency statistics are constant when a local threshold for each run is applied. This may indicate a self similar distribution. The AU case was similar in that the statistics did not vary with time, although they did vary with location (bar crest vs. bar trough) as will be explained in Table 3.2. In summary, both the erosive and accretive unsteady cases showed that the intermittent statistics were fairly constant in time for a given cross-shore location even though the bathymetry was changing considerably.

Having looked at the unsteady erosive and accretive case, we now turn our attention to the steady erosive and accretive cases using the same thresholding technique for k and C . Figure 3.6 shows the cross-shore variation of intermittency statistics for the EQ case. To focus on turbulence and sediment suspension near the bed, we only plot the estimate at ADV1 ($\zeta = 0.01$ m). Figure 3.6a shows m_k near bottom, indicating a peak ($\sim 80 \text{ cm}^2/\text{s}^2$) at E7 and E8, landward of bar trough. Figure 3.6b shows m_c near bottom, indicated that that m_c is largest ($\sim 200 \text{ g/m}^2$) at the bar trough (E10) and decays significantly onshore. Figure 3.6c shows that the ratio of the standard deviation to mean for both k and C is relatively constant ($\sigma / m \simeq 2$) across the surf zone. This is somewhat surprising given that the signatures of the cross-shore variation of the mean turbulence m_k and sediment concentration m_c near the bottom are distinctly different. This is also consistent

with CK00 for turbulence inside the bottom boundary, and gives a further indication that there may be a self-similarity in the intermittent signals, even for the case of a non-planar beach.

In Figures 3.6d and 3.6e, the statistics range around 5 to 10% for n_1 / n and 30 to 50% for $n_1 m_1 / nm$ for both k and C . This indicates that even though intermittent events occur for only a fraction of the record (n_1 / n), these events account for a significant amount of k and C throughout the surf zone ($n_1 m_1 / nm$). In Figure 3.6e, $n_1 m_1 / nm$ is relatively constant for k , and there appears to be some variation for C with a maximum at E10 over the bar trough. For the intense events, Figure 3.6f shows that the variations in n_3 / n are similar between k and C , and the values range from 1 to 2%. Figure 3.6g shows that $n_3 m_3 / nm$ ranges from 10 to 30% with a peak at E10 for C . There is a general trend of $n_3 m_3 / nm$ for k decreasing toward shoreline from the bar, with the lowest value for both k and C occurs at E9 in the inner surf zone.

Similar to Figure 3.6 for the quasi-steady erosive case (EQ), we now show the cross-shore variation of the intermittency statistics in k and C for the quasi-steady accretive case (AQ). In Figure 3.7a, there is a slight peak in m_k at the bar crest (A5) and is shifted seaward relative to the peak in the EQ case. There is a second

peak near shoreline (A8) due to a second breaking just as the waves impinge on the shoreline. In Figure 3.7b, there is a strong peak in the bar trough measured at A6, being larger than other locations by a factor of 3-5. Seaward of the bar crest, m_C is low at A9, indicating that this location is beyond the range of sediment suspension or advection. Landward of the bar trough, A7 shows a similar decrease in sediment concentration and at A8 in the inner surf zone. Similar to the EQ case, the peak in m_C does not correspond to a peak of m_k . Also similar to the EQ case, Figure 3.7c shows that the ratio of the standard deviation over the mean is similar across the surf zone A5-A8 (except for turbulence at A9 outside the surf zone) even though the cross-shore variations of m_k and m_C are different.

Compared to the EQ case, Figure 3.7d shows a greater cross-shore variation in n_1 / n , although the values are mostly in the range of 5 to 10% as is the case for the erosive case. For Figure 3.7e, the range of $n_1 m_1 / nm$ is also similar 30 to 50% and there appears to be a local maximum for C at A6 corresponding to the peak of m_C . For the intense events, Figure 3.7f again shows the similarity between k and C and the values ranging 1 to 3%. Figure 3.7g shows that $n_3 m_3 / nm$ ranges from 10 to 30% with a peak at A6 for C . It is worth noting that $n_3 m_3 / nm$ for k is higher at A9 and decreases shoreward throughout the surf zone, and this same trend was seen earlier in the erosive case.

Table 3.2 summarizes the intermittency statistics of k and C near the bed for all runs in this study. Because the intermittency statistics were stable over time for the EU and AU case, we categorized the runs into bar crest (E11; and A1, A2, A5), bar trough (E1-E6, E10; and A2, A4, A6), and inner surf zone (E7-E9; and A7, A8) to facilitate comparison between the erosive and accretive condition and with the data of JS92 and CK00. We excluded A9 because it was well outside the surf zone. The mean of the intermittency statistics of associated runs is given with the standard deviation in parentheses. Two general observations can be made. First, coherent events occur for less than 10% of the record yet account for approximately 40% of the motion. This is true for both erosive and accretive conditions, for both turbulence and suspended sediments, and across the surf zone. Second, the intense events occur for about 2% of the record and contain approximately 20% of the motion. Similar to coherent events, this applies for both k and C , for both nearshore conditions, and across the surf zone. In some sense, it is remarkable that the statistics should be so similar for two distinctly different processes, especially when one recalls Figure 3.4 showing that there is not necessarily a clear correlation between an intermittent turbulent and sediment suspension events.

Upon careful inspection of Table 3.2, one may notice an exception to the symmetry in the k and C statistics at the bar trough for the accretive case. Here, the portion of the record containing coherent and intense events ($n_1 / n = 7.0$, $n_3 / n =$

2.6) is larger than at the bar crest or inner surf zone ($n_1 / n = 5.7$, $n_3 / n = 1.9$) and the percent of the motion is larger as well. We speculate that at this location, there are additional mechanisms which cause a significant increase to the local suspended sediment concentration record and that these mechanisms are less important at other surf zone locations.

We also use Table 3.2 to compare the results of the intermittency of wave breaking turbulence by CK00 and sediment suspension by JS92. CK00 conducted small-scale laboratory measurements of turbulence induced by regular waves spilling on a rough and impermeable slope. The location of L3 by CK00 represents the transition region where the wave changed from organized motion to a turbulent bore and is qualitatively consistent with the bar trough in the present study. The locations of L4-L6 in CK00 were measured in the inner surf zone. Although there is a difference in wave type (regular vs. irregular), experimental scale (small vs. large) and bottom shape (plane vs. barred) between CK00 and the present study, Table 3.2 show surprisingly similar statistics for turbulence at the bar trough (transient region CK00) and inner surf zone.

Furthermore, the statistics of C are compared with JS92, who conducted the field measurement at the Army Corps of Engineers Field Research Facility (FRF) in Duck, North Carolina. They provided the intermittency statistics with the sediment concentration measured 0.13 m above the bed (Figure 3.8 in JS92). The locations 3

and 4, and the locations 1 and 2 in JS92 are chosen for a bar crest and inner surf zone, respectively, to be compared with the present study. Again, the statistics of JS92 and the present study agree reasonably well, except for the duration of events (n_1/n and n_3/n). The discrepancy may arise from the slightly different definition of the events. The present study defines the start and end of events when the sediment load exceed the mean plus one (or three) standard deviation(s), while JS92 used the mean concentration as the threshold of the start and end of events which would increase the duration of the intermittent event. Overall, the intermittency statistics of k and C near the bed suggest that the intermittent and intense features of k and C is a general aspect in the surf zone, and contribute to the total sediment suspension.

Taken together, Figures 3.5-3.7 and Table 3.2 show that there is a remarkable similarity in the statistics of intermittent turbulence and sediment suspension. However, they do not indicate to what degree these signals are correlated. Recalling the symbols of Figure 3.3, we now turn our attention to the correlation and conditional probabilities between k and C . Figure 3.8 shows the cross correlation between k and C for the erosive and accretive cases averaged for all the runs listed in Table 3.1. The figure shows that the peak correlation is slightly less than 0.6 for both cases and that k leads C by approximately $0.2T_p$ for the erosive case and $0.1T_p$ for the accretive case. Furthermore, the accretive case shows a

more narrow correlation than the erosive case. The horizontal line in Figure 3.8 shows the window length of $\pm T_p / 2$ used in the conditional sampling.

To examine the correlation between the coherent events of k and C , the correlated events between k and C are denoted N_{kC} and are counted as follows. If the peaks of the smoothed k and C signals are within the window length of $\pm T_p / 2$, then those two events are regarded as correlated and illustrated as closed triangles and circles in Figures 3.3c and 3.3d, respectively. This window length takes into account situations where sediment suspension occurs in the vicinity of the sensor and then oscillates with the wave-induced motion. In this way, the analysis can account for nearby suspension events which are not directly at the sensor while at the same time excluding suspension events that were advected to the location over a longer time scale.

Table 3.3 lists the results of the conditional sampling of k and C near the bed. As shown in Figure 3.3c, the time series of k were moving-averaged with 2s-filter and peaks of the coherent events were indicated as triangles. N_k in Table 3.3 denotes the number of these peaks. Similarly, the peaks of the coherent suspension events were indicated as circles in Figure 3.3d, and N_C in Table 3.3 represents the number of these events. Two conditional probabilities were calculated. First, N_{kC} / N_k represents the probability of the correlated events (i.e., turbulence-

induced suspension events) on the condition of the coherent turbulent events. The statistics of N_{kC} / N_k represent that only 20 to 35% (9% at the bar crest in the erosive case) of the coherent turbulent events are associated with the coherent suspension events. This implies that it will be difficult to simply relate turbulent events to suspension events. In other words, many of the turbulent events such as the one identified in Figures 3.4c and 3.4d for $390 \text{ s} < t < 400 \text{ s}$ may be efficient at dissipating wave energy throughout the water column, but they do not cause a local suspension of sediments.

Second, N_{kC} / N_C represents the probability of the correlated event on the condition of the coherent sediment suspension events. The results of N_{kC} / N_C show that 50 to 65% (40% at the bar crest in the erosive case) of the coherent sediment suspension events are associated with the coherent turbulent events. All of these values are fairly high, showing a maximum value (approximately 65%) at the bar crest in the accretive case and a minimum value (approximately 40%) at the bar crest in the erosive case. This implies that roughly half of the suspension events can be attributed to turbulent events associated with wave breaking. The difference of N_{kC} / N_k at the bar crest between the erosive and accretive case can be explained by the different types of breakers. As mentioned in Section 2, spilling breakers were observed to be predominant in the erosive case whereas plunging breakers were observed to be predominant in the accretive case. The large and

coherent vortices produced by plunging breakers can hit the bottom with more intensity and cause more sediment suspension than spilling breakers (e.g., Aagaard and Hughes, 2010).

3. 4. 2. Cross-shore and vertical distributions of intermittent turbulence and sediment concentration

In this section, the analysis on the intermittent turbulence and sediment concentration is extended from the outer region of the bottom boundary layer up to $\zeta = 0.50$ m for turbulence and $\zeta = 0.32$ m for sediment concentration. Figure 3.9 shows the cross-shore and vertical distributions of the intermittency statistics of k and c for EQ state. Instead of using the integrated sediment concentration (i.e., suspended loads, C), we use the sediment concentration (c) at each elevation for this subsection. Figure 3.9a shows m_k and $m_k + \sigma_k$ which are used as thresholds for the coherent event of intermittency analysis. Similar to statistics near the bed (Figures 3.6c and 3.7c), σ_k is almost twice of m_k at each elevation. The trend of $m_k + 3\sigma_k$ for the intense events is similar to $m_k + \sigma_k$ and it is not shown for brevity. Large values of m_k are shown near the water surface level ($\sim 500 \text{ cm}^2/\text{s}^2$) and decays exponentially toward the bottom (50 to $100 \text{ cm}^2/\text{s}^2$) for all cross-shore location. Figure 3.9b shows m_c and $m_c + \sigma_c$ at each elevation. Most of m_c and $m_c + \sigma_c$ are confined in the lower region of water column. For example, at E10, the average of m_c from the lower probe ($\zeta = 0.01$ to 0.09 m) is $2.41 \text{ kg}/\text{m}^3$ while

that from the upper probe ($\zeta = 0.09$ to 0.32 m) is 1.29 kg/m^3 . Comparing over the cross-shore locations, sediment concentration near the bar region is large and then decays rapidly shoreward. For example, the depth-averaged m_c for E10 (2.03 kg/m^3) is larger than E9 (0.20 kg/m^3) by an order of magnitude. This indicates that most of dynamic sediment motion occurs in the vicinity of the bar.

Figures 3.9c and 3.9d shows the intermittency statistics of n_3 / n and $n_3 m_3 / nm$. The trend of the coherent events (n_1 / n and $n_1 m_1 / nm$) are similar to the intense events and only the intense events are plotted for brevity. Inside the surf zone (shoreward from the bar), the values of $(n_3 / n)_k$ and $(n_3 m_3 / nm)_k$ are uniform over water depth, ranging from 1 to 2% for $(n_3 / n)_k$ and 15 to 20% for $(n_3 m_3 / nm)_k$. Little variance over the water depth is also consistent with the results inside the surf zone in CK00. The uniform intermittency of k over water depth suggests that most of the intense turbulent events (e.g., strong vortex motions) generated from the water surface level are transported to the bottom with the similar percentage of the intense events, although the thresholds for intermittency abruptly decreases downward (Figure 3.9a). On the other hand, the duration of sediment concentration during the intense events ($(n_3 / n)_c$) is similar to the intense turbulence event ($(n_3 / n)_k$) as shown in Figure 3.9c. However, unlike the case of k , $(n_3 m_3 / nm)_c$ for the sediment concentration show more of a variation over

depth with larger values near the bottom (Figure 3.9d), indicating that most of the intermittent motions are occurred near the bed.

Figure 3.10 for the AQ state is plotted similar to Figure 3.9 for the EQ state. In general, Figure 3.10a shows smaller turbulence intensity than Figure 3.9a by approximately 30% because of the smaller wave height conditions (and subsequently smaller energy loss) in the accretive case. Figure 3.10b shows a similar vertical distributions of m_c and $m_c + \sigma_c$ at the bar trough (A6) with the erosive case (E10 in Figure 3.9b). However, comparing the vertical structures of m_c at the bar crest between the erosive and accretive cases, the accretive case shows a more uniform vertical structure at the bar crest (A5) than the erosive case (E11 in Figure 3.9). This difference can be explained by the different types of breakers. Strong vortex motions generated from plunging breakers at the bar crest could enhance the sediment mixing throughout water column than spilling breakers (Wang et al., 2002; Aagaard and Hughes, 2010). The strong mixing at the bar crest in the accretive case is also consistent with the results of Table 3.2, where the conditional probabilities at the bar crest in the accretive case shows larger values than the erosive case. Outside the surf zone (A9), m_c is substantially smaller compared to the bar region. In Figure 3.10c, $(n_3 / n)_k$ and $(n_3 / n)_c$ inside the surf zone are vertically uniform similar to the EQ state (Figure 3.9c). However, in Figure 3.10d, large $(n_3 m_3 / nm)_c$ is shown near the bed, while $(n_3 m_3 / nm)_k$ is

relatively constant over water depth, similar to the erosive case. Overall, from the investigation on the both beach conditions, it can be concluded that the percentage of intermittency (n_3 / n) is vertically constant and quantitatively similar for both k and c , while the percentage of the contained motion ($n_3 m_3 / nm$) for k and c are different. Furthermore, $(n_3 m_3 / nm)_k$ is depth uniform, but $(n_3 m_3 / nm)_c$ increases near the bed.

3. 4. 3. Contribution of intermittent sediment suspension on cross-shore transport

In the following, we investigate the contribution of the intermittent suspension events to the cross-shore sediment transport. Figure 3.11 shows hydrodynamic conditions and morphological change in the EQ state, including wave conditions (Figure 3.11a), flow conditions (low-frequency motion in Figure 3.11b, wave-induced motion in Figure 3.11c), cross-shore sediment flux (Figure 3.11d), and subsequent bathymetry change (Figure 3.11e). Figure 3.11a shows that the significant wave height increases and then decreases as the waves pass over the bar ($x = 60$ m), indicating that most of waves break at this location. Figure 3.11b shows the mean of the low-frequency motion (\bar{u}_{lf}) near the bed (at ADV1). To investigate the distinctive flow conditions during the intense suspension events, the mean of the low-frequency motion during the intense suspension events is plotted (closed dot) in addition to the mean of the low-frequency motion during the whole

time series (open triangle). While \bar{u}_{lf} for the whole time series are uniform across the surf zone, \bar{u}_{lf} for the intense suspension events varies in the cross-shore locations with the offshore peak at the bar crest, suggesting that the suspended sediments are driven offshore by the strong low-frequency motion at the bar crest. Similar to Figure 3.11b, Figure 3.11c shows the mean of u_{wave} (\bar{u}_{wave}) during the intense suspension events and the whole time series. Contrary to the low-frequency motion, most of the intense suspension events are in phase with the onshore wave-induced motion, except at the shoreline.

Figure 3.11d shows the depth-integrated cross-shore sediment flux (q) during the intense suspension events and the whole time series. The depth-integrated cross-shore sediment flux (q) is calculated as follows:

$$q = \sum \sum (u \cdot c) \Delta t \Delta \zeta \quad (3.6)$$

where, Δt is a time step, and u is the total measured time series (including low frequency, wave, and turbulent components). Velocities measured at $\zeta = 0.01, 0.05, 0.09, 0.20, 0.31,$ and 0.50 m were linearly interpolated to be paired with the sediment concentration at the elevation of FOBS. The sediment fluxes summed over, except for the first segment, at each elevation of FOBS. Then they were integrated from $\zeta = 0.01$ m to 0.32 m. From this figure, it is found that the sediment flux directed offshore during both the intense suspension events and the whole time series, with the smaller magnitude of the sediment flux during the

intense suspension events. The offshore sediment flux is consistent with the bathymetric changes shown in Figure 3.11e.

Figure 3.12 for the AQ state is plotted similar to Figure 3.11 for the EQ state. Compared to the EQ state, the AQ state shows smaller wave conditions (Figure 3.12a), weaker low-frequency motion (Figure 3.12b), but larger onshore wave-induced motion during the intense suspension events (Figure 3.12c) by a factor of 2-3. Consequently, it is clearly observed that the intense suspension events drive the onshore sediment transport in the AQ case, especially at the bar trough (A6) and slightly onshore of the bar trough (A7) (Figure 3.12d). Although the sediment flux during the whole time series is still directed offshore due to the undetected onshore sediment transport beyond the range of sensors (e.g., onshore-directed bed-load transport below the bottom of FOBS and suspended sediment transport above the top of FOBS), we can conclude that the intense suspension events drive the onshore sediment transport with the wave-induced motion in the AQ state.

Finally, Figure 3.13 shows a comparison of the contribution of the intermittent sediment suspension events with the field work of JS92. The surf zone length (the distance from the bar crest to shoreline) of JS92 was approximately 75 m, while the distance for the present study was about 20 m. To compare the cross-shore locations between the present study and JS92, the cross-shore locations are normalized by the surf zone length, with $x^*=0$ at the bar crest and $x^*=1$ at the

shoreline, where x^* is the normalized cross-shore location by the surf zone width. In Figure 3.13a, the cross-shore variation of $n_3 m_3 / nm$ of C for the both EQ and AQ cases are compared with the same statistics at the sediment concentration measured at $\zeta = 13$ cm from JS92. This figure shows all three data sets have the peak of $n_3 m_3 / nm$ around the bar crest (landward of the bar crest for the present study and seaward of the bar for JS92) and then decrease shoreward. The slight difference of the peaks may be attributed to that the JS92 case had a more energetic case (1.5 m significant wave height and 13 second period) and additional wave breaking seaward of the bar or that the bar was still moving offshore during their measurements. Figure 3.13b shows the net sediment transport for the intense suspension events. The net sediment transport for the EQ and AQ state shows a similar order of magnitude in opposite directions. The larger sediment flux for JS92 is because the sediment flux was measured at 13 cm above the bottom whereas it was measured from 1 cm to 32 cm from the bed in the present study. The measurement at 13 cm above the bottom in JS92 might not include the offshore sediment fluxes which were mainly occurred near the bed. Overall, the comparison of this study with the field work by JS92 confirmed that the intermittent suspension events significantly contribute to the onshore or offshore sediment transport and consequent bathymetric changes.

3. 5. Discussions

3. 5. 1. Sediment suspension mechanism in addition to turbulence

In Table 3.3 Column 7, the conditional probabilities show a fairly close relationship between the turbulence and sediment suspension events; however, the results still indicate that a significant portion (approximately 50%) of the suspension events are caused by mechanisms other than turbulence induced by wave breaking. Here, we investigate the relationship between sediment suspension and the low-frequency motions. The suspension events uncorrelated with turbulence are described with the subscript of $C - k$, using the notation of the difference of sets. Note that the suspension events with uncorrelated turbulence cases are also indicated in Figure 3.3a with open circles. The mean of the low-frequency motion at ADV1 ($\zeta = 0.01$ m) for this case is notated as $(\bar{u}_{lf})_{C-k}$, while \bar{u}_{lf} represents the mean of the low-frequency motions for the time series.

Comparing \bar{u}_{lf} between the erosive and accretive cases, the erosive case shows larger \bar{u}_{lf} values than the accretive case as expected. Comparing $(\bar{u}_{lf})_{C-k}$ with \bar{u}_{lf} in Table 3.3, $(\bar{u}_{lf})_{C-k}$ are larger than \bar{u}_{lf} by a factor of 1.3 to 2.3 in all of the erosive cases and over the bar crest and inner surf zone for the accretive case, indicating that the significant suspension events uncorrelated with turbulence occur under the condition of strong undertow. This can be attributed to advection of sediment suspended elsewhere. Previous literatures observed a large cloud of sediments when there is a strong current near the sensor (e.g., Black et al. 1995).

However, it is very challenging to distinguish the local sediment suspension from advection, and further investigation is needed.

Of note is that the only exception of the larger $(\bar{u}_{lf})_{C-k}$ than \bar{u}_{lf} is found at the bar trough in the accretive case. The magnitude of $(\bar{u}_{lf})_{C-k}$ for this case shows lower value than \bar{u}_{lf} ($(\bar{u}_{lf})_{C-k} / \bar{u}_{lf} = 0.63$). Along with the small values of N_{kC} / N_k and N_{kC} / N_C , the small value of $(\bar{u}_{lf})_{C-k}$ for this case implies that the near bed suspension is induced by something other than turbulence by wave breaking or horizontal advection. A possible explanation of the sediment suspension at this case can be pressure gradients near the bed (e.g., Madsen, 1974; Cox et al., 1991; Foster et al., 2006; Suzuki et al., 2010). The pressure gradient can cause a ‘momentary bed failure’ during the passage of near-breaking waves or breaking waves (Madsen, 1974). Especially, since plunging breaker has more abrupt transition features than spilling breakers, the pressure gradient near the bed is probably an important sediment suspension mechanism in the accretive case where plunging breaker predominate. Furthermore, because an abrupt transition of breaking waves occur mostly at the bar trough, this effect can be maximized at this location, under the weaker low-frequency motion (undertow) in the accretive case (Table 3.3, Figures 3.11 and 3.12).

3. 5. 2 Intermittency on the sediment transport modeling

The present paper may be useful for developing predictive models, such as a stochastic model, of sediment transport by allowing a better parameterization of turbulence induced by wave breaking. Many of the present models describe the complex sediment suspension process with ad-hoc parameterization. However, as noted by Hanes (1988), an accurate quantitative estimate of the sediment transport undergoing intermittent suspension can be achieved with an understanding of the statistical distribution of the suspension events. For example, Kobayashi et al., (2008) introduced the probabilities of sediment movement and suspension in their formulation to predict cross-shore sediment transport. They calculated the probability of sediment movement, assuming that the horizontal velocity is following the Gaussian distribution. If we incorporate the intermittent features, i.e. a probability distribution, of turbulence and sediment suspension, and the relationship between them (Table 3.3) in the modeling, we could obtain a better parameterization in the prediction model.

3. 6. Conclusions

In the present study, a laboratory experimental data of free surface elevation, fluid velocity, and sediment concentration were obtained using a resistant-type wave gauge, ADV and FOBS in the surf zone, for the erosive and accretive beach cases. The data sets were used to investigate intermittent characteristics of turbulence, sediment suspension and transport in the surf zone. The main conclusions are summarized as follows.

- (1) Intermittent turbulence and sediment suspension near the bed (from $\zeta = 0.01$ m to 0.09 m), including the bar crest, the bar trough, and the inner surf zone, were investigated. The results showed similar intermittency statistics over the cross-shore locations, although the thresholds used for the intermittency analysis varied. The comparison of intermittency between the present study and the previous studies (Cox and Kobayashi, 2000; Jaffe and Sallenger, 1992) agrees well despite the different experimental conditions. The similar intermittency of k and C near the bed suggests that turbulence and sediment suspension can be characterized as a self-similar, intermittent process in the surf zone.
- (2) The relationship between the coherent turbulence and sediment suspension events was examined. The conditional probabilities of N_{kC} / N_k and N_{kC} / N_C were introduced based on the number of the intermittent turbulence, suspension, and correlated events with a window length of $\pm T_p / 2$. The results of N_{kC} / N_k showed that 20~35% (~10% at the bar crest in the erosive case) of the turbulent events may trigger the suspension events. Also, the results of N_{kC} / N_C indicate 50~65% (~40% at the bar crest in the erosive case) of the suspension events are induced by the turbulent events. The large probability in the accretive case mainly arises

from the predominating plunging breakers, while the small probability in the erosive case results from the predominating spilling breakers.

- (3) Possible mechanisms of the sediment suspension other than turbulence were discussed. The sediment suspension events uncorrelated with turbulence were mostly induced when strong offshore low-frequency motion were present, highlighting the need for better understanding of advection in the surf zone. The bar trough in the accretive case was an exception, and the horizontal pressure gradient was discussed as a contributing mechanism.
- (4) The intermittency statistics throughout water column were examined. Although the thresholds of intermittent events, i.e, a mean plus one (three) standard deviation(s), were varied vertically for both k and c , the duration of intermittent events were uniform over water depth and quantitatively similar each other. The motions contained in the intermittent events of k , $(n_3 m_3 / nm)_k$, were vertically uniform, whereas $(n_3 m_3 / nm)_c$ varied vertically, showing large values near the bed.
- (5) The contribution of the intense sediment suspension to the cross-shore sediment transport was examined. The intense suspension events drove the onshore sediment transport mainly with the wave-induced motion. The

onshore sediment transport was observed in the AQ state during the intense suspension events, while the EQ state shows offshore sediment flux even in the intense suspension events. Comparison these results with the field work by Jaffe and Sallenger (1992) confirmed the importance of intermittency on the cross-shore sediment transport.

Acknowledgements

This work was supported by the National Science Foundation (OCE-0351741).

The authors are grateful to all participants during the CROSSTEX project and the staff at the O. H. Hinsdale Wave Research Laboratory. The authors are grateful to Andrea Ogston of the University of Washington for the loan of the FOBS. Chris Scott and Meghan Irving contributed to the experimental measurement and preliminary analysis. Dan Cox gratefully acknowledges support by the Japan Society for the Promotion of Science and his hosts at the Disaster Prevention Research Institute of Kyoto University during the preparation of this manuscript.

References

- Aagaard, T., and M. G. Hughes, 2006, Sediment suspension and turbulence in the swash zone of dissipative beaches, *Marine Geology*, 228, 117–135.
- Aagaard, T., and M. G. Hughes, 2010, Breaker turbulence and sediment suspension in the surf zone, *Marine Geology*, 271, 250-259.

- Battjes, J. A., 1974., Surf similarity, *Proceedings of the 14th International Conference on Coastal Engineering*. 466-480. Am. Soc. Civil. Eng., New York
- Beach, R. A., and R. W. Sternberg, 1988, Suspended sediment transport in the surf zone: responses to cross-shore infra-gravity motion, *Marine Geology*, 80, 61-79.
- Black, K. P., R. M. Gorman, and G. Symmonds, 1995. Sediment transport near the breakpoint associated with cross-shore gradients in vertical eddy diffusivity, *Coastal Eng.*, 23, 95-114
- Bouws, E., H. Gunther, W. Rosenthal, and C. L. Vincent. 1985. Similarity of the wind wave spectrum in finite depth water, Part I- Spectral form, *J. Geophys. Res.*, 90 (C1), 975-986.
- Butt, T., P. Russell, J. Puleo, J. Miles, and G. Masselink. 2004. The influence of bore turbulence on sediment transport in the swash and inner surf zone, *Continental Shelf Research*, 24, 757-771
- Butt, T., P. Russell, J. Puleo, J. Miles, and G. Masselink. 2005, The application of Bagnold-type sediment transport models in the swash zone, *Journal of Coastal Research*, 21, 887-895.
- Cox, D. T., and N. Kobayashi, 2000, Identification of intense, intermittent coherent motions under shoaling and breaking waves, *J. Geophys. Res.*, 105, C6, 14223-14236.

- Cox, D.T., N. Kobayashi, and H. Mase, 1991, Effects of Fluid Accelerations on Sediment Transport in Surf Zones, *Proc. of Coastal Sediments 91*, Am. Soc. Civil Engrg., 447-461.
- Cox, D. T., and S. L. Anderson, 2001, Statistics of intermittent surf zone turbulence and observations of large eddies using PIV, *Coastal Eng. J.*, 43, 121-131.
- Downing, J, 2006. Twenty-five years with OBS sensors: The good, the bad and the ugly, *Continental Shelf Research*, 26, 2299-2318.
- Foster, D. L., R. A. Holman, and R. A. Beach, 1994, Correlation between sediment suspension events and shear instabilities in the bottom boundary layer of the surf zone. *Proceedings of Coastal Dynamics '94*, 712-726, Am. Soc. Civil Eng., New York
- Foster, D. L., A. J. Brown, R. A. Holman, and P. Natoo, 2006, Field evidence of pressure gradient induced incipient motion, *J. Geophys. Res.*, 111, C05004.
- Fugate, D., C. and C. T. Friedrichs, 2002. Determining concentration and fall velocity of estuarine particle populations using ADV, OBS and LISST, *Continental Shelf Research*, 22, 1867-1886.
- Gallagher, E.L., S. Elgar and R.T. Guza, 1998, Observations of sand bar evolution on a natural beach, *J. Geophys. Res.*, 103 (C2), 3203–3215.
- Hanes, D., M. and D. A. Huntley, 1986. Continuous measurements of suspended sand concentration in a wave dominated nearshore environment, *Continental Shelf Research*, 6, 585-596.

- Hanes, D., M., 1988, Intermittent sediment suspension and its implications to sand tracer dispersal in wave-dominated environments, *Marine Geology*, 81, 175-183.
- Henderson, S. M., J. S. Allen, and P. A. Newberger, 2004, Nearshore sandbar migration predicted by an eddy-diffusive boundary layer model, *J. Geophys. Res.*, 109, C06024, Doi:10.1029/2003JC002137
- Hoefel, F. and S. Elgar, 2003. Wave-induced sediment transport and sandbar migration, *Science*, 299, 1885-1887
- Hsu, T.-J, S. Elgar, and R. T. Guza, 2006, Wave-induced sediment transport and onshore sandbar migration, *Coastal Eng.*, 53, 817-824
- Jaffe, B. E., R. W. Sternberg, and A. H. Sallenger Jr., 1984, The role of suspended sediment in shore-normal beach profile changes, *Proceedings of the 19rd International Coastal Engineering Conference*, 2, 1983-1996, Am. Soc. Civil. Eng., New York
- Jaffe, B. E., and A. H. Sallenger Jr., 1992, The contribution of suspension events to sediment transport in the surf zone, *Proceedings of the 23rd International Coastal Engineering Conference*, 3, 2690-2693, Am. Soc. Civil. Eng., New York
- Kobayashi, N., A. Payo, A., and L. Schmied, 2008, Cross-shore suspended sand and bedload transport on beaches, *J. Geophys. Res.*, 113, C07001.

- Kubo, H., and T. Sunamura, 2001, Large-scale turbulence to facilitate sediment motion under spilling breakers. *Proceedings of Coastal Dynamics '01*, 212-221, Am. Soc. Civil Eng., New York
- Madsen, O. S., 1974., Stability of a sand bed under breaking waves, *Proceedings of the 14th International Conference on Coastal Engineering*. 776-794. Am. Soc. Civil. Eng., New York
- Mori, N., T. Suzuki, and S. Kakuno. 2007. Noise of acoustic Doppler velocimeter data in bubbly flows, *J. of Engrg Mech.*, 133, 122-125
- Nadaoka, K., M. Hino, and Y. Koyano. 1989. Structure of the turbulent flow field under breaking waves in the surf zone, *J. Fluid Mech.*, 204, 359-387.
- Nielsen. P., 1992. *Coastal bottom boundary layers and sediment transport*, World Scientific Publishing, Singapore, 324 pp.
- Ogston, A. S. and R. W. Sternberg, 1995. On the importance of nearbed sediment flux measurements for estimating sediment transport in the surf zone, *Continental Shelf Research*, 15, 1515-1524.
- Puleo, J. 2009, Tidal variability of swash-zone sediment suspension and transport, *Journal of Coastal Research*, 25 (4), 937-948.
- Roelvink, J. A., and M. J. F. Stive, 1989. Bar-generating cross-shore flow mechanisms on a beach, *J. Geophys. Res.*, 94, 4785-4800.
- Ruessink, B. G., 2010. Observations of turbulence within a natural surf zone, *J. Phys. Oceanogr.*, 40, 2696-2712.

- Scott, C. P., D. T. Cox, Shin, S. and Clayton, N., 2004. Estimates of surf zone turbulence in a large-scale laboratory wave flume. *Proceedings of the 29th International Conference on Coastal Engineering*. 379-391. Am. Soc. Civil. Eng., New York.
- Scott, N. V., T.-J. Hsu, and D. T. Cox, 2009, Steep wave, turbulence, and sediment concentration statistics beneath a breaking wave field and their implications for sediment transport, *Continental Shelf Research*, 29, 2303-2317.
- Shaw, W. J., and J. Trowbridge. 2001. The direct estimation of near-bottom turbulent fluxes in the presence of energetic wave motions, *J. Atmos. Oceanic Technol.*, 18, 1540-1557.
- Smith, G. G., and G. P. Mocke, 2002, Interaction between breaking/broken waves and infragravity-scale phenomena to control sediment suspension transport in the surf zone, *Marine Geology*, 187, 329–345.
- Svendsen, I., A, 1987. Analysis of surf zone turbulence, *J. Geophys. Res.*, 92, 5115-5124.
- Suzuki, T., A. Okayasu, and T. Shibayama. 2007. A numerical study of intermittent sediment concentration under breaking waves in the surf zone, *Coastal Eng.*, 54, 433-444.
- Suzuki, T., S. Shin, D. T. Cox, and N. Mori, 2010, Spatiotemporal characteristics of near-bed pressure gradient on a barred beach, *J. waterway, Port, Coastal and Ocean Engineering.*, 136, 327-336.

- Wang, P., B. A. Ebersole, E. R. Smith, and B. D. Johnson. 2002. Temporal and spatial variations of surf-zone currents and suspended sediment concentration, *Coastal Eng.*, *46*, 175-211.
- Yoon, H.-D, and D. T. Cox, 2010, Large-scale laboratory observations of wave breaking turbulence over an evolving beach, *J. Geophys. Res.*, *115*, C10007, Doi:10.1029/2009JC005748.
- Yu, Y., Sternberg, R. W., and R. A. Beach, 1993. Kinematics of breaking waves and associated suspended sediment in the nearshore zone, *Continental Shelf Research*, *13*, 1219-1242.

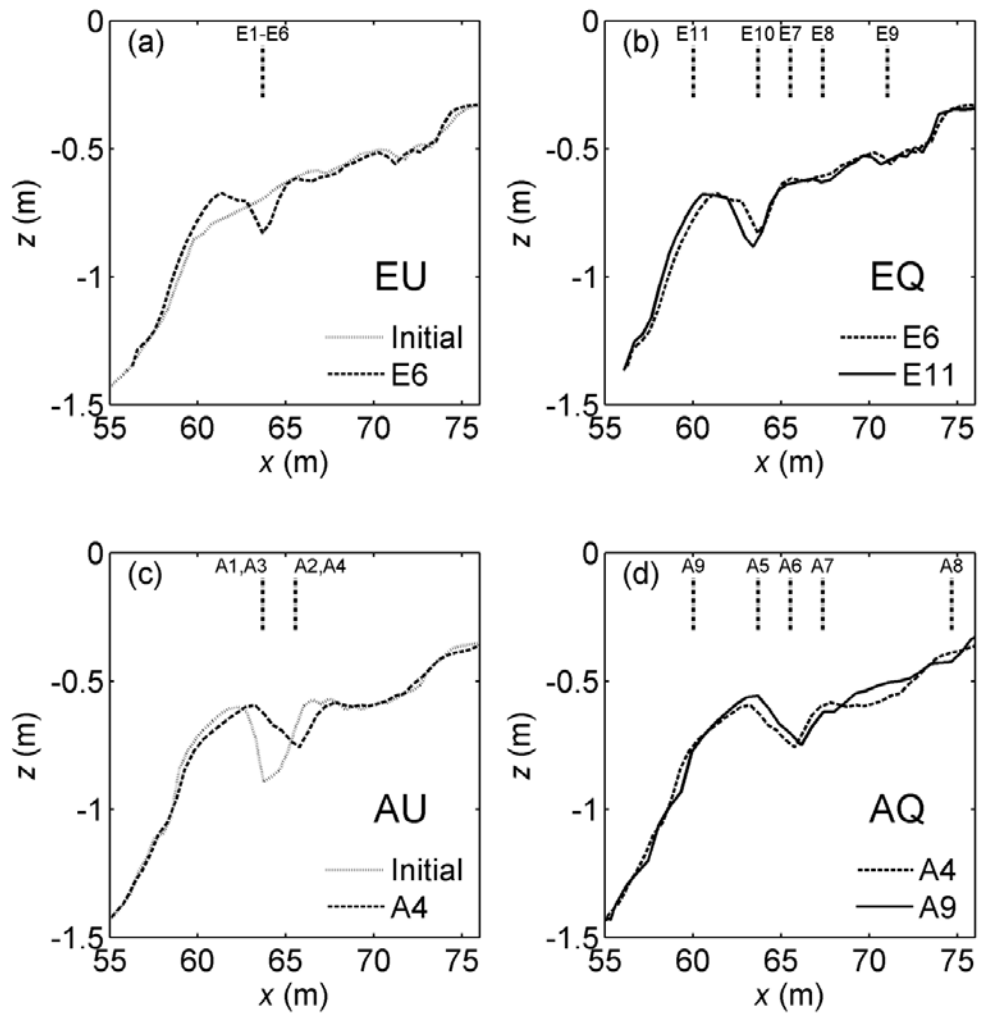


Figure 3.1: Bathymetry and cross-shore locations of the instrument array: (a) erosive and unstable (EU), (b) erosive and quasi-equilibrium (EQ), (c) accretive and unstable (AU), and (d) accretive and quasi-equilibrium (AQ). The vertical dashed lines represent the locations of the instrument array.



Figure 3.2: Instrument array on mobile cart: vertical stack of ADV (right) and FOBS (middle). Inset photo shows mobile cart in Large Wave Flume.

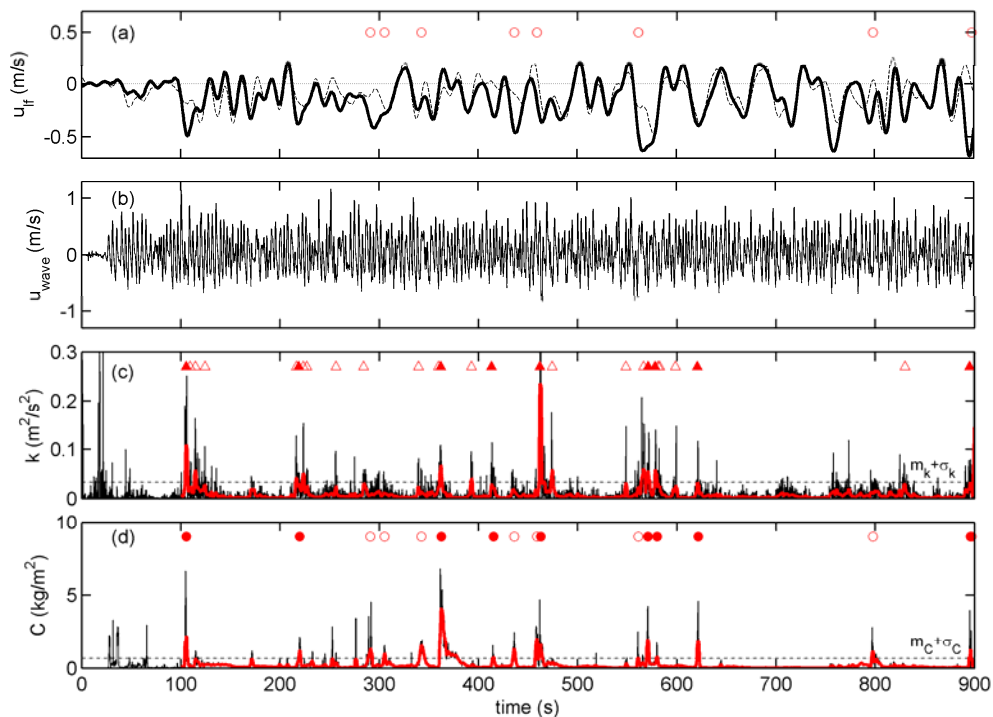


Figure 3.3: Temporal variation of (a) low-frequency motion of u , (b) wave-induced motion of u , (c) k estimated at ADV1 ($\zeta = 1$ cm) with ADV3 ($\zeta = 9$ cm), and (d) suspended load (C) detected at lower panel ($1 < \zeta < 9$ cm), for E2. In (a), thick solid line represents ADV1 ($\zeta = 1$ cm) and thin dashed line represents ADV6 ($\zeta = 50$ cm), and horizontal dotted line represents where $u_{lf} = 0$. In (b), wave-induced motion of ADV1 ($\zeta = 1$ cm) is plotted. In (c) and (d), the dash-dot lines indicate the mean plus a standard deviation of the time series. In (c) and (d), the thick lines represent the moving-averaging with 2-second filter length. The peak of each event over the mean plus one standard deviation is indicated as a triangle in (c) or a circle in (d). The closed triangles and circles denote the correlated events between k and C with a window length of $\pm T_p / 2$, while the open triangles and circles denote the uncorrelated events.

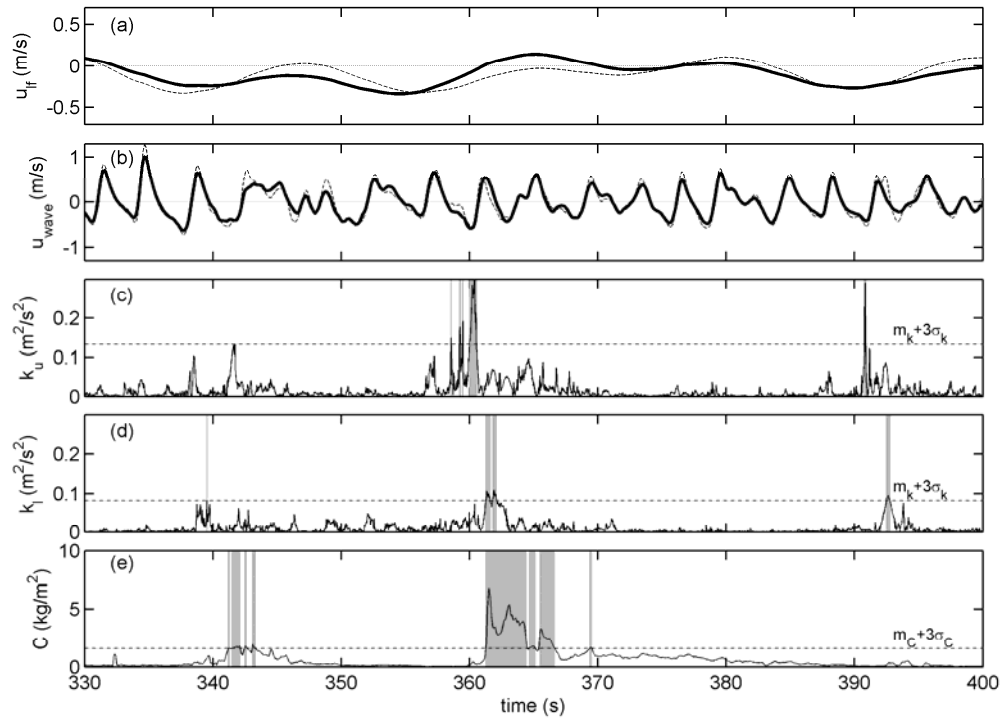


Figure 3.4: Temporal variation of (a) low-frequency motion of u , (b) incident waves motion of u , (c) k_u estimated at ADV6 ($\zeta = 50$ cm) with ADV5 ($\zeta = 31$ cm), (d) k_l estimated at ADV1 ($\zeta = 1$ cm) with ADV3 ($\zeta = 9$ cm), and (e) suspended load (C) detected at lower panel ($1 < \zeta < 9$ cm), for E2, in the range of $330\text{s} < t < 400\text{s}$. In (a) and (b), thick solid line represents ADV1 ($\zeta = 1$ cm) and thin dashed line represents ADV6 ($\zeta = 50$ cm). Dotted line represents where $u_{lf} = 0$ and $u_{wave} = 0$. In (c), k at ADV6 ($\zeta = 50$ cm) are denoted as k_u . In (d), k at ADV1 ($\zeta = 1$ cm) are denoted as k_l . In (c), (d), and (e), the dashed lines indicate the mean plus three standard deviations of the time series. The events over the mean plus three standard deviations are indicated as gray region.

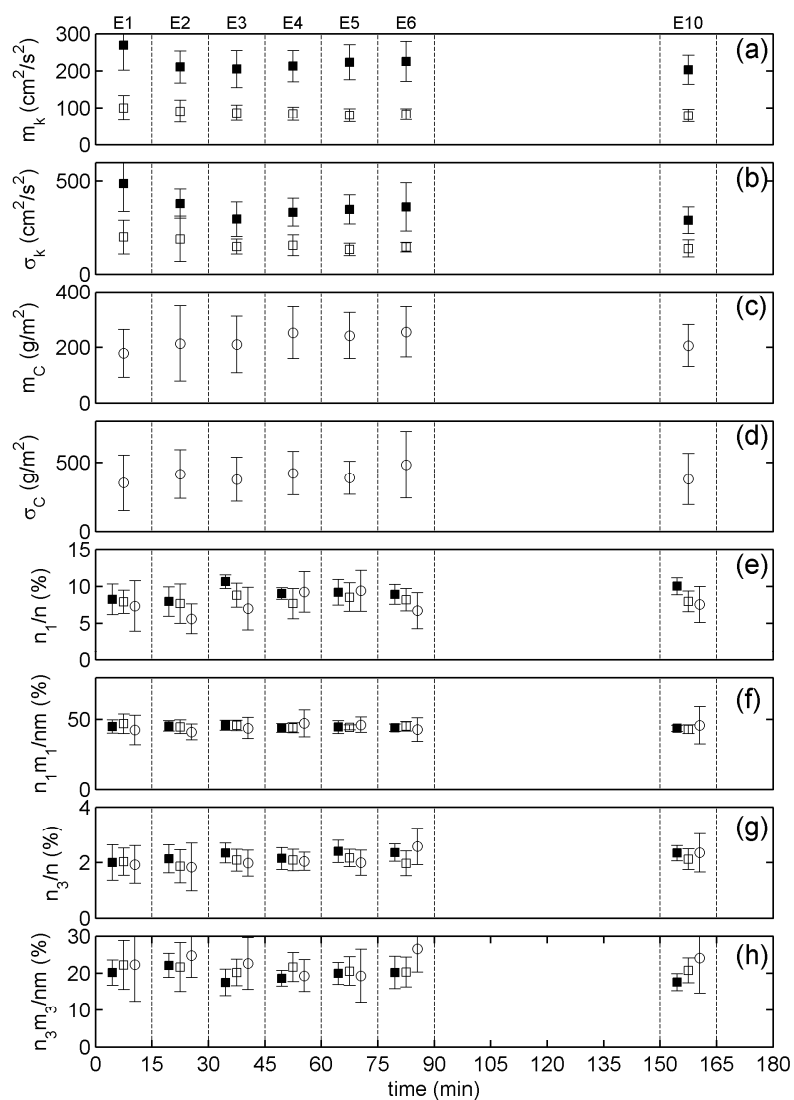


Figure 3.5: Temporal variation of: (a) mean of time-averaged k , (b) mean of standard deviation of k , (c) mean of time-averaged C , (d) standard deviation of C , (e) percentage of coherent events, (f) percentage of the motion contained in coherent events, (g) percentage of intense events, and (h) percentage of the motion contained in intense events, at bar trough, for erosive case. Symbols indicate the average of the eight 100-second segment estimation (total 800 sec), excluding the first segment. Closed square, open square, and open circle represent k_u , k_l (ADV2 was used for E4 and E5), and C , respectively.

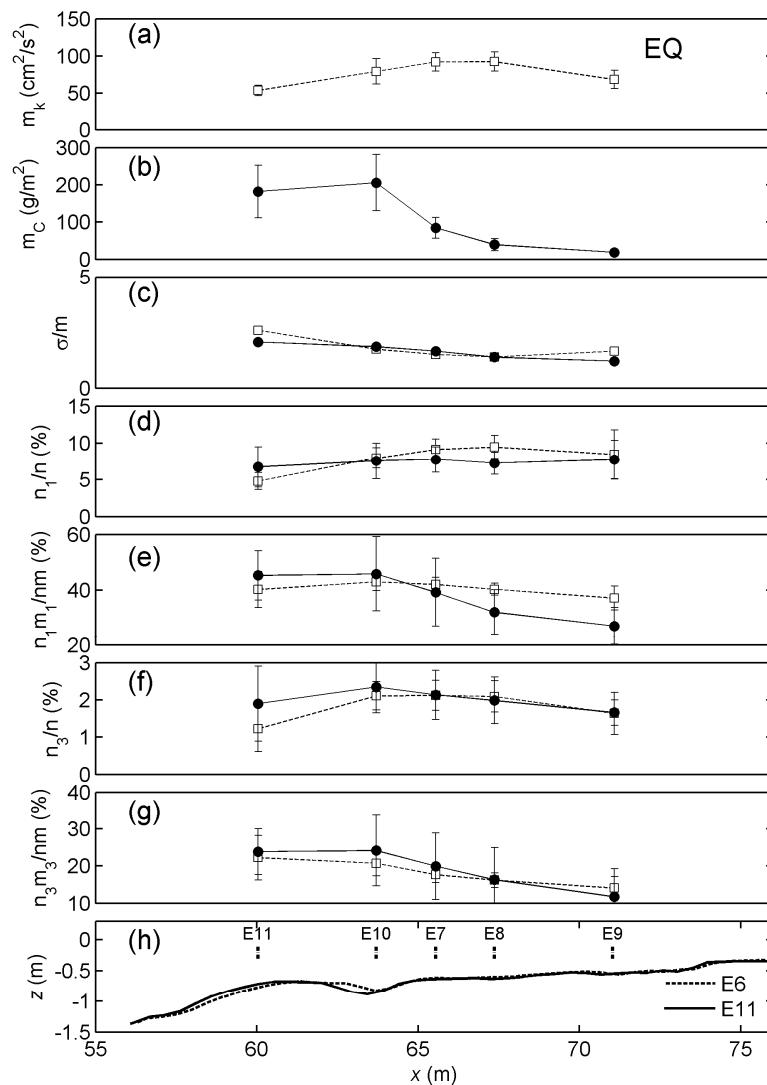


Figure 3.6: Cross-shore distribution of: (a) mean of time-averaged k , (b) mean of time-averaged C , (c) ratio of mean to standard deviation of k and C , (d) percentage of coherent events, (e) percentage of the motion contained in coherent events, (f) percentage of intense events, and (g) percentage of the motion contained in intense events, and (h) bathymetry and locations of the instrumental array for EQ. Symbols indicate the average of the eight 100-second segment estimation, excluding the first segment. Open square and open circle represent k and C , respectively.

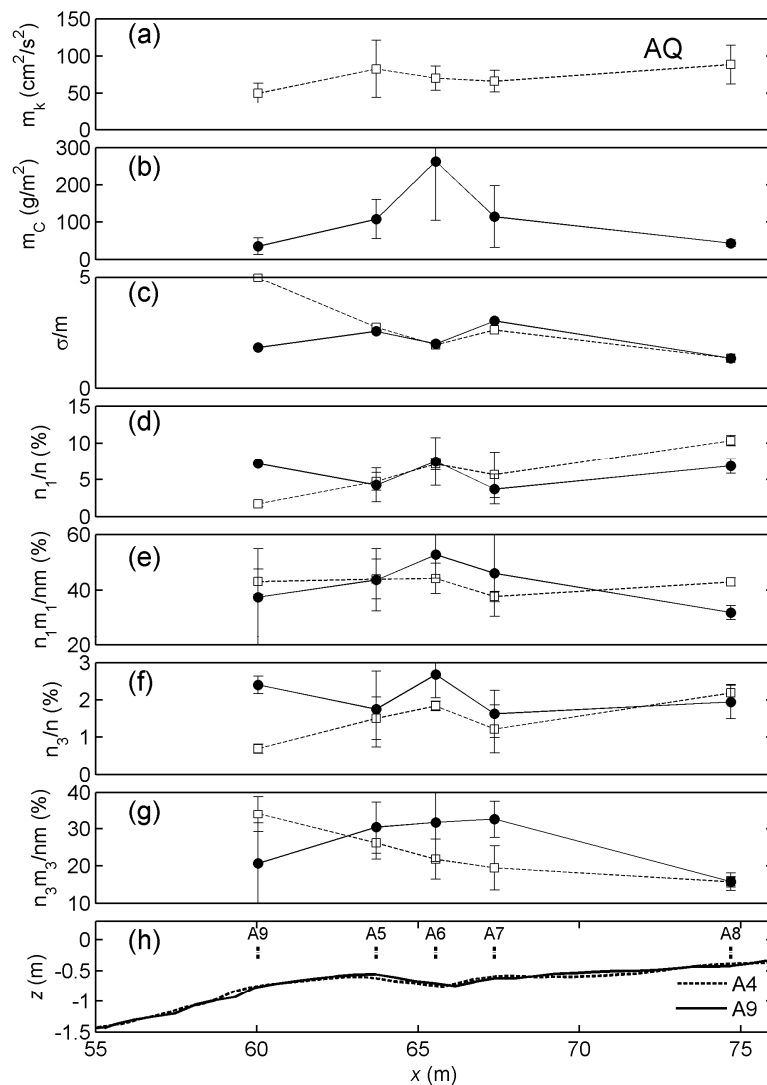


Figure 3.7: Cross-shore distribution of: (a) mean of time-averaged k , (b) mean of time-averaged C , (c) ratio of mean to standard deviation of k and C , (d) percentage of coherent events, (e) percentage of the motion contained in coherent events, (f) percentage of intense events, and (g) percentage of the motion contained in intense events, and (h) bathymetry and locations of the instrumental array for AQ. Symbols indicate the average of the four 180-second segment estimation, excluding the first segment. Open square and open circle represent k and C , respectively.

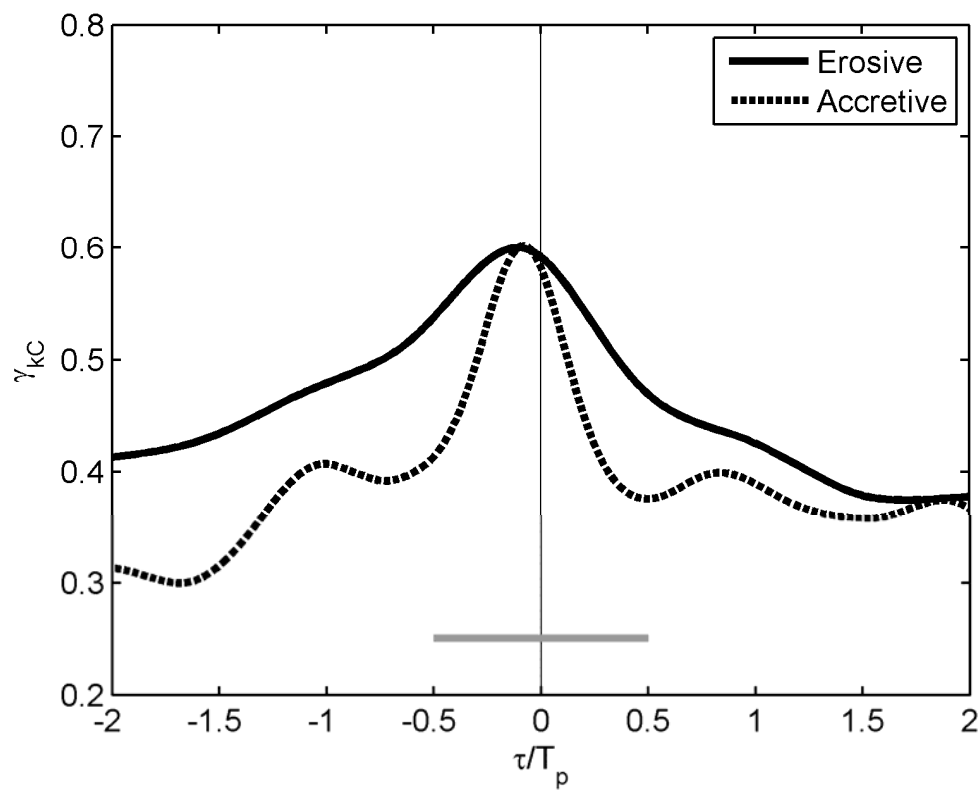


Figure 3.8: Cross-correlation (γ_{kC}) between k and C . The solid line represents the average of all erosive cases and the dashed line represents the average of all accretive cases. The (-) sign means that k leads C . The lag (τ) is normalized by peak period (T_p). The horizontal gray line represents the length of $\pm T_p / 2$.

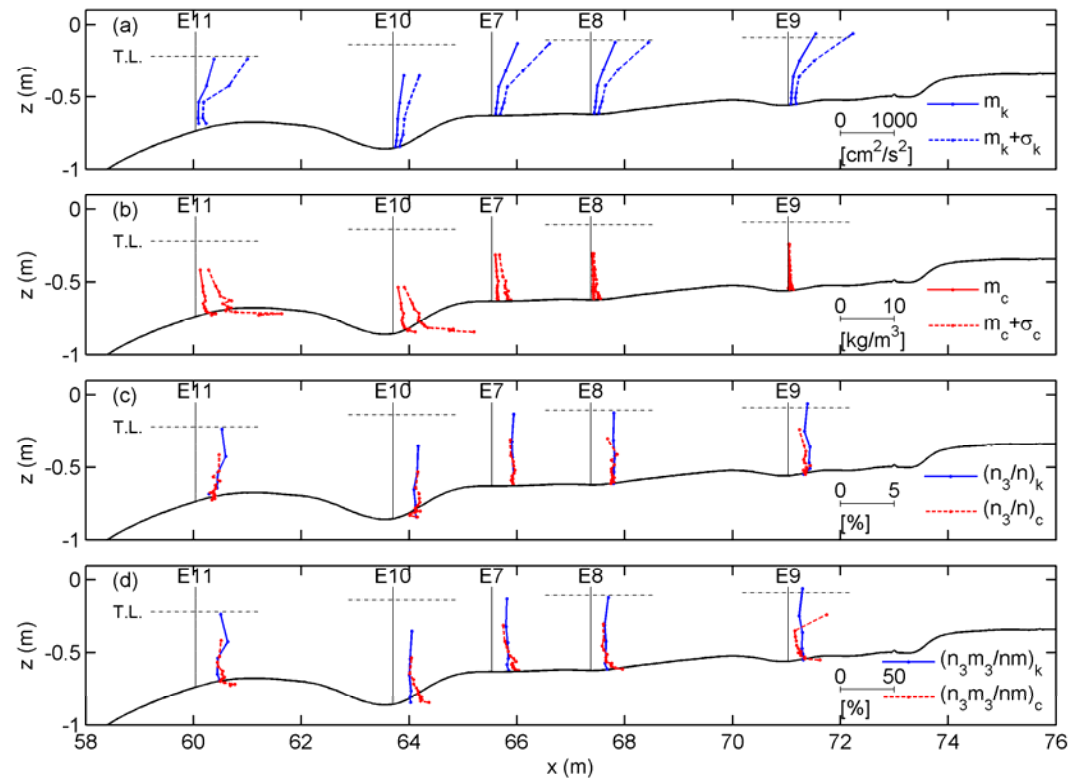


Figure 3.9: Cross-shore and vertical distribution of: (a) m_k and $m_k + \sigma_k$, (b) m_c and $m_c + \sigma_c$, (c) $(n_3/n)_k$ and $(n_3/n)_c$, and (d) $(n_3 m_3 / nm)_k$ and $(n_3 m_3 / nm)_c$, for EQ state. The average of the eight 100-second segment estimation is plotted. Bottom profiles are averaged during EQ state. Dash-dot line indicates wave trough level calculated as average of 1/3 lowest wave trough levels from zero-upcrossing.

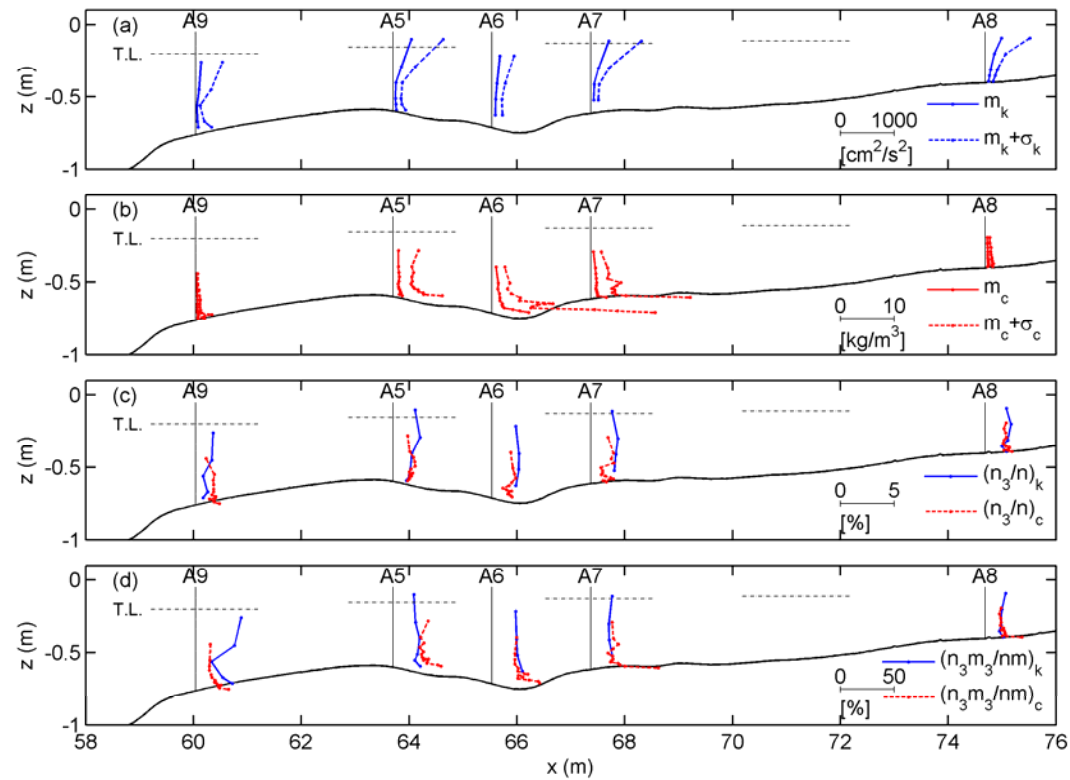


Figure 3.10: Cross-shore and vertical distribution of: (a) m_k and $m_k + \sigma_k$, (b) m_c and $m_c + \sigma_c$, (c) $(n_3/n)_k$ and $(n_3/n)_c$, and (d) $(n_3 m_3 / nm)_k$ and $(n_3 m_3 / nm)_c$, for AQ state. The average of the four 180-second segment estimation is plotted. Bottom profiles are averaged during AQ state. Dash-dot line indicates wave trough level calculated as average of 1/3 lowest wave trough levels from zero-upcrossing.

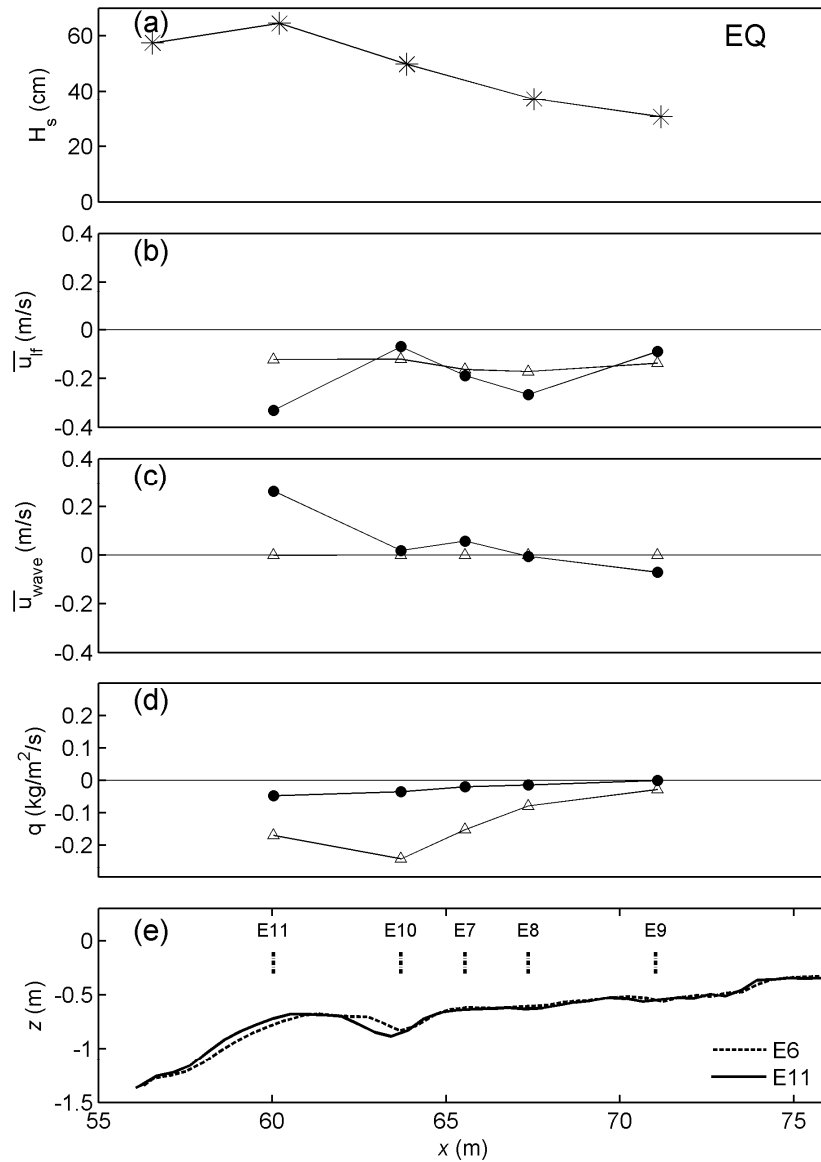


Figure 3.11: Cross-shore distribution of: (a) significant wave height, (b) \bar{u}_{lr} at ADV1 ($\zeta = 1$ cm), (c) \bar{u}_{wave} at ADV1 ($\zeta = 1$ cm), (d) cross-shore sediment flux, and (e) bathymetry and locations of the instrumental array, for EQ. In (b), (c) and (d), closed circle and open triangle represent estimates during intense suspension events and whole time series, respectively.

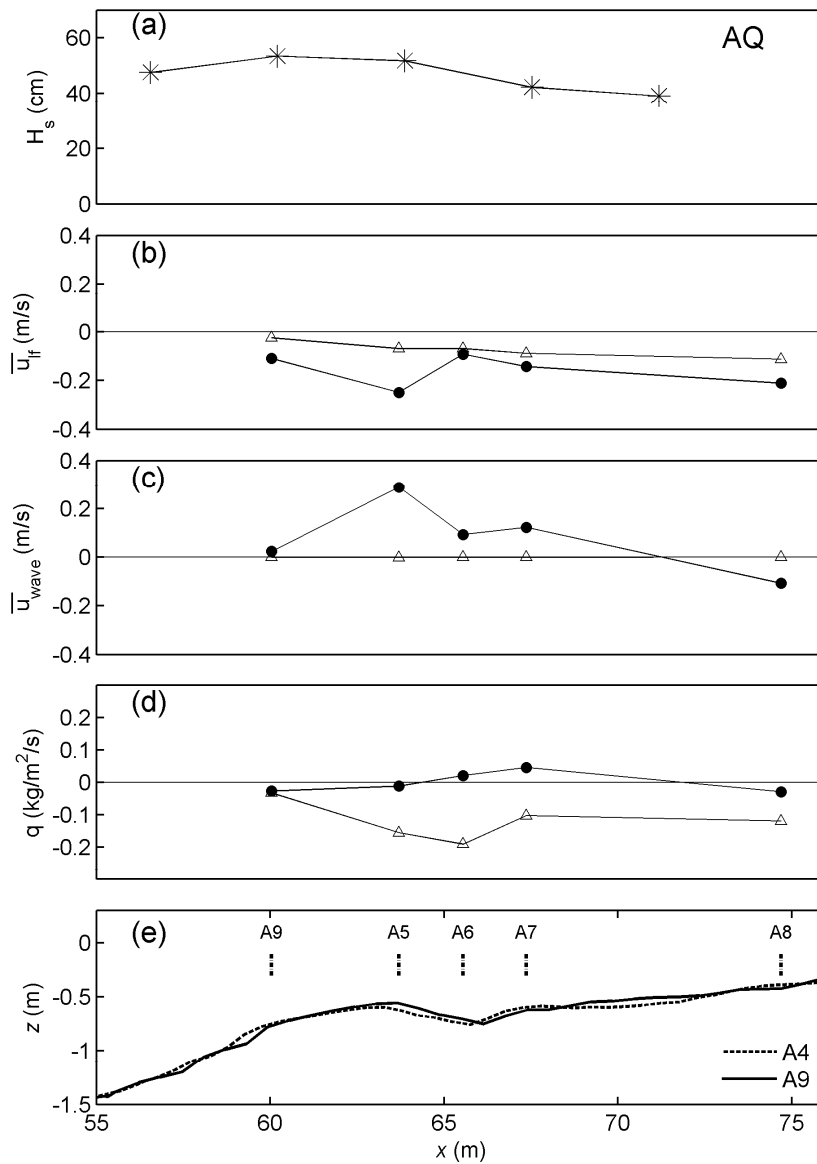


Figure 3.12: Cross-shore distribution of: (a) significant wave height, (b) \bar{u}_{lr} at ADV1 ($\zeta = 1$ cm), (c) \bar{u}_{wave} at ADV1 ($\zeta = 1$ cm), (d) cross-shore sediment flux, and (e) bathymetry and locations of the instrumental array, for AQ. In (b), (c) and (d), closed circle and open triangle represent estimates during intense suspension events and whole time series, respectively.

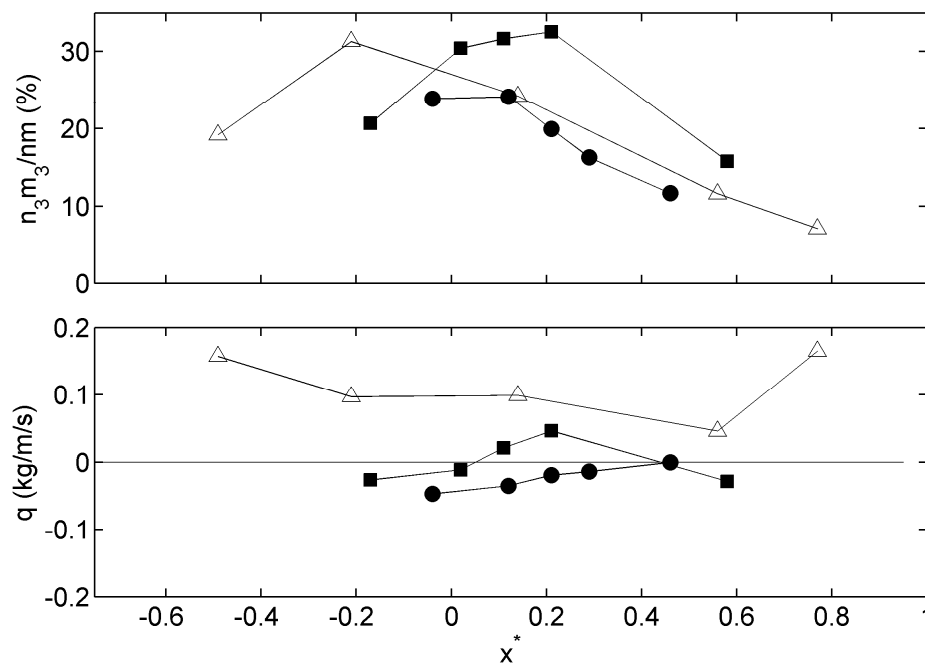


Figure 3.13: (a) Comparison of $(n_3 m_3 / nm)$ of C with sediment concentration at $\zeta = 5$ cm of JS92. (b) Sediment transport by the intense events for EQ, AQ and JS92. Closed circle, closed square, and open triangle represent the intense events for EQ, AQ, and JS92, respectively. x^* denotes normalized cross-shore locations with $x^* = 0$ at bar crest and $x^* = 1$ at shoreline.

Table 3.2: Comparison of intermittency statistics for k and C

Case	Location	k				C			
		Coherent events $m_k + \sigma_k$		Intense events $m_k + 3\sigma_k$		Coherent events $m_C + \sigma_C$		Intense events $m_C + 3\sigma_C$	
		$\frac{n_1}{n}$	$\frac{n_1 m_1}{nm}$	$\frac{n_3}{n}$	$\frac{n_3 m_3}{nm}$	$\frac{n_1}{n}$	$\frac{n_1 m_1}{nm}$	$\frac{n_3}{n}$	$\frac{n_3 m_3}{nm}$
		(%)	(%)	(%)	(%)	(%)	(%)	(%)	(%)
E11	Bar crest	4.8 (-)	40.2 (-)	1.2 (-)	22.2 (-)	6.7 (-)	45.3 (-)	1.9(-)	23.9(-)
E1-E6, E10	Bar trough	8.1 (0.4)	44.8 (1.3)	2.0 (0.1)	21.1 (0.8)	7.6 (1.4)	44.2 (2.3)	2.1 (0.3)	22.7 (2.7)
E7-E9	Inner surf zone	9.0 (0.5)	39.8 (2.5)	1.9 (0.3)	16.0 (1.8)	7.6 (0.3)	32.7 (6.1)	1.9 (0.2)	16.0 (4.1)
A1, A3, A5	Bar crest	5.0 (0.2)	43.4 (0.6)	1.4 (0.1)	24.6 (1.4)	5.9 (1.5)	48.7 (4.5)	2.0 (0.4)	29.8 (2.1)
A2, A4, A6	Bar trough	8.1 (1.1)	44.6 (0.7)	2.0 (0.2)	20.3 (1.4)	6.6 (0.8)	54.8 (2.2)	2.5 (0.3)	34.8 (2.9)
A7, A8	Inner surf zone	8.0 (3.3)	40.3 (3.7)	1.7 (0.7)	17.6 (2.6)	5.3 (2.2)	39.0 (10.0)	1.8 (0.2)	24.2 (11.9)
CK00 (L3)	Transient	10.7 (1.4)	42.8 (2.7)	2.0 (0.2)	14.4 (2.3)	-	-	-	-
CK00 (L4- L6)	Inner surf zone	8.6 (1.6)	41.8 (3.1)	1.9 (0.4)	17.4 (2.2)	-	-	-	-
JS92 (Loc 3,4)	Bar crest	-	-	-	-	16.0 (-)	48.0 (-)	7.5 (-)	34.0 (-)
JS92 (Loc 1,2)	Inner surf zone	-	-	-	-	32.0 (-)	47.0 (-)	10.0 (-)	18.0 (-)

Note: Standard deviation is given in parentheses.

Table 3.3: Coherent event analysis of k and C .

Case	Location	N_k (-)	N_C (-)	N_{kC} (-)	N_{kC} / N_k (%)	N_{kC} / N_C (%)	\bar{u}_{lf} (cm/s)	$(\bar{u}_{lf})_{C-k}$ (cm/s)
E11	Bar crest	75 (-)	18 (-)	7 (-)	9.3 (-)	38.9 (-)	-12.2 (-)	-26.4 (-)
E1-E6, E10	Bar trough	36 (8)	17 (2)	9 (2)	27.3 (7.5)	53.4(11.1)	-13.5 (1.0)	-17.3 (10.4)
E7-E9	Inner surf zone	43 (8)	15 (6)	9 (5)	19.7 (8.0)	57.1 (7.5)	-15.7 (1.8)	-23.5 (1.1)
A1, A3, A5	Bar crest	27 (4)	15 (5)	10 (3)	36.11(12.7)	64.4 (3.9)	-7.6 (0.8)	-18.3 (3.4)
A2, A4, A6	Bar trough	27 (7)	15 (7)	8 (3)	29.9 (13.5)	47.3 (3.2)	-7.7 (0.8)	-4.9 (1.5)
A7, A8	Inner surf zone	44 (23)	13 (6)	9 (8)	17.2 (8.6)	53.5(22.7)	-10.0 (1.7)	-21.7 (8.0)

Note: Standard deviation is given in parentheses.

Chapter 4

**Prediction of time-dependent sediment suspension in the surf zone
using artificial neural network**

Hyun-Doug Yoon

School of Civil and Construction Engineering

Oregon State University, Corvallis, OR 97331-2302, USA

Tel: 541-737-6967 Fax: 541-737-6974 Email: yoonhy@onid.orst.edu

Daniel T. Cox

School of Civil and Construction Engineering

Oregon State University, Corvallis, OR 97331-2302, USA

Munki Kim

Technology Research & Development Institute, Daelim Industrial Co., Ltd.

146-12, Susong-dong, Jongno-gu, Seoul, Korea

Submitted to *Coastal Engineering*

Abstract

A predictive model of time-dependent sediment suspension was developed with artificial neural network, using velocity and integrated sediment concentration (i.e., suspended load) data observed from a large-scale laboratory experiment under erosive and accretive beach conditions. Low-frequency motion, wave-induced motion, and turbulent kinetic energy per unit mass at lower and upper ADV were used as inputs and suspended load near the bed was used as output. To account for the previous history prior to sediment suspension, five time steps (corresponding 2 s) of data prior to sediment suspension were included in the inputs. The artificial neural network model shows a predict capability of the time-dependent sediment suspension in the surf zone for both erosive and accretive conditions. The correlation coefficient (r) between the measured and predicted suspended load reached up to $r = 0.79$ at the bar crest in the accretive beach condition, and typical average correlation coefficients over all subsets (\bar{r}) were 0.53 over the bar crest. The results from various input cases showed that turbulent kinetic energy near the bed is most important to predict the sediment suspension in the surf zone for the both erosive and accretive conditions. Also, the best predictive performance was shown at the bar crest, supporting the hypothesis that turbulence induced by intense wave breaking at the bar crest is a dominant mechanism for sediment suspension. Outside the surf zone (A9), the wave-induced motion was the highest contributing factor for the sediment suspension. Furthermore, when the information from the upper ADV was included as inputs, the model improved the

prediction capability by 40 % at the bar trough in the erosive beach condition. The increased prediction at this location may possibly be attributed to the effect of vertical shear motion in the low-frequency range due to strong undertow from wave breaking.

Keywords: sediment suspension, turbulence, artificial neural network, surf zone, large-scale experiment, nearshore processes

4.1 Introduction

An accurate prediction of local sediment suspension in the surf zone may improve sediment transport and subsequent bathymetric change models because the cross-shore sediment transport is dependent on the phase between sediment suspension and cross-shore velocity (e.g., Hanes, 1988; Jaffe and Sallenger, 1992). However, the sediment suspension in the surf zone shows intense, infrequent and intermittent features (e.g., Hanes and Huntley, 1986; Jaffe and Sallenger, 1992, Yoon and Cox, 2011), and this intermittency makes it difficult to predict the sediment suspension. Furthermore, the mechanisms for sediment suspension are still unclear because of a complex flow field in the surf zone. The traditional parameter for incipient motion of sediments, Shields number, is based on steady flow. Several researches modified the Shields number to apply for the unsteady flow (e.g, van Rijn, 1984, Nielsen, 1998). However, these applications are limited to specific conditions such

as non-breaking oscillating waves although attempts have been made to use this formulation under turbulent flow conditions (e.g., Okayasu et al., 2010).

In the surf zone, the coexistence of low-frequency motions, wave-induced motions, and turbulence induced by wave breaking and their complex interaction with sediments make it even harder to understand the mechanism of sediment suspension. Yoon and Cox (2011) examined the intermittent features of turbulence and sediment suspension in the surf zone and their relationship using data from a large-scale laboratory experiment under prototype and well-controlled conditions. It was found that only 20~35% of the turbulent events were associated with sediment suspension events, implying that much of the intermittent turbulent motion may act to dissipate wave energy rather than suspend sediments. On the other hand, 50~65% of the sediment suspension events were associated with turbulent events, implying that intermittent turbulent motion is one of the fundamental mechanism for the initiation of sediment suspension in the surf zone. In addition to turbulence, low-frequency motion and wave-induced motion can contribute to the sediment suspension as a form of horizontal advection or pressure gradient. These results implied that the prediction of time-dependent sediment suspension is still challenging.

Jaffe and Rubin (1996), hereinafter JR96, developed a nonlinear forecasting model to predict the time-dependent sediment suspension in response to flow velocity in the surf zone. They used data from field observations conducted at the U. S. Army Corps of Engineers Field Research Facility at Duck, North Carolina, in the fall of 1982. The measurement were located seaward of a bar, where water depths ranged from 2.3 to 4.9 m, and significant wave heights ranged from 1.5 to 2.3 m.

Sediment concentration was measured at elevations 10, 13, 19, 31 and 61 cm above the bed with an optical backscatter sensor (OBS), and the fluid velocity was measured at 0.5, 1.0 and 1.75 m above the bed with an electromagnetic current meters sampling at 5 Hz. For the prediction of sediment suspension, they adopted a non-linear prediction model, and provided the correlation coefficient between the measured and predicted sediment concentration at the elevation of 19 cm to estimate the performance of their model, resulting in a correlation coefficient of 0.58 for the best case. Although they used local flow velocity as input, they could not include the effect of turbulence due to the resolution of velocity measurements. As they remarked in the discussion section, their prediction would likely be improved with the information of turbulent intensity.

In this paper, we develop a predictive model for time-dependent sediment suspension in the surf zone, essentially extending the work of JR96 in three ways. First, we adopt the artificial neural network, hereinafter ANN, instead of the

nonlinear regression model. Second, we include turbulence induced by wave breaking, particularly the intermittent nature observed by Cox and Kobayashi (2000) and Yoon and Cox (2011). Third, we apply the model for two data sets with distinct erosive and accretive conditions and at several cross-shore locations including the bar crest, bar trough, and inner surf zone.

ANN is a massively parallel distributed information processor in which the relationship between inputs and outputs is acquired through the learning process resembling human brain (Haykin, 1994), and has been used for function fitting, pattern recognition, clustering, and time series analysis (Hagan, 1996). For example, in coastal engineering and nearshore research, the ANN was applied for estimating the design properties related to coastal structures (e.g., Mase et al., 1995; Panizzo and Briganti, 2007; van Gent et al., 2007), forecasting water level (Tsai and Lee, 1999; Cox et al., 2002), increasing the accuracy of measurements (Kingston et al., 2000), and refining numerical model predictions (Browne et al., 2007). Recently, van Maanen et al. (2010) and Oehler et al. (2011) adopted the ANN to predict the alongshore sediment transport rate and reference concentration, respectively, in a time-averaged sense. Table 4.1 summarizes these recent works with their applications and structural information of their respective ANN models. The structures of the present ANN model will be discussed in Section 4.3. As seen in the applications, the ANN has been mostly used when the ‘cause and effect’ is not clearly understood but the sufficient data is available (van Gent et al., 2007). In

this sense, the prediction of time-dependent sediment suspension, in which the suspension mechanism is still unclear, is the case to apply the ANN model.

As mentioned previously, we use the instantaneous wave breaking induced turbulence as well as the wave-induced and low-frequency motions measured locally as distinct inputs to the model, whereas JR96 used (squared) cross-shore velocity, for the prediction. Because 50~65 % of sediment suspension events were associated with turbulent events in the surf zone (Yoon and Cox, 2011), inclusion of turbulence information will likely improve the prediction of sediment suspension. Furthermore, we use the data from a large-scale laboratory experiment conducted under controlled environment (described in Section 4.2), while JR96 used the field data in which other conditions (e.g., alongshore current, tides, etc.) may affect the sediment suspension.

By using the ANN prediction model, we will investigate the capability for predicting the time-dependent sediment suspension across the surf zone and examine the contribution of each hydrodynamic forcing to sediment response, under two data sets characterized by erosive and accretive nearshore conditions. Recalling that JR96 used the data during a storm passage which may cause an erosive beach condition, the difference between the erosive and accretive beach conditions help us understand the mechanism of sediment suspension for each beach condition.

This paper is organized as follows. In Section 4.2, we introduce a data set from a large-scale laboratory experiment. In Section 4.3, we optimize the ANN structure and explain the procedure for the analysis. In Section 4.4, we provide the results across the surf zone with discussion about the contribution of hydrodynamic forcing to sediment response. Last, in Section 4.5, we summarize the conclusions.

4.2 Data set

Data used in the present analysis were collected during CROSSTEX (CROSS-Shore Sediment Transport Experiment). The experiment was conducted in the large wave flume (104 m long, 3.7 m wide, and 4.6 m deep) at Oregon State University's O H Hinsdale Wave Research Laboratory with approximately 800 m³ of Oregon beach sand ($d_{50}=0.22$ mm) for a natural beach. For the experiment presented here, two wave conditions were synthesized to produce erosive and accretive conditions. Figure 4.1 illustrates the bathymetry, wave conditions, and locations of measurements. For the erosive conditions, the bathymetry transformed from essentially a planar beach to a barred beach under an irregular time series. The observed significant wave heights at the seaward side of the bar crest ranged from 51.8 cm to 59.1 cm and peak periods ranged from 3.97 s to 4.02 s. In approximately 90 minutes the beach was in quasi-equilibrium, in which the bar shape (a ratio of bar height to width) was relatively constant, then the instrument array was moved to five cross-shore locations (Figure 4.1a) for runs E7 to E11

(Yoon and Cox, 2010). For the accretive conditions, the beach transformed from a barred beach to a planar beach, under a new irregular wave time series. The observed significant wave heights at the bar crest ranged from 43.7 cm to 46.0 cm and peak periods ranged from 7.23 s to 7.28 s. In approximately 90 minutes, the beach also reach a quasi-equilibrium condition and the array was moved to five cross-shore locations for runs A5 to A9 (Figure 4.1b). Following Yoon and Cox (2010), we use the notation erosive and quasi-equilibrium (EQ) and accretive and quasi-equilibrium (AQ) for each beach condition.

Simultaneous, high resolution measurements of velocity and sediment concentration were obtained from acoustic Doppler velocimeters (ADV) and fiber-optic backscatter sensors (FOBS). The ADV stack measured the cross-shore velocity (u), alongshore velocity (v), and vertical velocity (w) at six elevations with a sampling rate of 50 Hz. The instrument array was lowered such that the sampling volume of the bottommost ADV was 1.0 cm above the bed at the start of each run. The distances from the bed (ζ) of the ADVs were 1.0 cm (ADV1), 5.0 cm (ADV2), 9.0 cm (ADV3), 20.0 cm (ADV4), 31.0 cm (ADV5), and 50.0 cm (ADV6). In this analysis, the upper and lower ADVs are denote ADV6 ($\zeta = 0.50$ m) and ADV1 ($\zeta = 0.01$ m), respectively, and they are shown in Figure 4.1. At A8, ADV5 was used for the upper ADV because ADV6 was exposed to air above the wave trough level. Eight FOBSs, which were installed from 1.0, 2.0, 3.0, 4.0, 5.0, 6.0, 7.0, and 9.0 cm above the bed, were used to estimate sediment suspension

near bed. The lowest FOBS was located 1.0 cm above the bottom at the start of each run, and the sampling rate was 10 Hz.

Figure 4.2 shows an example of the data for E10 which is an example from EQ measured at bar trough. The measured instantaneous velocity (u) was separated into three components

$$u = u_{lf} + u_{wave} + u' \quad (4.1)$$

where u_{lf} is the low-frequency motion, u_{wave} is the wave-induced motion, and u' is the turbulent fluctuation. Figure 4.2a shows the low-frequency motions at the upper and lower ADVs, which were low-pass filtered with $f / f_p < 0.25$, where f is the frequency and f_p is the peak frequency. We can see that the low-frequency motion is predominantly offshore and the variability of this flow is on the order of several wave periods. In general, the upper and lower sensors are in phase; however, there exist certain instances where strong vertical shear persists for several wave periods (e.g., $460 < t < 480$ s).

Figure 4.2b shows a temporal variation of the wave-induced motion at the lower ADV. The wave-induced motion at the upper ADV is similar with the lower ADV, therefore it is not shown for clarity. The wave-induced motion is estimated by applying Shaw and Trowbridge (2001) method, hereinafter ST01, on the high-pass filtered ($f / f_p > 0.25$) velocity. The basic assumption of the ST01 method is that

coherent signals from a pair of ADVs are regarded as wave-induced motions but incoherent signals are turbulence. The wave-induced motion is calculated as follows (Yoon and Cox, 2011)

$$u_{wave}(t)_{(1)} = \int_{-T/2}^{T/2} h_f(t-\tau) [u(t) - u_{ff}(t)]_{(2)} d\tau \quad (4.2)$$

where, $u_{wave}(t)_{(1)}$ is the time series of wave-induced motion at position (1), $[u(t) - u_{ff}(t)]_{(2)}$ is the high-pass filtered ($f / f_p > 0.25$) velocity at position (2), T is a filter length ($T_p / 2$ are used in this study), and h_f is a least square filter.

Further details of a matrix form for calculation are provided in Yoon and Cox (2010). The wave-induced motion at the lower ADV is estimated by pairing with ADV3 ($\zeta = 0.09$ m), and the upper ADV is paired with ADV5 ($\zeta = 0.31$ m). At some runs (E11, and A9), an error in data acquisition at ADV1 occurred and ADV1 data were replaced with ADV2 for these cases. This replacement has little effect on the result as shown in Yoon and Cox (2011).

Figures 4.2c and 4.2d show temporal variations of turbulent kinetic energy per unit mass (TKE, k) at the upper and lower ADVs, respectively, which are calculated as follows:

$$k = \frac{1}{2} (u'^2 + v'^2 + w'^2) \quad (4.3)$$

where, u' , v' , and w' are turbulent components of cross-shore, alongshore, and vertical fluid velocities, respectively. Each turbulent component was estimated by

subtracting low-frequency motion and wave-induced motion from the measured velocity. The solid thick line in Figure 4.2c shows a moving average using a 2 s filter length. The 2 s filter was used to further smooth the data to provide more robust statistics while at the same time retaining the characteristic intermittent signal. TKE (k) at the lower ADV shows a lower intensity than the upper ADV by a factor of 3. This supports the notion that turbulence is mostly induced near the water surface level due to wave breaking in the surf zone. The wave breaking turbulence is mostly transported to the bed (e.g., $t = 310, 360, 395,$ and 475 s), however, sometimes it is dissipated in the water column and cannot reach to the bed (e.g., $t = 440$ s).

Figure 4.2e shows a temporal variation of the suspended load (C) which is defined as follows

$$C = \sum_0^{h_s} c(\zeta) \Delta\zeta \quad (4.4)$$

where, $c(\zeta)$ is the instantaneous suspended sediment concentration measured at the elevation of ζ , $\Delta\zeta$ is the distance between measurement elevations, h_s is the elevation of top sensor, and C is the suspended load. The suspended load, C , is integrated from the lowest FOBS ($\zeta = 0.01$ m) to the highest FOBS ($\zeta = 0.09$ m). The suspended load provides the intensity of sediment suspension near the bed and also shows a less noisy signal than the sediment concentration at a specific elevation. From this figure, the most significant sediment suspension occurs at

$t=365$ s, and there is a significant turbulence event that precedes the suspension event. However, one can see a large turbulent event near $t=395$ s without corresponding suspension event. Furthermore, another large suspension event is observed near $t=325$ s without significant turbulence events. These observations highlight the difficulty in predicting the time-dependent sediment suspension in the surf zone. In any case, the data presented in Figures 4.2a through 4.2d essentially provide the forcing for the model, and Figure 4.2e is the response. Data observed at other locations exhibited similar behavior, showing similar intermittent features in turbulence and suspended load despite the different mean values across the surf zone (Yoon and Cox, 2011).

4.3 Artificial neural network model

4.3.1 General configuration of ANN structure

Figure 4.3 shows the configuration of the ANN model used here. The two-layer feed forward ANN architecture is used with one hidden layer and one output layer. Most of studies adopted one hidden layer (Table 4.1) for simplicity because a higher number of hidden layers do not improve the performance in most cases. The input layer consists of the various combinations of u_{lf} , u_{wave} , and k from the lower and upper ADVs and the output layer consists of the suspended load. Table 4.2 lists the cases of input combinations, categorizing into 4 groups: measured velocity (Group 1, Case 1) from the lower ADV down-sampled to 2 Hz, one input

parameter (Group 2, Case 2-4) from the lower ADV, two or three input parameters (Group 3, Case 5-8) from the lower ADV, and five input parameters including the upper ADV in addition to the lower ADV (Group 4, Case 9-11). To account for the time history of input data, five previous time steps (2 s prior to suspended load) of each input parameter are used, including the data ahead of a quarter of significant wave period for the erosive ($T_p/4=1.0$ s) and accretive ($T_p/4=1.7$ s) case. We note that JR96 found that the data prior to a quarter of the significant wave period contributed to the sediment suspension. These input data were scaled in the range of -1 and 1, and were transferred to the neurons in the hidden layer with a transfer (tansig) function as is typical for ANN modeling (e.g., Panizzo and Briganti, 2007).

The ANN results are dependent on the number of neurons in the hidden layers. To optimize the number of neurons in the hidden layer, we tested the sensitivity for different number of neurons (from 1 to 10) in the hidden layer. We found that the number of neurons from 2 to 10 showed similar performance within the range of 10%, while one neuron showed less stable results for each case. For simplicity we adopted 2 neurons in the hidden layer in the present study.

Input data and the neurons in the hidden layer are interconnected with weights and bias. Then, the information in the hidden layer is transferred to the output layer with another transfer function. These relations can be expressed as (Hagan et al., 1996)

$$\mathbf{n} = f(\mathbf{W}\mathbf{p} + \mathbf{b}) \quad (4.5)$$

where \mathbf{n} is the net input vector, f is a transfer function, \mathbf{W} is the weight matrix, and \mathbf{b} is the bias vector. The superscripts 1 and 2 indicate the hidden layer and output, respectively. The subscripts in Figure 4.3 indicate the number of inputs (R), the neurons in the hidden layer (2) and output (1). Also the transfer function of the hidden layer (f^1 , tansig) and output (f^2 , linear) are expressed as

$$\mathbf{a}^1 = f^1(\mathbf{n}^1) = \frac{e^{\mathbf{n}^1} - e^{-\mathbf{n}^1}}{e^{\mathbf{n}^1} + e^{-\mathbf{n}^1}} \quad (4.6)$$

$$a^2 = f^2(n^2) = n^2 \quad (4.7)$$

where \mathbf{a} is the output vector. The output, which was scaled between -1 and 1, were rescaled back to the original dimension in the end.

4.3.2 ANN Training

The biases and connection weights are evaluated with a back-propagation algorithm (Levenberg-Marquardt), which is the fastest method for training modern-sized feedforward ANN and performs well on function fitting problems (Hagan et al., 1996). From the data set, the first 100 s data were eliminated due to possible transient effects associated with the start of the wavemaker, and the analysis was performed on the remaining 800 s data. The 800 s input and output data were partitioned into a 400 s training data set, a 200 s validation set, and a 200 s prediction set. The tests were repeated by changing the training, validation, and prediction sets in the whole data set following the so-called ‘bootstrapping’

technique used by others (e.g., van Gent et al., 2007; Oehler et al., 2010). Table 4.2 provides details of the subsets classification. On the other hand, to avoid overfitting in which the noise in the training set is also learned due to too many training, the mean square error (MSE) in validation set is monitored concurrently during the training. The training stopped if the MSE in the validation set increased for 6 consecutive epochs.

4.3.3 Procedures

Because the back-propagation ANN is sensitive to the initial weights and biases, it is important to find a proper initial weights and biases for the prediction.

Following the procedure by Oehler et al. (2011), the ANN was initialized with random weights and bias 22 times. Out of 22 observations, the weight and bias of the best case (which has a minimum MSE error) in the training and validation set were kept, and they were applied for the prediction set. This approach accounts for the 10% best cases with a confidence of 90%, assuming that random initial weights and biases follow a normal distribution (Oehler et al., 2011).

To find the minimum number of repetitions necessary for stable performance, a sensitivity test for the number of runs was carried out. Figure 4.4 shows the standard deviation of the correlation coefficient between predicted and measured suspended load (σ_r) as a proxy of the stability of performance. This figure shows that the statistics become stable when the procedure was repeated at least 100

times. In this sense, we will provide the average of 100 repetitions for the prediction performance. We note that the ANN model was written using the MATLAB (Neural Network Toolbox, version 7.9).

4. 4 Results and discussion

Figure 4.5 shows an example application to E10 for Case 11 and Subset 5. The ANN was satisfactorily trained in the training set (Figure 4.5e, $500 < t \leq 900$ s), and monitored in the validation set to avoid overfitting (Figure 4.5e, $100 < t \leq 300$ s). The prediction set (Figure 4.5e, $300 < t \leq 500$ s) is highlighted in Figure 4.6. As a first step to examine the performance of the ANN model, we compared the time-averaged and the root-mean-squared of C . The time-average of the predicted C is 0.22 kg/m^2 and was similar to the measured C of 0.20 kg/m^2 , which is somewhat expected since the wavemaker forcing was held constant. Also the root-mean-squared of C is 0.36 kg/m^2 for the prediction and 0.33 kg/m^2 for the measurement.

The model performance was evaluated more closely with a correlation coefficient, r , between the measured and predicted C in the prediction set. Although van Maanen et al. (2010) remarked that the ANN is sometimes difficult to train and predict for extreme values, such as intermittent suspension events, our results show a fairly good predictive capability ($r = 0.70$). This is shown in Figure 4.6, in which the ANN model predict the relatively weak suspension event at $t = 335$ s and the more intense event at $t = 370$ s. There is a slight shift between the measured and

predicted C and can also be seen at $t = 480$ s. The model fails to predict two moderate events ($t = 325, 430$ s) and significantly overpredicts a small event at $t = 305$ s.

Figure 4.7 shows the average correlation coefficient, \bar{r} , at the five cross-shore locations for EQ, including a bar crest (E11), trough (E10) and inner surf zone (E7, E8, E9). To provide a robust statistics results, the averages of all subsets from the bootstrapping trials were provided. It should be noted that the maximum of the 6 subsets is larger than the average of the all subsets by approximately 50~100%, except for far inner surf zone (A8) and outside the surf zone (A9). For instance, the maximum for Group 1 at E11 was $r = 0.72$, but the average for 6 subsets was $\bar{r} = 0.49$. Figure 4.7a shows the performance of the ANN when the measured velocity was used as input (Case 1 of Group 1 in Table 4.2). Seaward of the bar at E11 where the turbulence from wave breaking is low, the correlation is higher, $\bar{r} = 0.49$. This result indicates that the wave-induced and low frequency velocity motion can give a reasonable estimate for sediment suspension. However, it shows a poor performance at the bar trough and inner surf zone, showing \bar{r} from 0.0 to 0.1.

Figure 4.7b shows the performance of the ANN for Group 2 when only one parameter among the low-frequency motion (Case 4), wave-induced motion (Case 3), or TKE was considered (Case 2). For the input case with TKE (Case2), \bar{r}

ranges 0.35 to 0.50, being larger than the case with the low-frequency motion or wave-induced motion by a factor of 3. Figure 4.7c for Group 3 shows the performance of the ANN when two or three components were used. Case 5, which consists of the low-frequency motion and wave-induced motion, shows a lowest correlation coefficient, confirming that TKE is the most important information to predict sediment suspension in the surf zone. The other cases in Group 3 (Case 6, 7, and 8) show similar results each other for all locations. Figure 4.7d shows the performance of the ANN for Group 4 when the data from the upper sensor were provided in addition to the lower ADV. Interestingly, the largest increase of the average correlation coefficient is found at the bar trough, when the low-frequency motion from the upper sensor were considered. For example, \bar{r} for Case 11 (in Figure 4.7d) is enhanced by approximately 40% compared to Case 8 (in Figure 4.7c). We speculate that the increased prediction at this location with the low-frequency motion from upper sensor can be attributed to the coherent structures over the complex bathymetry at the bar trough. As remarked in Section 4.2 (e.g., $460 < t < 480$ s in Figure 4.2), the ‘shear motion’ in the low frequency motion, which probably results from return currents induced by wave breaking, may be an explanation.

Figure 4.8 shows the average correlation coefficient at the five cross-shore locations for AQ, including outside the surf zone (A9), a bar crest (A5), trough (A6) and inner surf zone (A7, A8). Similar to EQ, Figure 4.8a shows

unsatisfactory results when the measure velocity itself was used in the surf zone. Figure 4.8b shows a significant \bar{r} at the bar crest and trough, ranging 0.45 to 0.50. Again, it was found that TKE is the most contributing factor to predict sediment suspension near the bar region where is the most dynamic suspension events occur. The highest \bar{r} values occur at the bar crest for both EQ (E11, $\bar{r}=0.52$) and AQ (A5, $\bar{r}=0.54$). This implies intermittent turbulent motion is one of the fundamental mechanism for the initiation of sediment suspension, especially at the bar crest where the effect of wave breaking is maximized. Outside the surf zone (A9), wave-induced motion (Case 3) is more decisive than TKE (Case 2) for sediment suspension.

In Figure 4.8c, it is confirmed that turbulence is also the important factor for sediment suspension in AQ. For Subset 1 and Case 8, the maximum correlation coefficient was found 0.79 at the bar crest (not shown). Comparing with the best result (correlation coefficient of 0.58) of the nonlinear model by Jaffe and Rubin (1996), the present study improved the prediction capability in the surf zone, using the ANN model with decomposed flow velocity as inputs. Figure 4.8d shows that the information from upper sensor did not improve the prediction capability significantly at the bar trough, in contrast to EQ. This is probably due to weaker undertow in AQ than EQ. In any event, we anticipate that there can be several refinements and future work to this model. For example, we used only the local velocity information to predict the locally observed sediment suspension. However,

the advection of sediment in the surf zone is another possible explanation for the intermittent suspended sediment observations, therefore the model could be extended to include wave-induced and low frequency velocity information from sensors landward and seaward of the prediction location. We also anticipate that other mechanisms such as strong pressure gradients, particularly over the bar in the presences of steep waves, can cause a momentary failure of the seabed (Madsen, 1974) and could be another mechanism to suspend sediments. In this case, it would be necessary to use a different input such as free surface slope or near bottom pressure gradient (e.g., Suzuki et al., 2010).

4. 5 Conclusions

We developed an artificial neural network model to predict the time-dependent sediment suspension in the surf zone. The measure velocity was decomposed into the low-frequency motion, wave-induced motion, and turbulent kinetic energy per unit mass and they were used as inputs with 11 combinations. The model was applied to two sets of large-scale laboratory tests for irregular waves over a moveable bed for erosive and accretive conditions. The average correlation coefficient between the measured and predicted suspended load were calculated to estimate the performance of the ANN model across the surf zone. The main conclusions supported by this work include:

- (1) This study shows an improved sediment prediction (with correlation coefficient up to 0.79) using the ANN model with turbulence information in the surf zone, comparing with the best result (correlation coefficient of 0.58) of the nonlinear model by Jaffe and Rubin (1996).
- (2) Turbulent kinetic energy near the bed is important to predict the sediment suspension in the surf zone for both erosive and accretive conditions. When turbulent kinetic energy was considered as an input, the correlation coefficient between the measured and predicted sediment suspension increases by a factor of 3, compared with the case where only the low-frequency motion or wave-induced motion was used as an input.
- (3) The best predictions are shown at the bar crest (E11 and A5) with average correlation coefficients of $\bar{r} = 0.52$ and 0.54, respectively. These results represent the importance of turbulence from the intense wave breaking at the bar crest for sediment suspension.
- (4) Outside the surf zone (A9), the wave-induced motion was the highest contributing factor for the sediment suspension.
- (5) When the information from the upper ADV was included as input, the ANN model improved the prediction capability by 40 % at the bar trough for the erosive case while it did not improve the prediction in accretive case.

Acknowledgements

This work was supported by the National Science Foundation (OCE-0351741). The authors are grateful to all participants during the CROSSTEX project and the staff at the O. H. Hinsdale Wave Research Laboratory. The authors thank A. Ogston, University of Washington, for the loan of the FOBS during the CROSSTEX deployment. Munki Kim was supported by Brain Korea 21 for his stay at Oregon State University. Dan Cox was supported by the Japan Society for the Promotion of Science during the preparation of this manuscript. The authors thank David Rubin for valuable discussion on forecasting sediment suspension in the surf zone.

References

- Browne, M., B. Castelle, D. Strauss, R. Tomlinson, M. Blumenstein, and C. Lane, 2007, Near-shore swell estimation from a global wind-wave model: Spectral process, linear and artificial neural network models, *Coastal Eng.*, 54, 445-460.
- Cox, D.T., P. Tissot, and P. Michaud, 2002, Water level observations and short-term predictions including meteorological events for entrance of Galveston bay, Texas, *J. waterway, Port, Coastal and Ocean Engineering.*, 128, 21-29.
- Hanes, D., M. and D. A. Huntley, 1986. Continuous measurements of suspended sand concentration in a wave dominated nearshore environment, *Continental Shelf Research*, 6, 585-596.

- Hanes, D., M., 1988, Intermittent sediment suspension and its implications to sand tracer dispersal in wave-dominated environments, *Marine Geology*, 81, 175-183.
- Hagan, M.T., H.B. Demuth, and M. Beale, 1996, *Neural network design*. PWS Publishing, Boston, Massachusetts. 736 pp.
- Haykin, 1994, *Neural networks: A comprehensive foundation*, Macmillan College Publishing, Englewood Cliffs, New Jersey, 696 pp.
- Jaffe, B. E., R. W. Sternberg, and A. H. Sallenger Jr., 1984, The role of suspended sediment in shore-normal beach profile changes, *Proceedings of the 19th International Coastal Engineering Conference*, 2, 1983-1996, Am. Soc. Civil. Eng., New York
- Jaffe, B. E., and A. H. Sallenger Jr., 1992, The contribution of suspension events to sediment transport in the surf zone, *Proceedings of the 23rd International Coastal Engineering Conference*, 3, 2690-2693, Am. Soc. Civil. Eng., New York.
- Jaffe, B. E., and D.M. Rubin, 1996, Using nonlinear forecasting to learn the magnitude and phasing of time-varying sediment suspension in the surf zone, *J. Geophys. Res.*, 101, C6, 14,283-14,296.
- Kingston, K. S., B.G. Ruessink, I. M. J. van Enckevort, and M. A. Davidson, 2000, Artificial neural network correction of remotely sensed sandbar location, *Marine Geology*, 169, 137-160.

- Madsen, O. S., 1974., Stability of a sand bed under breaking waves, *Proceedings of the 14th International Conference on Coastal Engineering*. 776-794. Am. Soc. Civil. Eng., New York
- Mase, H., M. Sakamoto, and T. Sakai, 1995, Neural network for stability analysis of rubble-mound breakwaters, *J. waterway, Port, Coastal and Ocean Engineering.*, 121, 294-299.
- Nielsen, 1998, *Coastal bottom boundary layers and sediment transport*, World Scientific Publishing, Singapore, 324 pp.
- Oehler, F., G. Coco, M.O. Green, and K.R. Bryan, 2011, A data-driven approach to predict suspended-sediment reference concentration under non-breaking waves, *Continental Shelf Research*, doi:10.1016/j.csr.2011.01.015.
- Okayasu, A., K. Fujii, and M. Isobe, 2010, Effect of external turbulence on sediment pickup rate, *Proceedings of the 32nd International Coastal Engineering Conference*, <https://journals.tdl.org/ICCE/article/view/1434>, Am. Soc. Civil. Eng., New York.
- Panizzo, A., and R. Briganti, 2007, Analysis of wave transmission behind low-crested breakwaters using neural networks, *Coastal Eng.*, 54, 643-656.
- Shaw, W. J., and J. Trowbridge. 2001. The direct estimation of near-bottom turbulent fluxes in the presence of energetic wave motions, *J. Atmos. Oceanic Technol.*, 18, 1540-1557.

- Suzuki, T., S. Shin, D. T. Cox, and N. Mori, 2010, Spatiotemporal characteristics of near-bed pressure gradient on a barred beach, *J. waterway, Port, Coastal and Ocean Engineering.*, 136, 327-336.
- Tsai, C. P., and T. Lee, 1999, Back-propagation neural network in tidal-level forecasting, *J. waterway, Port, Coastal and Ocean Engineering.*, 125, 195-202.
- van Gent, M.R.A., H.F.P. van den Boogaard, B. Pozueta, and J.R. Medina, 2007, Neural network modeling of wave overtopping at coastal structures, *Coastal Eng.*, 54, 586-593.
- van Maanen, B., G. Coco, K.R. Bryan, and B.G. Ruessink, 2010, The use of artificial neural networks to analyze and predict alongshore sediment transport, *Nonlin.Processes Geophys.*, 17, 395-404.
- van Rijn, 1984, Sediment pickup functions, *Journal of Hydraulic Eng.*, 110, 1494-1502.
- Yoon, H.-D, and D. T. Cox, 2010, Large-scale laboratory observations of wave breaking turbulence over an evolving beach, *J. Geophys. Res.*, 115 ,C10007, Doi:10.1029/2009JC005748.
- Yoon, H.-D, and D. T. Cox, 2011, Cross-shore variation of intermittent sediment suspension and turbulence induced by depth-limited wave breaking, submitted to *Continental Shelf Research*.

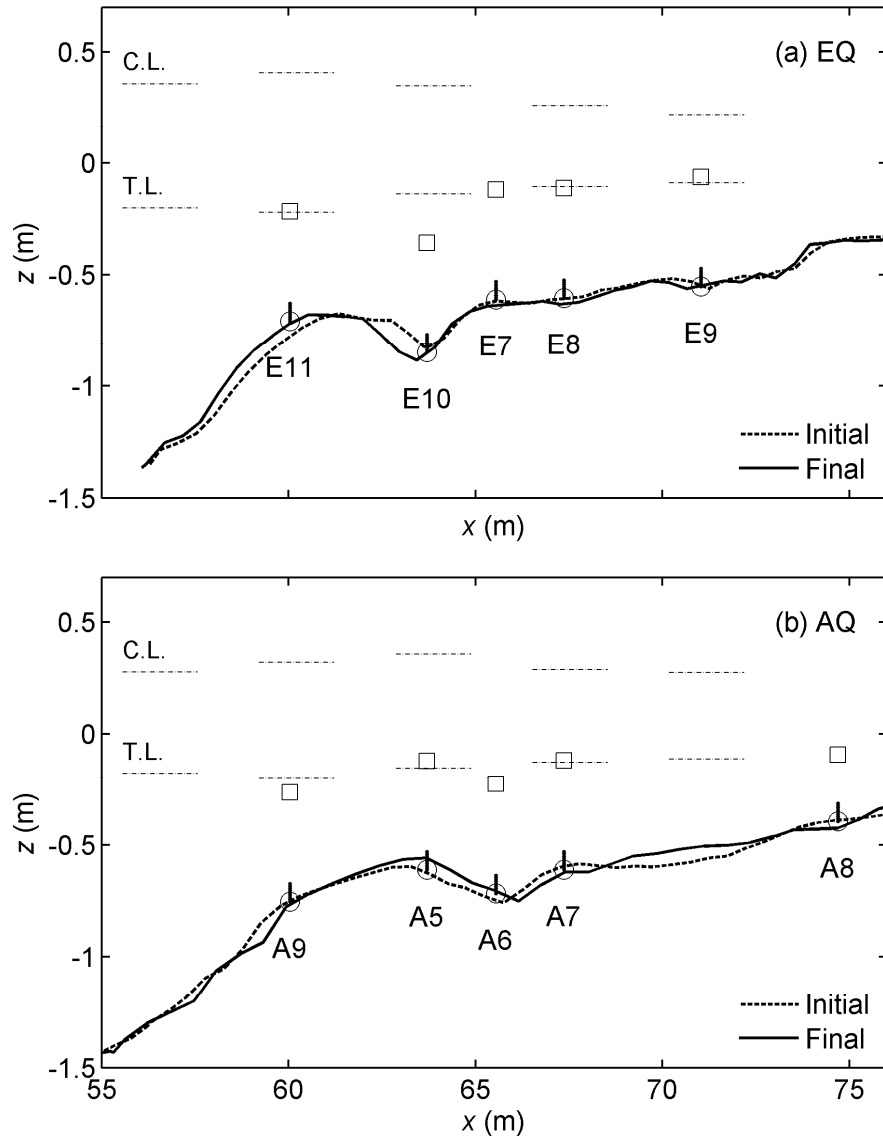


Figure 4.1: Bathymetry and locations of measurements for: (a) erosive and quasi-equilibrium (EQ) and (b) accretive and quasi-equilibrium (AQ). Open circle and square represents lower ADV (ADV1, $\zeta = 0.01$ m), and upper ADV (ADV6, $\zeta = 0.50$ m), respectively. At A8, ADV5 ($\zeta = 0.31$ m) is replaced for upper ADV. Vertical lines near bed indicates the range of FOBS from $\zeta = 0.01$ to 0.09 m. Horizontal dash-dot lines represent wave crest and trough level calculated as average of 1/3 highest and lowest water surface levels from zero-upcrossing.

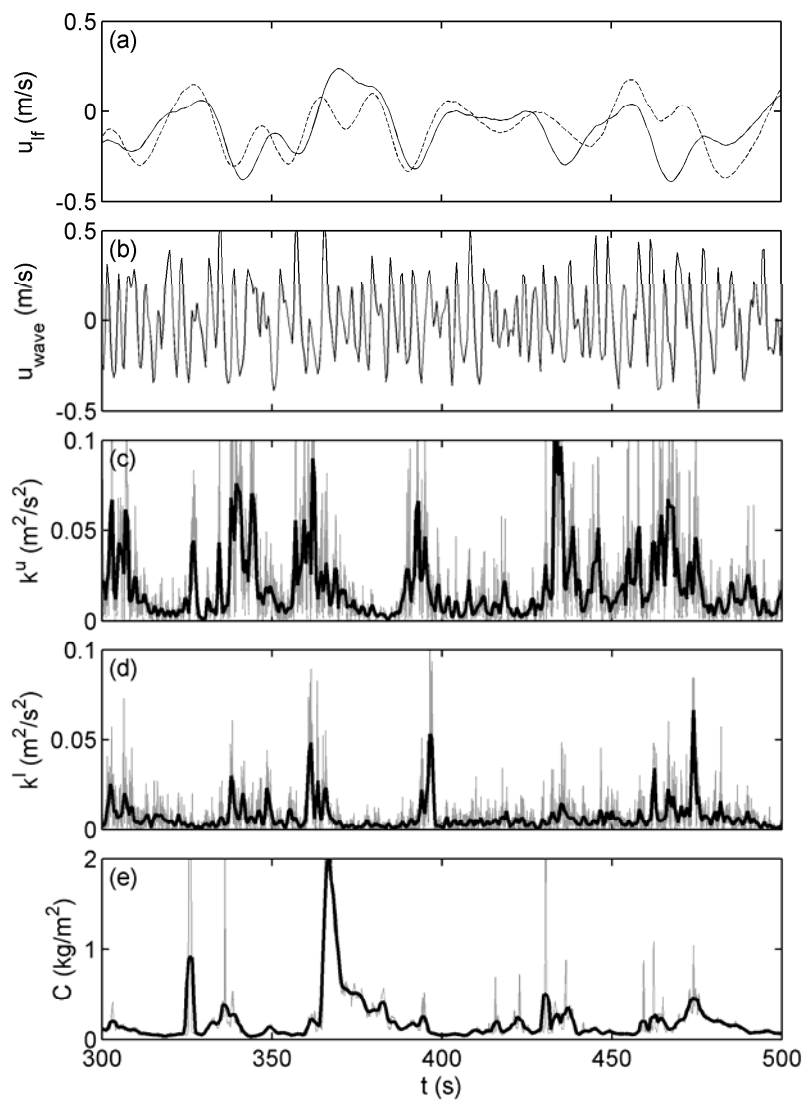


Figure 4.2: Example of inputs (a-d) and output (e) for E10: (a) cross-shore velocity of low-frequency motion at lower ADV (ADV1, $\zeta = 0.01$ m, solid line) and upper ADV (ADV6, $\zeta = 0.50$ m, dashed line), (b) cross-shore velocity of low-frequency motion at lower ADV, (c) turbulent kinetic energy per unit mass (k) at upper ADV, (d) turbulent kinetic energy per unit mass (k) at lower ADV, and (e) suspended load (C). In (c), (d), and (e), gray and black lines indicate raw and smoothed (with 2 s filter averaging) data, respectively.

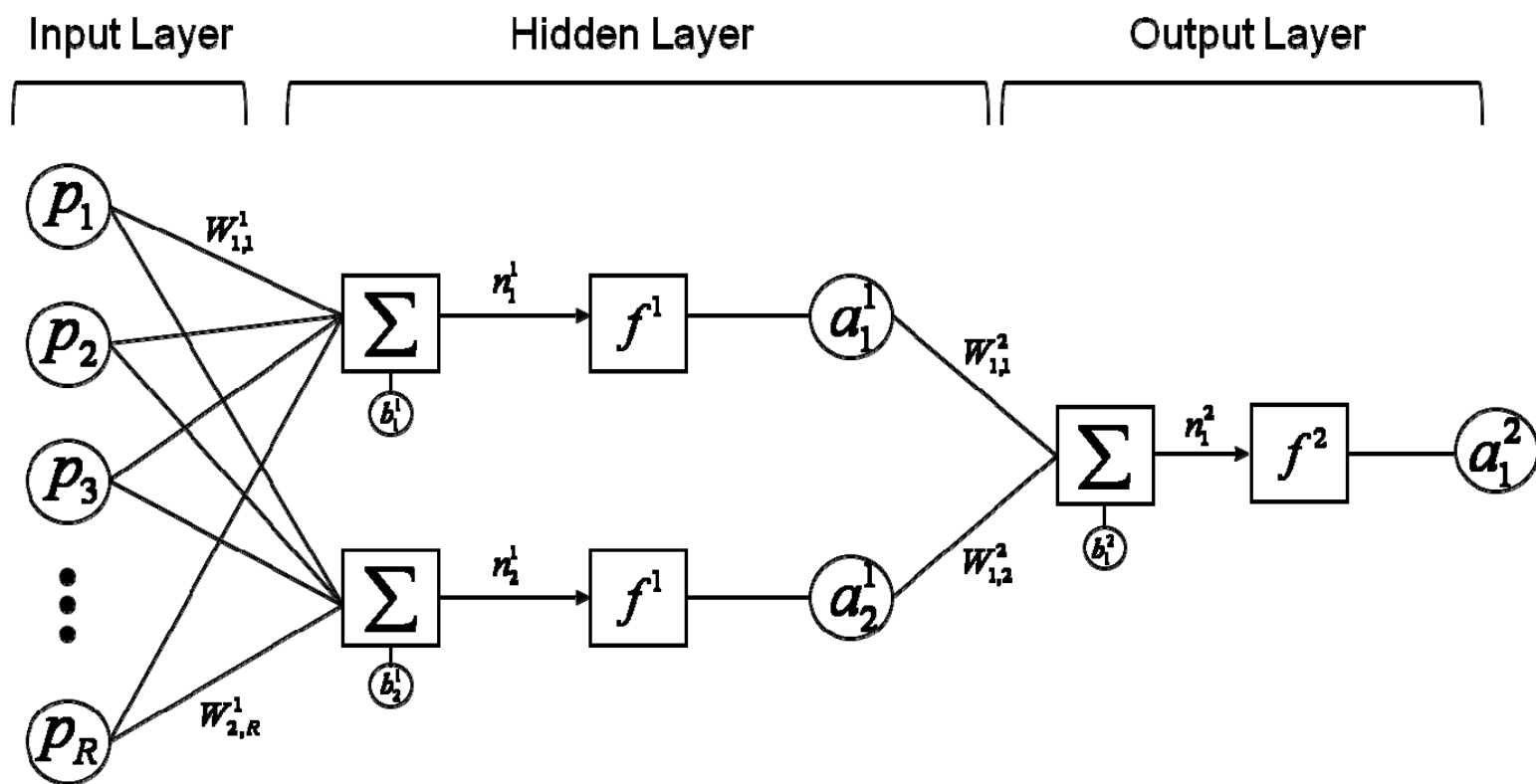


Figure 4.3: Sketch of ANN structure

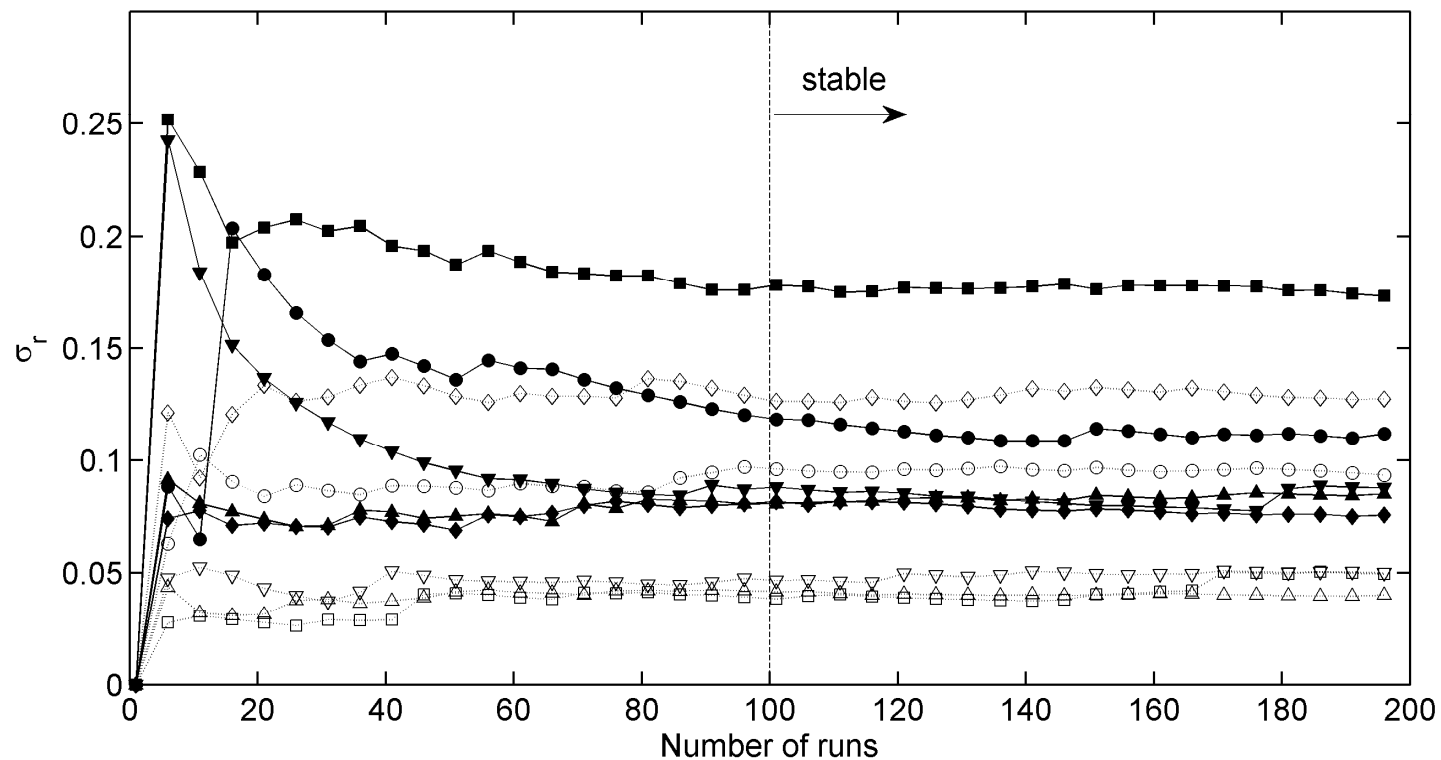


Figure 4.4: Standard deviation of correlation coefficient (σ_r) with number of runs. Input case 8 and Subset 5 is used for the training, validation, and prediction. Closed symbols represent EQ: circle (E7), square (E8), diamond (E9), upward triangle (E10), and downward triangle (E11). Open symbols represent AQ: circle (A5), square (A6), diamond (A7), upward triangle (A8), and downward triangle (A9).

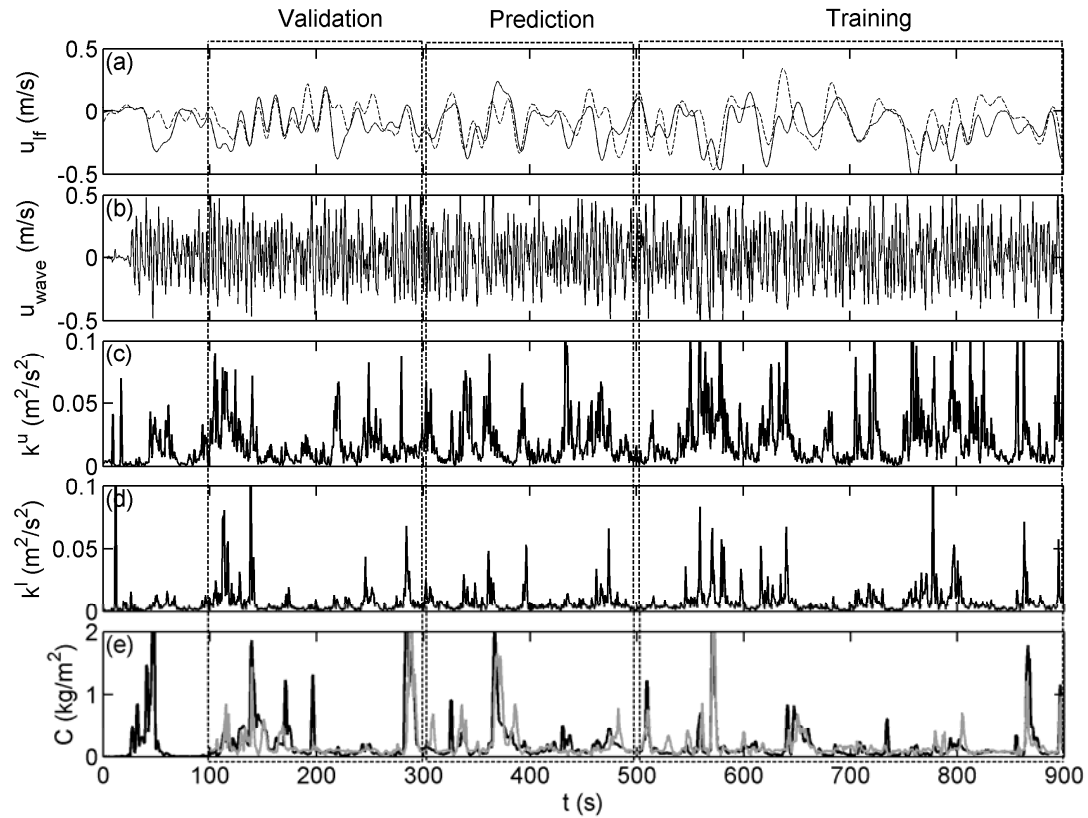


Figure 4.5: Example of inputs (a-d) and output (e) for E10 for input case 11 and subset 5: (a) cross-shore velocity of low-frequency motion at lower ADV (ADV1, $\zeta = 0.01$ m, solid line) and upper ADV (ADV6, $\zeta = 0.50$ m, dashed line), (b) cross-shore velocity of low-frequency motion at lower ADV, (c) turbulent kinetic energy per unit mass (k) at upper ADV, (d) turbulent kinetic energy per unit mass (k) at lower ADV, and (e) measured (black) and predicted (gray) suspended load. In (c), (d), and (e), the smoothed lines (moving averaged with 2 s filter) are shown.

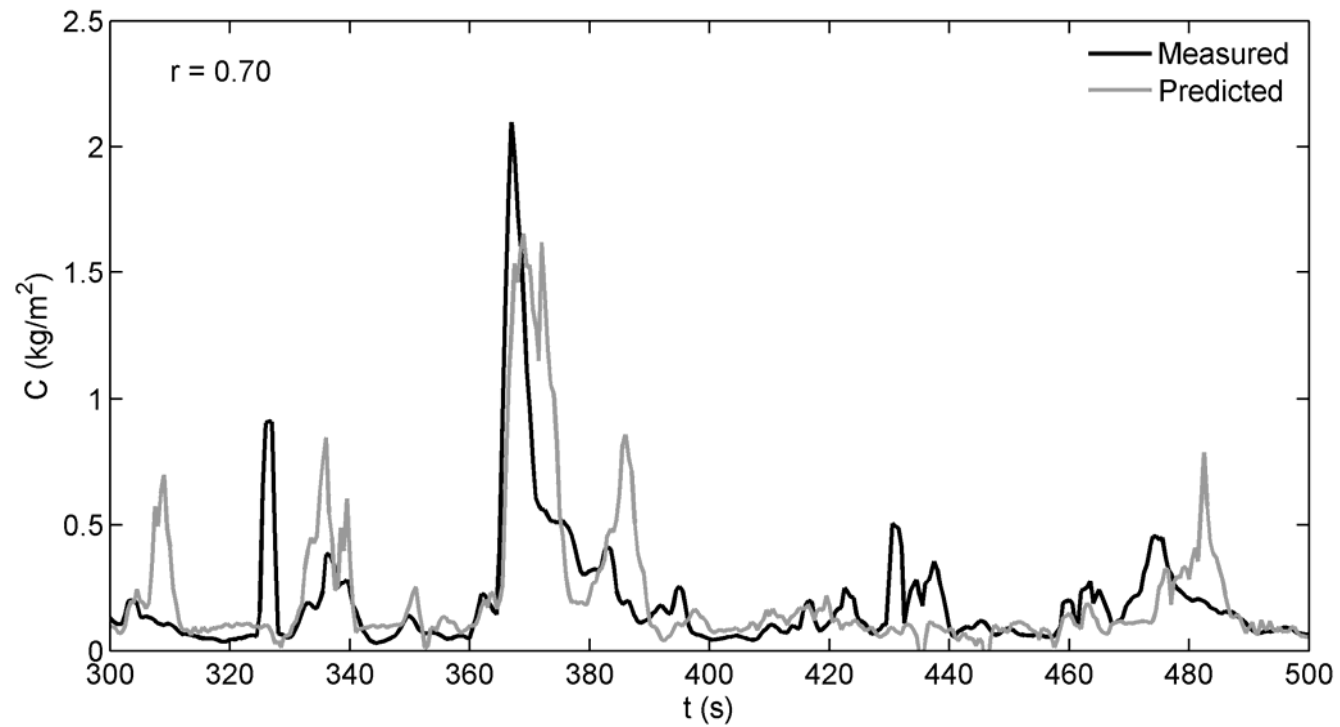


Figure 4.6: Time series of observed suspended load (black) and predicted suspended load (gray) for E10, in the range of $300 \text{ s} < t < 500 \text{ s}$. Input case 11 and Subset 5 is used for the training, validation, and prediction. Correlation coefficient between the observed and predicted suspended load is provided in upper left.

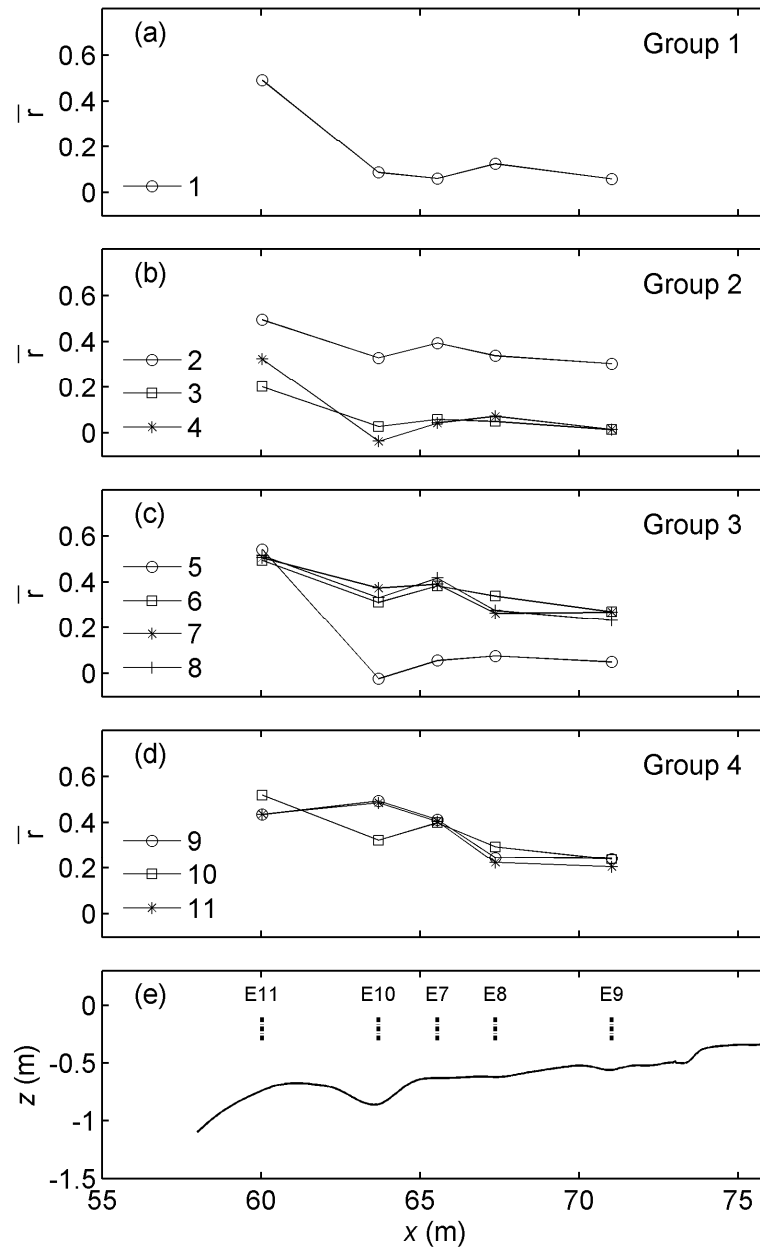


Figure 4.7: Cross-shore variation of the average of correlation coefficients over all subsets, for EQ: (a) Group 1 (Case 1), (b) Group 2 (Case 2-4), (c) Group 3 (Case 5-8), (d) Group 4 (Case 9-11), and (e) averaged bathymetry over EQ. Legends indicate input case number.

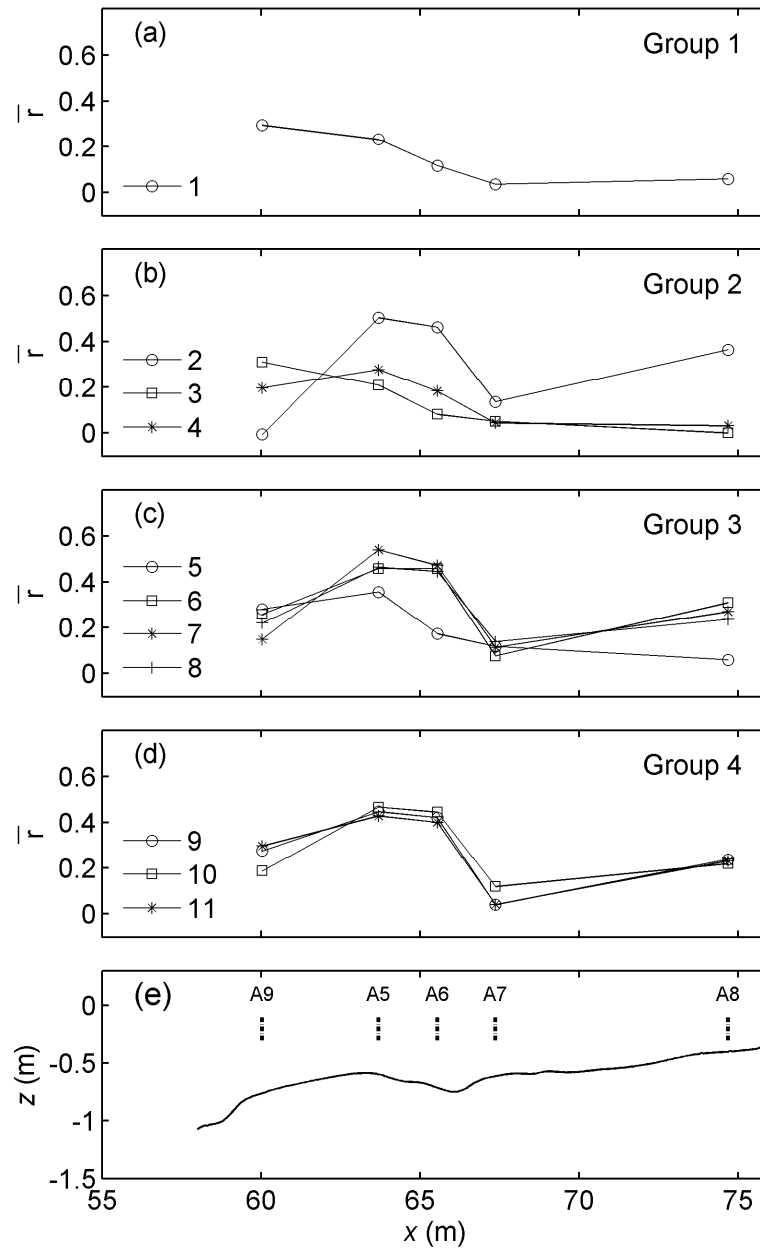


Figure 4.8: Cross-shore variation of the average of correlation coefficients over all subsets, for AQ: (a) Group 1 (Case 1), (b) Group 2 (Case 2-4), (c) Group 3 (Case 5-8), (d) Group 4 (Case 9-11), and (e) averaged bathymetry over AQ. Legends indicate input case number.

Table 4.1: Summary of literatures using artificial neural network in coastal and nearshore research

Paper	Application	Input	No. of hidden layer	No. of neuron	Transfer function	Train function	Output
Mase et al. (1995)	Stability analysis of rubble-mound breakwaters	damage level, number of waves, permeability parameter, surf similarity, relative water depth, spectral parameter	1	12	logsig	GD ¹	Stability number
Tsai and Lee (1999)	Tidal-level forecasting	advance consecutive tidal data, corresponding shock	1	4	logsig	GD	Tidal level
Kingston et al. (2000)	Improving the accuracy of sand bar location	wave height, tidal level	1	15	tansig	LM ²	Bar location
Cox et al. (2002)	Prediction of water level	previous measurements of water level, wind speed, barometric pressure	1	1	logsig, tansig	LM	Water level anomaly
Panizzo and Briganti (2007)	Prediction of wave transmission behind low-crested breakwaters	incident wave height, water depth, offshore wave length, 6 structural parameters	1	6	tansig, linear	LM	Transmission coefficient
van Gent et al. (2007)	Prediction of wave overtopping discharges for coastal structures	significant wave height, wave period, wave angle, 12 geometrical shape parameters	1	20	Not provided	GD	Overtopping discharge
Browne et al. (2007)	Prediction of wave height	wave height, swell, wind, wind waves, directional angle variables	1	6	tansig	LM	Significant wave height
van Maanen et al. (2010)	Prediction of alongshore sediment transport rate	water depth, wave height, wave period, alongshore velocity	1	2-8	logsig	LM	Alongshore suspended sediment rate
Oehler et al. (2011)	Prediction of reference concentration under non-breaking waves	water depth, mean grain size, wave amplitude at the bed, mean wave period	1	3	logsig	GD	Reference concentration
Yoon et al. (This study)	Prediction of time-dependent sediment suspension in the surf zone	low-frequency motion, wave-induced motion, turbulent kinetic energy from upper and lower ADV	1	2	tansig, linear	LM	Suspended load

Note: ¹GD (Gradient descent), ²LM (Levenberg-Marquardt)

Table 4.2: Case of input data

Case	Group	ADV1 (Lower)				ADV6 (Upper)		
		u	u_{lf}	u_{wave}	k	u_{lf}	u_{wave}	k
1	1	●	○	○	○	○	○	○
2	2	○	○	○	●	○	○	○
3	2	○	○	●	○	○	○	○
4	2	○	●	○	○	○	○	○
5	3	○	●	●	○	○	○	○
6	3	○	○	●	●	○	○	○
7	3	○	●	○	●	○	○	○
8	3	○	●	●	●	○	○	○
9	4	○	●	●	●	●	○	○
10	4	○	●	●	●	○	○	●
11	4	○	●	●	●	●	○	●

Table 4.3: Subset for training, validation and prediction.

Subset	Training	Validation	Prediction
1	$100 \text{ s} < t \leq 500 \text{ s}$	$500 \text{ s} < t \leq 700 \text{ s}$	$700 \text{ s} < t \leq 900 \text{ s}$
2	$100 \text{ s} < t \leq 500 \text{ s}$	$700 \text{ s} < t \leq 900 \text{ s}$	$500 \text{ s} < t \leq 700 \text{ s}$
3	$300 \text{ s} < t \leq 700 \text{ s}$	$700 \text{ s} < t \leq 900 \text{ s}$	$100 \text{ s} < t \leq 300 \text{ s}$
4	$300 \text{ s} < t \leq 700 \text{ s}$	$100 \text{ s} < t \leq 300 \text{ s}$	$700 \text{ s} < t \leq 900 \text{ s}$
5	$500 \text{ s} < t \leq 900 \text{ s}$	$100 \text{ s} < t \leq 300 \text{ s}$	$300 \text{ s} < t \leq 500 \text{ s}$
6	$500 \text{ s} < t \leq 900 \text{ s}$	$300 \text{ s} < t \leq 500 \text{ s}$	$100 \text{ s} < t \leq 300 \text{ s}$

Note: Duration of 400 s is corresponding to 100 waves for EQ and 57 waves for AQ. Duration of 200 s is corresponding to 50 waves for EQ and 29 waves for AQ.

Chapter 5

General Conclusions

In this dissertation the interactions between hydrodynamics, sediment suspension and transport, and morphological evolution in the surf zone was investigated with a large-scale laboratory experiment data, CROss-Shore Sediment Transport Experiment (CROSSTEX). The data set included comprehensive measurements of water surface elevation, fluid velocity, sediment concentration, and morphology for irregular waves under erosive and accretive beach conditions. In Chapter 2, hydrodynamics were examined in response to morphological evolution, focusing on turbulence due to wave breaking. In Chapter 3, intermittent features of sediment suspension and turbulence, and their relationship were examined. In Chapter 4, the intermittent sediment suspension was predicted with an artificial neural network using the results from Chapter 2 and Chapter 3. General 12 conclusions can be drawn as follows.

- (1) The beach evolves to the quasi-equilibrium state in approximately 100 minutes for both cases. The quasi-equilibrium state is defined when the ratio of bar height to width is stable. The bar crest migrates slowly offshore for the erosive case and onshore for the accretive case even in the quasi-equilibrium state.

- (2) Waves break in a more plunging manner for the erosive case and in a spilling manner for the accretive case as the beach evolves, and was generally consistent with observations.
- (3) The vertical distribution of normalized time-averaged turbulent kinetic energy from the Shaw and Trowbridge (2001) method is larger than the high-pass filtering method (cut-off frequency: 0.0625 Hz) by a factor of 2 but smaller than those of the T98 method by approximately 10~15% over water depth.
- (4) Turbulent kinetic energy is closely related to the wave energy loss by wave breaking. Also the turbulence intensities are smaller at the bar trough are smaller than those inside the surf zone. This is due to the rapid increase of water depth at the bar trough, where the spread of TKE are enhanced by the increased water mass. Inside the surf zone, strong intensities of turbulence are observed due to a second breaking on a shallow water depth.
- (5) Similar intermittency statistics were found over the cross-shore locations, although the thresholds used for the intermittency analysis varied. The comparison of intermittency between the present study and the previous studies (Cox and Kobayashi, 2000; Jaffe and Sallenger, 1992) agrees well despite the different experimental conditions. The similar intermittency suggests that turbulence and sediment suspension can be characterized as a self-similar, intermittent process in the surf zone.

- (6) From a conditional probability, 20~35% (~10% at the bar crest in the erosive case) of the turbulent events may trigger the suspension events. Also, 50~65% (~40% at the bar crest in the erosive case) of the suspension events are induced by the turbulent events.
- (7) The sediment suspension events uncorrelated with turbulence were mostly induced when strong offshore low-frequency motion were present, highlighting the need for better understanding of advection in the surf zone. The bar trough in the accretive case was an exception, and the horizontal pressure gradient was discussed as a contributing mechanism.
- (8) The duration of intermittent events were uniform over water depth. The motions contained in the intermittent events of turbulence were vertically uniform, whereas the suspended load varied vertically, showing large values near the bed.
- (9) The intense suspension events drove the onshore sediment transport mainly with the wave-induced motion. The onshore sediment transport was observed in the AQ state during the intense suspension events, while the EQ state shows offshore sediment flux even in the intense suspension events. Comparison these results with the field work by Jaffe and Sallenger (1992) confirmed the importance of intermittency on the cross-shore sediment transport.

- (10) Turbulent kinetic energy near the bed is important to predict the sediment suspension in the surf zone for both EQ and AQ. When turbulent kinetic energy was considered as an input, the correlation coefficient between the measured and predicted sediment suspension increases by a factor of 3, compared with the case where only the low-frequency motion or wave-induced motion was used as an input. The best predictions are shown at the bar crest. These results represent the importance of turbulence from the intense wave breaking at the bar crest, for sediment suspension.
- (11) Outside the surf zone, the wave-induced motion is the most contributing factor for the sediment suspension with a less importance of TKE.
- (12) When the information from the upper ADV was included as inputs, the ANN model improved the prediction capability by 40 % at the bar trough in EQ while it did not improve the prediction in AQ. The increased prediction in EQ can be attributed to the coherent turbulent structure which is probably induced by return currents from wave breaking.

Overall, the interaction of hydrodynamics (especially turbulence), sediment suspension over an evolving beach were quantitatively observed (Chapter 2 and 3) and predicted (Chapter 4). Hopefully, these findings can contribute to understanding and modeling of sediment transport problems in the surf zone.

Bibliography

- Aagaard, T., J. Nielsen, and B. Greenwood, 1998, Suspended sediment transport and nearshore bar formation on a shallow intermediate-state beach, *Marine Geology*, 148, 203–225.
- Aagaard, T., and M. G. Hughes, 2006, Sediment suspension and turbulence in the swash zone of dissipative beaches, *Marine Geology*, 228, 117–135.
- Aagaard, T., and M. G. Hughes, 2010, Breaker turbulence and sediment suspension in the surf zone, *Marine Geology*, 271, 250-259.
- Bailard, J. A., 1981, An energetics total load sediment transport model for a plane sloping beach, *J. Geophys. Res.*, 86, 10938-10964.
- Battjes, J. A. 1974. Surf similarity, *Proceedings of the 14th International Conference on Coastal Engineering*. ASCE, New York, 466-480.
- Battjes, J. A., 1975. Modeling of turbulence in the surf zone, paper presented at *Symposium on Modeling Techniques* Am. Soc. Of Civ. Eng., San Francisco, California.
- Beach, R. A., and R. W. Sternberg, 1988, Suspended sediment transport in the surf zone: responses to cross-shore infra-gravity motion, *Marine Geology*, 80, 61-79.
- Black, K. P., R. M. Gorman, and G. Symmonds, 1995. Sediment transport near the breakpoint associated with cross-shore gradients in vertical eddy diffusivity, *Coastal Eng.*, 23, 95-114

- Blenkinsopp, C. E, and J. R. Chaplin. 2008. The effect of relative crest submergence on wave breaking over submerged slopes, *Coastal Eng.*, 55, 967-974.
- Bowen, A. 1981. Simple models of nearshore sedimentation: Beach profiles and longshore bars, *Coastline Can.*, 80-10, 1-11.
- Bouws, E., H. Gunther, W. Rosenthal, and C. L. Vincent. 1985. Similarity of the wind wave spectrum in finite depth water, Part I- Spectral form, *J. Geophys. Res.*, 90 (C1), 975-986.
- Browne, m., B. Castelle, D. Strauss, R. Tomlinson, M. Blumenstein, and C. Lane, 2007, Near-shore swell estimation from a global wind-wave model: Spectral process, linear and artificial neural network models, *Coastal Eng.*, 54, 445-460.
- Butt, T., P. Russell, J. Puleo, J. Miles, and G. Masselink. 2004. The influence of bore turbulence on sediment transport in the swash and inner surf zone, *Continental Shelf Research*, 24, 757-771
- Butt, T., P. Russell, J. Puleo, J. Miles, and G. Masselink. 2005, The application of Bagnold-type sediment transport models in the swash zone, *Journal of Coastal Research*, 21, 887-895.
- Chang, K, -A., and P. L. -F. Liu. 1999. Experimental investigation of turbulence generated by breaking waves in water of intermediate depth, *Physics of fluids*, 11, 3390-3400.

- Cox, D.T., N. Kobayashi, and H. Mase, 1991, Effects of Fluid Accelerations on Sediment Transport in Surf Zones, *Proc. of Coastal Sediments 91*, Am. Soc. Civil Engrg., 447-461.
- Cox, D. T., N. Kobayashi, and A. Okayasu. 1995. *Experimental and numerical modeling of surf zone hydrodynamics*, Res. Report CACR-95-07, Center for Applied Coastal Research, University of Delaware, 293 pp.
- Cox, D.T. and Kobayashi, N., 1998, Application of an undertow model to irregular waves over plane and barred beach, *Journal of Coastal Research*, 14 (4), 1314-1324.
- Cox, D. T., and N. Kobayashi, 2000, Identification of intense, intermittent coherent motions under shoaling and breaking waves, *J. Geophys. Res.*, 105, C6, 14223-14236.
- Cox, D. T., and S. L. Anderson, 2001, Statistics of intermittent surf zone turbulence and observations of large eddies using PIV, *Coastal Eng. J.*, 43, 121-131.
- Cox, D.T., P. Tissot, and P. Michaud, 2002, Water level observations and short-term predictions including meteorological events for entrance of Galveston bay, Texas, *J. waterway, Port, Coastal and Ocean Engineering.*, 128, 21-29.
- Dally, W. R., and R. G. Dean, 1984, Suspended sediment transport and beach profile evolution, *J. waterway, Port, Coastal and Ocean Engineering.*, 110, 15-33.

- Downing, J, 2006. Twenty-five years with OBS sensors: The good, the bad and the ugly, *Continental Shelf Research*, 26, 2299-2318.
- Elgar, S., R.T. Guza, B. Raubenheimer, T.H.C. Herbers, and E. L. Gallagher, 1997, Spectral evolution of shoaling and breaking waves on a barred beach, *J. Geophys. Res.*, 102 (C7), 15797-15805.
- Feddersen, F., and A. J. Williams III, 2007, Direct estimation of the Reynolds stress vertical structure in the nearshore, *J. Atmos. Oceanic Technol.*, 24, 102-116.
- Foster, D. L., R. A. Holman, and R. A. Beach, 1994, Correlation between sediment suspension events and shear instabilities in the bottom boundary layer of the surf zone. *Proceedings of Coastal Dynamics '94*, 712-726, Am. Soc. Civil Eng., New York
- Foster, D. L., R. A. Beach, and R. A. Holman, 2000, Field observations of the wave bottom boundary layer, *J. Geophys. Res.*, 105(C8), 19,631-19,647.
- Foster, D. L., A. J. Brown, R. A. Holman, and P. Natoo, 2006, Field evidence of pressure gradient induced incipient motion, *J. Geophys. Res.*, 111, C05004.
- Fugate, D., C. and C. T. Friedrichs, 2002. Determining concentration and fall velocity of estuarine particle populations using ADV, OBS and LISST, *Continental Shelf Research*, 22, 1867-1886.
- Fredsøe, J., and R. Deigaard. 1998. *Mechanics of Coastal Sediment Transport*, World Scientific Publishing, Singapore, 369 pp.

- Gallagher, E.L., S. Elgar and R.T. Guza, 1998, Observations of sand bar evolution on a natural beach, *J. Geophys. Res.*, *103* (C2), 3203–3215.
- Garcez Faria, A.F., E.B.Thornton, T.C.Lippmann, and T.P.Stanton, 2000, Undertow over a barred beach, *J. Geophys. Res.*, *105* (C7), 16,999–17,010.
- George, R., R. E. Flick, and R. T. Guza. 1994. Observations of turbulence in the surf zone, *J. Geophys. Res.*, *99* (C1), 801-810.
- Goring, D. G., and V. I. Nikora. 2002. Despiking acoustic Doppler velocimeter data, *J. Hydraul. Eng.*, *128* (1), 117-126.
- Govender, K., G. P. Mocke, and M. J. Alport, 2002, Video-imaged surf zone wave and roller structures and flow fields, *J. Geophys. Res.*, *107*(C7), 3072.
- Govender, K., H. Michallet, M.J. Alport, U. Pillay, G.P. Mocke, and M. Mory, 2009. Video DCIV measurements of mass and momentum fluxes and kinetic energies in laboratory waves breaking over a bar, *Coastal Eng.*, *56*, 876-885.
- Hagan, M.T., H.B. Demuth, and M. Beale, 1996, *Neural network design*. PWS Publishing, Boston, Massachusetts. 736 pp.
- Haines, J.W. and A. H. Sallenger Jr., 1994, Vertical structure of mean cross-shore currents across a barred surf zone, *J. Geophys. Res.*, *99* (C7), 14,223–14,242.
- Haller, M. C., R. A. Dalrymple, and I. A. Svendsen, 2002, Experimental study of nearshore dynamics on a barred beach with rip channels, *J. Geophys. Res.*, *107* (C6), 3061, doi:10.1029/2001JC000955

- Hanes, D., M. and D. A. Huntley, 1986. Continuous measurements of suspended sand concentration in a wave dominated nearshore environment, *Continental Shelf Research*, 6, 585-596.
- Hanes, D., M., 1988, Intermittent sediment suspension and its implications to sand tracer dispersal in wave-dominated environments, *Marine Geology*, 81, 175-183.
- Henderson, S. M., J. S. Allen, and P. A. Newberger, 2004, Nearshore sandbar migration predicted by an eddy-diffusive boundary layer model, *J. Geophys. Res.*, 109, C06024, Doi:10.1029/2003JC002137
- Hoefel, F. and S. Elgar, 2003. Wave-induced sediment transport and sandbar migration, *Science*, 299, 1885-1887
- Holman, R. A., 1995. *Nearshore processes*, Review of geophysics, Supplement, July 1995, 1237-1247.
- Hsu, T.-J, S. Elgar, and R. T. Guza, 2006, Wave-induced sediment transport and onshore sandbar migration, *Coastal Eng.*, 53, 817-824
- Huang, Z.-C., S.-C. Hsiao, H.-H. Hwung, and K.-A. Chang, 2009. Turbulence and energy dissipations of surf-zone spilling breakers, *Coastal Eng.*, 56, 733-746.
- Hughes, S. A., 1998, *Physical models and laboratory techniques in coastal engineering*, World Scientific, 568 pp.
- Jaffe, B. E., R. W. Sternberg, and A. H. Sallenger Jr., 1984, The role of suspended sediment in shore-normal beach profile changes, *Proceedings of the 19rd*

- International Coastal Engineering Conference*, 2, 1983-1996, Am. Soc. Civil. Eng., New York
- Jaffe, B. E., and A. H. Sallenger Jr., 1992, The contribution of suspension events to sediment transport in the surf zone, *Proceedings of the 23rd International Coastal Engineering Conference*, 3, 2690-2693, Am. Soc. Civil. Eng., New York
- Kinston, K. S., B.G. Ruessink, I. M. J. van Enckevort, and M. A. Davidson, 2000, Artificial neural network correction of remotely sensed sandbar location, *Marine Geology*, 169, 137-160.
- Kimmoun, O., and H. Branger. 2007. A particle image velocimetry investigation on laboratory surf-zone breaking waves over a sloping beach, *J. Fluid Mech.*, 588, 353-397.
- Kobayashi, N., H. Zhao, and Y. Tega, 2005, Suspended sand transport in surf zone, *J. Geophys. Res.*, 110, C12009
- Kobayashi, N., A. Payo, A., and L. Schmied, 2008, Cross-shore suspended sand and bedload transport on beaches, *J. Geophys. Res.*, 113, C07001.
- Kubo, H., and T. Sunamura, 2001, Large-scale turbulence to facilitate sediment motion under spilling breakers. *Proceedings of Coastal Dynamics '01*, 212-221, Am. Soc. Civil Eng., New York
- Kuriyama, Y., 2002, Medium-term bar behavior and associated sediment transport at Hasaki, Japan, *J. Geophys. Res.*, 107 (C9), 3132, doi:10.1029/2001JC000899.

- Madsen, O. S., 1974., Stability of a sand bed under breaking waves, *Proceedings of the 14th International Conference on Coastal Engineering*. 776-794. Am. Soc. Civil. Eng., New York
- Marino-Tapia, I.J., P.E.Russell, T.J.O'Hare, M.A. Davidson, and D.A.Huntley, 2007a, Cross-shore sediment transport on natural beaches and its relation to sandbar migration patterns: 1. Field observations and derivation of a transport parameterization, *J. Geophys. Res.*, *112*, C03001,doi:10.1029/2005JC002893.
- Marino-Tapia, I.J., P.E.Russell, T.J.O'Hare, M.A. Davidson, and D.A.Huntley, 2007b, Cross-shore sediment transport on natural beaches and its relation to sandbar migration patterns: 2. Application of the field transport parameterization, *J. Geophys. Res.*, *112*, C03002,doi:10.1029/2005JC002894.
- Mase, H., M. Sakamoto, and T. Sakai, 1995, Neural network for stability analysis of rubble-mound breakwaters, *J. waterway, Port, Coastal and Ocean Engineering.*, *121*, 294-299.
- Melville, W. K., F. Veron, and C. J. White. 2002. The velocity field under breaking waves: coherent structures and turbulence, *J. Fluid Mech.*, *454*, 203-233.
- Mocke, G. P., 2001, Structure and modeling of surf zone turbulence due to wave breaking., *J. Geophys. Res.*,*106*(C8), 17,039-17,057.
- Mori, N., T. Suzuki, and S. Kakuno. 2007. Noise of acoustic Doppler velocimeter data in bubbly flows, *J. of Engrg Mech.*, *133*, 122-125

- Mori, N., T. Suzuki, and S. Kakuno. 2007. Experimental study of air bubbles and turbulence characteristics in the surf zone, *J. Geophys. Res.*, *112*, C05014.
- Nadaoka, K., and T. Kondoh. 1982. Laboratory measurements of velocity field structure in the surf zone by LDV, *Coastal Eng. in Japan*, *25*, 125-146.
- Nadaoka, K., M. Hino, and Y. Koyano. 1989. Structure of the turbulent flow field under breaking waves in the surf zone, *J. Fluid Mech.*, *204*, 359-387.
- Nielsen, P., 1992. *Coastal bottom boundary layers and sediment transport*, World Scientific Publishing, Singapore, 324 pp.
- Oehler, F., G. Coco, M.O. Green, and K.R. Bryan, 2011, A data-driven approach to predict suspended-sediment reference concentration under non-breaking waves, *Continental Shelf Research*, doi:10.1016/j.csr.2011.01.015.
- Ogston, A. S. and R. W. Sternberg, 1995. On the importance of nearbed sediment flux measurements for estimating sediment transport in the surf zone, *Continental Shelf Research*, *15*, 1515-1524.
- Okayasu, A., K. Fujii, and M. Isobe, 2010, Effect of external turbulence on sediment pickup rate, *Proceedings of the 32nd International Coastal Engineering Conference*, <https://journals.tdl.org/ICCE/article/view/1434>, Am. Soc. Civil. Eng., New York.
- Osler, M. S., I. A. Svendsen, and J.T. Kirby. 2004. A Laboratory Investigation of Nearshore Turbulence. *Proceedings of the 29th International Conference on Coastal Engineering*, ASCE, 2,1393-1403.

- Panizzo, A., and R. Briganti, 2007, Analysis of wave transmission behind low-crested breakwaters using neural networks, *Coastal Eng.*, 54, 643-656.
- Puleo, J. 2009, Tidal variability of swash-zone sediment suspension and transport, *Journal of Coastal Research*, 25 (4), 937-948.
- Rodriguez, A, A. Sánchez-Arcilla, J. M. Redondo, and C. Mösso. 1999. Macroturbulence measurements with electromagnetic and ultrasonic sensors: a comparison under high-turbulent flows, *Experiments in fluids*, 27, 31-42.
- Roelvink, J.A, and I. Broker, 1993, Cross-shore profile models, *Coastal Engineering*, 21, 163–191.
- Roelvink, J. A. and M. J. F. Stive. 1989, Bar-generating cross-shore flow mechanism on a beach, *J. Geophys. Res.*, 94 (C4), 4785-4800.
- Ruessink, B. G., 2010. Observations of turbulence within a natural surf zone, *J. Phys. Oceanogr.*, 40, 2696-2712.
- Scott, C. P., D. T. Cox, Shin, S. and Clayton, N., 2004. Estimates of surf zone turbulence in a large-scale laboratory wave flume. *Proceedings of the 29th International Conference on Coastal Engineering*. 379-391. Am. Soc. Civil. Eng., New York.
- Scott, C. P., D. T. Cox, T. B. Maddux, and J. W. Long. 2005. Large-scale laboratory observations of turbulence on a fixed barred beach, *Meas. Sci. Technol.* 16, 1903-1912.
- Scott, C. P., D. T. Cox, S. Shin, and T. B. Maddux. 2006. The role of wave breaking turbulence in sediment suspension observed during CROSSTEX,

Proceedings of the 30th International Conference on Coastal Engineering. ASCE, 3, 2537-2546.

Scott, N. V., T.-J. Hsu, and D. T. Cox, 2009, Steep wave, turbulence, and sediment concentration statistics beneath a breaking wave field and their implications for sediment transport, *Continental Shelf Research*, 29, 2303-2317.

Shaw, W. J., and J. Trowbridge. 2001. The direct estimation of near-bottom turbulent fluxes in the presence of energetic wave motions, *J. Atmos. Oceanic Technol.*, 18, 1540-1557.

Smith, E. R., and N. C. Kraus, 1991, Laboratory study of wave-breaking over bars and artificial reefs, , *J. waterway, Port, Coastal and Ocean Engineering.*, 117, 307-325.

Smith, G. G., and G. P. Mocke, 2002, Interaction between breaking/broken waves and infragravity-scale phenomena to control sediment suspension transport in the surf zone, *Marine Geology*, 187, 329–345.

Stive M. J. F., 1980. Velocity and pressure field in spilling breakers, *Proceedings of the 17th International Conference on Coastal Engineering.* ASCE, 1, 547-566

Svendsen, I., A, 1987. Analysis of surf zone turbulence, *J. Geophys. Res.*, 92, 5115-5124.

- Suzuki, T., A. Okayasu, and T. Shibayama. 2007. A numerical study of intermittent sediment concentration under breaking waves in the surf zone, *Coastal Eng.*, 54, 433-444.
- Suzuki, T., S. Shin, D. T. Cox, and N. Mori, 2010, Spatiotemporal characteristics of near-bed pressure gradient on a barred beach, *J. waterway, Port, Coastal and Ocean Engineering.*, 136, 327-336.
- Tennekes, H., and J. L. Lumley, 1972, *A First Course in Turbulence*, MIT Press, 300pp
- Thornton, E.B. and R.T. Guza, 1983, Transformation of wave height distribution, *J. Geophys. Res.*, 88 (C10), 5925–5938.
- Thornton, E.B., R.T. Humiston, and W. Birkemeier, 1996, Bar/trough generation on a natural beach, *J. Geophys. Res.*, 101 (C5), 12,097-12,110.
- Thornton, E.B., R.A. Dalrymple, T. Drake, E. Gallagher, R.T. Guza, A. Hay, R.A. Holman, J. Kaihatu, T.C. Lippmann, and T. Özkan-Haller. 2000. State of nearshore processes research: II, *Technical Report NPS-OC-00-001*, Naval Postgraduate School, Monterey, CA, 37 pp.
- Ting, F. C. K., and J. T. Kirby. 1994. Observation of undertow and turbulence in a laboratory surf zone, *Coastal Eng.*, 24, 51-80.
- Ting, F. C. K., and J. T. Kirby. 1995. Dynamics of surf-zone turbulence in a strong plunging breaker, *Coastal Eng.*, 24, 177-204.
- Ting, F. C. K., and J. T. Kirby. 1996. Dynamics of surf-zone turbulence in a spilling breaker, *Coastal Eng.*, 27, 131-160.

- Trowbridge, J., 1998. On a technique for measurement of turbulent shear stress in the presence of surface waves, *J. Atmos. Oceanic Technol.*, *15*, 290-298.
- Trowbridge, J., and S. Elgar. 2001. Turbulence measurements in the surf zone, *J. Phys. Oceanogr.*, *31*, 2403-2417.
- Tsai, C. P., and T. Lee, 1999, Back-propagation neural network in tidal-level forecasting, *J. waterway, Port, Coastal and Ocean Engineering.*, *125*, 195-202.
- van Gent, M.R.A., H.F.P. van den Boogaard, B. Pozueta, and J.R. Medina, 2007, Neural network modeling of wave overtopping at coastal structures, *Coastal Eng.*, *54*, 586-593.
- van Maanen, B., G. Coco, K.R. Bryan, and B.G. Ruessink, 2010, The use of artificial neural networks to analyze and predict alongshore sediment transport, *Nonlin.Processes Geophys.*, *17*, 395-404.
- van Rijn, 1984, Sediment pickup functions, *Journal of Hydraulic Eng.*, *110*, 1494-1502.
- Wang, P., B. A. Ebersole, E. R. Smith, and B. D. Johnson. 2002. Temporal and spatial variations of surf-zone currents and suspended sediment concentration, *Coastal Eng.*, *46*, 175-211.
- Yoon, H.-D, and D. T. Cox, 2010, Large-scale laboratory observations of wave breaking turbulence over an evolving beach, *J. Geophys. Res.*, *115*, C10007, Doi:10.1029/2009JC005748.

Yoon, H.-D, and D. T. Cox, 2011, Cross-shore variation of intermittent sediment suspension and turbulence induced by depth-limited wave breaking, submitted to *Continental Shelf Research*.

Yu, Y., Sternberg, R. W., and R. A. Beach, 1993. Kinematics of breaking waves and associated suspended sediment in the nearshore zone, *Continental Shelf Research*, 13, 1219-1242.